Quantum dot and Its nanocomposites : interactions with biosystems and biomedical applications

Lu, Zhisong

2011

Lu, Z. S. (2011). Quantum dot and Its nanocomposites : interactions with biosystems and biomedical applications. Doctoral thesis, Nanyang Technological University, Singapore.

https://hdl.handle.net/10356/44700

https://doi.org/10.32657/10356/44700

(On the Spine)

QD & Its Nanocomposites: Interactions with Biosystem & Bioapplications

LU ZHISONG

2011

NANYANG TECHNOLOGICAL UNIVERSITY

Quantum Dot and Its Nanocomposites: Interactions with Biosystems and Biomedical Applications

LU ZHISONG

SCHOOL OF CHEMICAL AND BIOMEDICAL ENGINEERING

2011

Quantum Dot and Its Nanocomposites: Interactions with Biosystems and Biomedical Applications

LU ZHISONG

School of Chemical and Biomedical Engineering

A thesis submitted to the Nanyang Technological University
in fulfillment of the requirement for the degree of
Doctor of Philosophy

2011

Acknowledgements

First and foremost, I would like to express my deepest respect and most sincere gratitude to my supervisor, Prof. Chang Ming Li, for his guidance and encouragement. Prof. Li constantly advised, inspired, and supported me throughout the course of my study. He also imparted his knowledge and experience while providing me with excellent advice during my experiments and manuscript writing. Without his guidance, support, and encouragement, it would not have been possible for me to overcome the setbacks and obstacles that I encountered during the course of this research. I will always treasure my research experience with him, which will continue to motivate me as I face scientific challenges in the future.

I would like to thank all the research staff and graduate students at the Centre for Advanced Bionanosystems for their friendship over the years. I cherish the moments that we shared together, and your inspiration and experimental assistance are greatly appreciated.

Special thanks go to my dear wife, Qiao Yan, for all her love and support. Last but not least, I wish to thank my parents for their love and dedication in raising me, supporting me, and educating me throughout my life.

Table of contents

List of figures

List of tables

Abstract

Quantum dots (QDs), semiconductor nanocrystals of a size ranging from 1 to 10 nm, have been extensively studied as replacements for or complements to traditional organic dyes in advanced biosensing, cell imaging, and *in vivo* animal tracking applications. In spite of their many advantages compared to traditional materials, their use as antimicrobial agents and the development of biocompatible QD–based nanocomposites for various biomedical applications remain great challenges. Addressing these challenges, this PhD research project investigated the antimicrobial activity of Cadmium Telluride (CdTe) QDs and its underlying mechanism, the fabrication of biocompatible QD nanocomposites for cell imaging, and the impact of the shape of specifically designed QD nanocomposites on phagocytosis to extend the biomedical applications of CdTe QDs and provide scientific insights into bionanosystems.

One primary accomplishment of this research was its investigation of the bactericidal activity of CdTe QDs on *Escherichia coli* (*E. coli*) and the mechanism behind this activity for the first time. Based on the finding that QDs attach to bacterial cells, impair their anti–oxidative system, including down–regulations of antioxidative genes and decreases of antioxidative enzymes activities, it is proposed that the primary mechanism behind the bactericidal activity of CdTe QDs involving QDs–bacteria association and a reactive oxygen species (ROS)–mediated pathway.

Besides the bactericidal effects, QD–induced bacterial growth inhibition and its photophysical mechanism were also investigated. The growth curve and atomic force

microscopy (AFM) images show that QDs can inhibit the growth of bacterial cells via blocking cell division. Combining biological and physical discoveries, a photophysical mechanism involving a polypeptide or amino acid adsorption–mediated fluorescence and ROS quenching process is elucidated. Thus, CdTe QDs could have the potential to be formulated as a novel antimicrobial material with excellent optical properties.

Although QDs can be coated with a variety of materials to reduce their nanotoxicity, these materials may introduce new toxic sources and quench fluorescence to a degree that confines the biomedical applications of the resulting QD nanocomposites. To address this challenge, ZrO_2, an excellent ceramic biomaterial with a low extinction coefficient and a high level of biocompatibility, was utilized to coat CdTe QDs for the first time. The experimental results indicate that ZrO_2–QD nanocomposites with a size of ~30 nm in diameter possess a relatively high level of fluorescence and a low level of nanotoxicity. After being functionalized with folic acid, these nanocomposites were able to label cultured *HeLa* cells effectively, indicating that ZrO_2–QD nanocomposites are promising biocompatible nanomaterials that may be able to replace or complement pristine QDs in biomedical applications.

This project also demonstrated the utility of a green synthesis method mediated by *E. coli* to harvest protein–coated CdTe QDs nanocomposites, which possess a high level of crystallinity, superior size–tunable optical properties, and a

fluorescence emission ranging from 488 nm to 551 nm. Experimental results revealed that the surface protein capping layer could maintain the viability of 92.9% of the cells in an environment with a QD concentration as high as 2 μM. This finding, as well as this study's successful preparation and use of folic acid–conjugated protein–QD nanocomposites for cervical cancer cell imaging *in vitro*, demonstrates that the QD–synthesis approach described in this work is an economical and environmentally friendly approach for the fabrication of highly fluorescent biocompatible CdTe–QD nanocomposites that have great potential in a broad array of bioimaging and biolabeling applications.

In a subsequent experiment, CdTe QD–cystine composites with dot, rod, and needle structures were fabricated via a one–pot cysteine–assisted hydrothermal approach and, after characterization, applied to explore the impact of particle shape on the macrophage phagocytosis. The finding that particle shape significantly affects macrophage phagocytosis at the initial cell–particle contact point not only advances fundamental understanding of shape–dependent macrophage responses but also offers a strategy for the design of drug carriers that can avoid the damage and phagocytosis of macrophage before reaching the desired cell populations by tailoring the particle shape.

In a brief, this interdisciplinary research project extended the research into material synthesis and characterization, cell behavior monitoring, biomolecular analysis, and cell imaging to fulfill the objectives of expanding the biomedical

applications of CdTe QDs and their nanocomposites, developing approaches to the fabrication of novel QD–based nanocomposites with reduced levels of cytotoxicity and of various structures, and advancing fundamental knowledge of the interaction between nanomaterials and biosystems.

Chapter 1 Introduction

1.1. Introduction

Due to remarkable advances in nanotechnology, nanomaterials have assumed increasing importance in the fields of informatics, optics, electronics, energy, environmental health, biomedicine, and pharmaceutics [1-11]. In 2007, the United States invested $13 billion in nanotechnology research, a figure that is expected to increase to $1 trillion by 2015 [12]. Defined as materials with one–dimension less than 100 nm in size that possess physicochemical properties unique from those of bulk materials of the same material composition, nanomaterials are expected to inspire a revolution in traditional biomedicine.

Among various nanomaterials, nanoparticles with a size comparable to that of cell organelles, or even that of DNA, protein, or lipid biomolecules, have attracted the prodigious interest of researchers because of their capacity to cross over cell gaps and easily penetrate into cells. After being conjugated with biomolecular affinity ligands, some nanoparticles, such as gold and iron oxide, have been utilized in biosensing applications, tumor cell imaging, and cancer therapy [13-18].

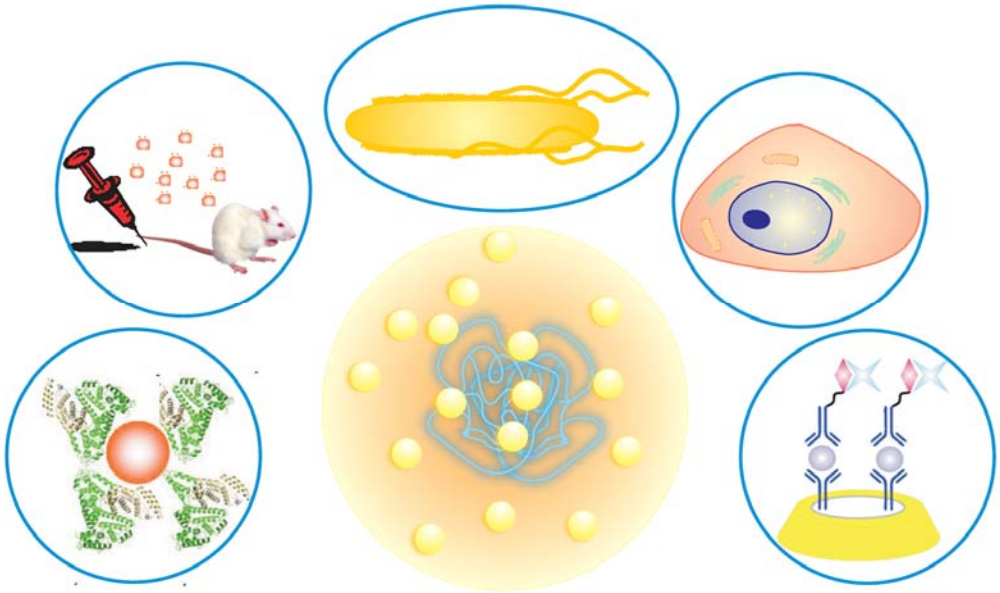

Figure 1.1 Biomedical applications of QDs

Quantum dots (QDs), semiconductor nanocrystals ranging in size from 1 to 10 nm, have been extensively studied for use as luminescent nanoprobes in biosensing and bioimaging applications [19-21]. Due to their ultrasmall size, broad excitation wavelength, high level of photostability, and excellent size–tunable fluorescence, QDs have been regarded as promising alternatives to traditional organic dyes [22, 23]. The recent development of QDs with near–infrared emission offers the possibility of their replacing radioactive reagents in *in vivo* imaging and tracking [24-27]. In spite of the merits of QDs, their use as antimicrobial materials and the development of biocompatible QD–based nanocomposites for various biomedical applications remain great challenges.

1.2. Motivations

Although the antimicrobial effects of QDs have been researched, all related studies solely focused on cadmium selenium (CdSe)–core QDs [28, 29]. As QDs with different core materials may interact with microbes in a distinct manner because of their different chemical and physical properties, it is of great importance to investigate the antimicrobial activities of QDs composed of other core materials. In addition, QD research to date has been limited to determination of the viability of QD–treated bacteria [28, 29], and has not yet elucidated the mechanism behind QD antimicrobial activity, particularly as it pertains to the bacterial response of QDs at the molecular level. Such lack of understanding of this mechanism hinders the application of QDs as bactericidal and bacterial growth inhibition nanomaterials.

As QD–released heavy metal ions cause severe cytotoxicity, which greatly limits their biomedical applications [30, 31], a variety of materials, such as polymer and silica, have been employed to coat QDs to prevent metal–ion release and thus reduce their cytotoxicity [32-39]. However, these non–biocompatible coating layers may introduce new toxic sources to the QD nanocomposites while, in most cases, causing significant fluorescence quenching. Therefore, there is a great need to identify a new coating material that not only improves QD biocompatibility but also maintains QD fluorescence. Besides the selection of coating materials, another major challenge is developing a simple and environmentally friendly method for the preparation of biocompatible QD nanocomposites without using toxic solvents.

QDs and their nanocomposites have been used as tools in biomedical research to solve bio–related problems or reveal the scientific nature of biological phenomena. However, their spherical shape may limit their application in specific areas, such as drug delivery systems and cell phagocytosis research. Therefore, there is a great need to fabricate QD nanocomposites of different shapes and nanostructures appropriate for a variety of functions.

1.3. Objectives

The overall objectives of this project were to extend the application of CdTe QDs and their nanocomposites in antimicrobial, tumor cell imaging, and cell phagocytosis research, as well to advance fundamental knowledge of the interaction between nanomaterials and biosystems. To so, this project focused on exploring the antimicrobial activity of CdTe QDs and its underlying mechanism, fabricating biocompatible QD nanocomposites for tumor cell imaging, developing a one–step biosynthesis approach for the preparation of biocompatible QD nanocomposites, and investigating cell phagocytosis with differently structured QD nanocomposites, and providing further scientific insights into bionanosystems. The following sections address each of these objectives in more detail.

1.3.1 To Investigate the Antimicrobial Activity of CdTe QDs and Its Underlying Mechanism

As the antimicrobial activity of CdTe–core QDs has not been studied to date, an important task of this project was to explore the concentration–dependent bactericidal and bacterial growth inhibition of CdTe–core QDs on *E. coli* cells. The antimicrobial mechanism involving the QD–bacterial association and the reactive oxygen species (ROS)–mediated pathway was investigated to provide the fundamental knowledge of QD antimicrobial activity necessary in the development of antimicrobial applications of QD nanocomposites.

1.3.2 To Fabricate Biocompatible CdTe QD–Based Nanocomposites for Tumor Cell Imaging

For the first time in the fabrication of biocompatible QD nanocomposites, zirconium dioxide (ZrO_2), an excellent ceramic biomaterial with a low extinction coefficient and a high level of biocompatibility, was utilized to coat CdTe QDs. Specifically, ZrO_2–QD nanocomposites of a small size offering a higher level of fluorescence emission and a lower level of nanotoxicity were fabricated via a reversible microemulsion approach for the efficient labeling of *HeLa* cells. These ZrO_2–QD nanocomposites show promise as biocompatible nanomaterials that can replace or complement pristine QDs in biomedical applications.

To develop a novel, cost–effective, environmentally friendly, and reproducible method for the synthesis of CdTe QD nanocomposites, an efficient biosynthesis

approach mediated by *E. coli* was studied to harvest protein–coated CdTe QDs with a tunable level of fluorescence emission. The protein–coating layer on the nanocomposites was found to not only increase the biocompatibility of QDs but also provide functional groups for the bioconjugation of molecular probes, further promoting the use of nanocomposites in tumor cell imaging.

1.3.3 To Explore the Impact of Material Shape on Phagocytosis with CdTe–QD Nanocomposites of Different Shapes

To gain understanding of the impact of material shape on phagocytosis for the optimization of the design of drug carriers, it is desirable to construct and investigate the impact of differently shaped nanocomposites with inherent luminescence. In this project, various shaped CdTe QD–cystine composites were synthesized via a one–pot cysteine–assisted hydrothermal approach. With the assistance of QD fluorescence, the macrophage phagocytosis of sphere–, rod–, and needle–shaped CdTe QD–cystine composite particles were then imaged under light illumination to provide valuable data for the design of optimal inorganic drug carriers that can eliminate phagocytosis from macrophages before reaching the desired cell populations.

1.4. Organization

Chapter 1 briefly introduces and provides an overview of the objectives and

motivations behind this PhD research project. Chapter 2 reviews recent advances in the development of QDs and nanocomposites, in particular their synthesis and application in biosensors, multimodal imaging agents, drug delivery carriers, and nanodevices for diagnostics and therapy. Chapter 3 describes the experimental approaches, materials, and instruments used in this study. After chapter 4 describes how this investigation of the bactericidal activity of CdTe QDs led to the identification of a distinct biomolecular mechanism behind CdTe QD bactericidal activity, chapter 5 explores the photophysical mechanism behind the CdTe QD–induced bacterial cell growth inhibition effect. Chapter 6 investigates the use of a ZrO_2 coating layer in the fabrication of CdTe QD nanocomposites with enhanced fluorescent properties for tumor cell imaging. Chapter 7 describes the development of a novel *E. coli*–based biosynthesis approach to preparing protein–coated CdTe QD nanocomposites for tumor cell imaging. Chapter 8 discusses the biomedical application of CdTe QD–cystine nanocomposites of different structures based on identification of the impact of their shape on macrophage phagocytosis before chapter 9 presents a general conclusion and recommends possible avenues for future research.

Chapter 2 Literature Review

2.1 Overview of QD

Engineered nanomaterials are of great interest to researchers because their physicochemical properties can differ greatly from those of bulk materials of the same material composition [40]. Among the various nanomaterials, QDs, semiconductor nanocrystals formed from the periodic groups II–VI, III–V, or IV–VI [31], have attracted great interest due to their promising size–tunable optical properties and great potential for use in biomedical applications. Because semiconductor nanocrystals are sufficiently small (1–10 nm) to approach the size of the Exciton Bohr Radius of the materials from which they originate, quantum confinement occurs, resulting in unique optical and electronic properties that differ from those of bulk semiconductors. Since a route was developed to synthesize highly luminescent QDs in a hot coordinating solvent in 1993 [41], QDs have been extensively studied in transistors [42], solar cells [43], LEDs [44] and diode lasers [45].

Figure 2.1 (A) Scheme of the core and coating of QDs. (B) A series fluorescence of MSA–CdTe QDs of different sizes under UV irradiation.

Generally, QDs are constructed from inorganic semiconductor cores, the properties of which determine QD optical or electronic properties, and an organic coating layer, which protects the core and provides a functional group for the conjugation of biological probes (Fig. 2.1). QD cores may consist of various compounds, such as CdTe, CdSe, zinc sulfide (ZnS), indium arsenate (InAs), or indium phosphate (InP) [46, 47], among which CdTe and CdSe are the most widely used in biomedical applications.

All water–soluble QDs are capped with either amphiphilic compounds or hydrophilic thiols or dithiols, such as mercaptoacetic acid (MAA), mercaptopropionic acid (MPA), mercaptosuccinic acid (MSA), or 11–mercaptoundecanoic acid (MUA) [48]. Owing to their unique optical properties, including a high level of photostability, size–tunable emission, bright photoluminescence, narrow range of emission, and broad range of UV excitation, as compared to conventional organic fluorescent dyes, QDs have been used as alternative or complementary materials in cell imaging [49], advanced biosensing [50, 51], single molecule detection [52], and *in vivo* animal tracking [53].

2.2 Antimicrobial Activity of Pristine QDs

Owing to their large specific surface area and high level of bioactivity, inorganic nanomaterials are promising replacements for extremely irritating and toxic

traditional organic antimicrobial agents. Many nanoparticles with antimicrobial activities have recently been investigated [54-59], of which silver nanoparticles have been reported to accumulate in the *E. coli* membrane and exhibit effective antibacterial effects [60]. Metal oxide nanoparticles, a type of nanomaterial that includes titanium dioxide (TiO_2), silicon dioxide (SiO_2), and zinc oxide (ZnO) nanoparticles, also display an excellent biocidal impact on both Gram–positive and Gram–negative bacteria [58]. Although all these compounds are photosensitive and can generate ROS under high–intensity light at a specific wavelength, only TiO_2 exhibits significant antibacterial activity when sunlight is applied as the excitation source [61, 62].

In addition to TiO_2 nanoparticles, QDs with superior size–dependent optical properties are promising antimicrobial nanomaterials. Under irradiation, QDs produce free radicals, of which the quality and the type are determined by their core materials [63]. It is known that excess free radicals are harmful to microbes. The liberation of free heavy metal ions from QDs could also be toxic to bacteria.

Since the use of QDs in single bacterium imaging is one of the most promising research areas in biological applications of QDs [64-66], the study of QD antimicrobial activity continues to expand. However, few studies have yet investigated the antimicrobial activities of QDs [28, 29]. Among them, Kloepfer *et al.* discovered that CdSe QDs could inhibit the growth of bacteria [28]. Recently, Dwarakanath *et al.* have demonstrated that antibody–QD conjugates exhibit stronger

antibacterial effects than do bare QDs [29]. However, all related studies have focused on the antimicrobial effects of CdSe–core QDs. Because their chemical and physical properties play a vital role in bioactivities, QDs composed of different core materials likely interact differently with microbes. Thus, it is of great importance to investigate the antimicrobial activities of QDs that are composed of other core materials.

2.3 Advances in Developing Biocompatible QD Nanocomposites

The possibility of core material–induced nanotoxicity is an important consideration in the introduction of QDs within a biosystem. Although non–heavy metal–based QDs have recently been developed, their poor quantum yield (QY) and narrow size–tunable emission range greatly hinders their application to biomedicine [67-69]. Currently, coating QDs with biocompatible materials is the best means of preventing the leaching of heavy metal ions while simultaneously maintaining the optical properties of the QDs.

2.3.1 QD–Polymer Nanocomposites

Two strategies have been developed to fabricate QD–polymer nanocomposites: ligand exchange to replace the original hydrophobic ligands on the QD surface with polymer molecules and polymer encapsulation of QDs without changing the native surface ligand layer [21, 70]. The coated long–chain polymer molecules not only

contain a large number of hydrophilic groups to enhance the water dispersability of QDs in biological buffer solutions but also provide chemical functional groups for the conjugation of bio–probes. To increase their biocompatibility, QDs have been coated with various polymers to reduce their cytotoxicity. In an early study, an amphiphilic polymer coating layer on CdSe QD was shown to significantly reduce QD cytotoxicity [71], an effect attributed to blocking of the diffusion of the released Cd^{2+} ions from the QDs. When Nie and Duan subsequently used polyethylene glycol (PEG)–grafted–polyethylenimine (PEI) to encapsulate QDs, they found that the cytotoxicity of the coated QDs depended on the number of PEG grafts on each PEI molecule, with a greater number of PEG grafts leading to less cytotoxicity [72]. This discovery suggests that the longer polymer chains may wrap around QDs to form a more compact layer as a barrier to the release of Cd^{2+} ions. Because PEI itself is a cytotoxic polymer, the presence of a greater number of PEG grafts may also prevent the contact of PEI with cells [72].

To avoid the introduction of additional toxic sources into QD–polymer nanocomposites, biocompatible polymers, among which natural biomolecules such as denatured proteins and gelatin are ideal [73-75], have been used to encapsulate QDs. As the conventional fabrication of protein–coated composites normally requires two steps, the synthesis of functionalized QDs and the linking of biomolecules, a new approach that can produce biomolecule–coated QDs through a one–step reaction is highly desirable.

Although polymer coating can enhance QD biocompatibility, it has several drawbacks, including having a large hydrodynamic size, altering the surface charge, and reducing the fluorescence, which affect cell penetration capacity, water solubility, and imaging efficiency. The physiochemistry of the QD surface may also be tremendously changed by polymer coating, further affecting QD stability. Therefore, the selection of polymer and the control of coat thickness should be carefully considered in the design and fabrication of QD–polymer biocompatible nanocomposites.

2.3.2 Silica–QD Nanocomposites

Silica has been employed to coat QDs due to its ability to prevent the flocculation of particles and maintain photoluminescence, as well to accept the addition of many functional groups, such as the thiol, amine, phosphate, and carboxylate groups [76]. Silica–encapsulated QD composites have been fabricated through a sol–gel process referred to as the Ströber method in which a silica shell grows with QDs as seeds in a water–ethanol mixture [77, 78]. Hydrophilic QDs can be directly used in this approach, but a prior ligand exchange is required for the hydrophobic QDs synthesized in organic systems.

To overcome this challenge and the difficulty of controlling the shell thickness of silica–QD nanoparticles using the Ströber method, a water–in–oil (W/O) microemulsion approach has been developed [79] in which a silica precursor hydrolyzes and condenses at the W/O interface to form spherical nanoparticles. In

comparison to the Ströber method, this approach allows for better control of the size and shell thickness of the coated particles, and is simpler to perform because both hydrophobic and hydrophilic QDs can be directly used.

Similar to the polymer coating layer, the silica shell protects the core materials from the oxidative environment to reduce QD cytotoxicity. It has been reported that the viability of the cultured cells can be maintained at more than 95% even after treatment with 5 μm silica–CdSe QDs for 48 hrs [80]. However, it has also been found that the encapsulation of QDs with a silica shell affects the optical properties of QDs, with most related research reporting that QY decreases after coating with silica [38, 80, 81]. Graf *et al.* has observed a dramatic drop of QY from 21% to 1% after coating CdSe/ZnS QD with silica [37]. Although UV irradiation can enhance the photoluminescence of silica QD up to a factor of ten [37], the level of fluorescence is still significantly lower than that of pristine QDs.

Research into the effects of silica shell thickness on the photoluminescence of silica–QD nanocomposites has found that fluorescence intensity first increases then decreases as the thickness of the shell increases [80, 82]. Clearly, the shell thickness determines the nanocomposite size, which is critical in bioapplications, especially intracellular localization and *in vivo* targeting. Thus, when a silica–QD nanocomposite is designed for biomedical systems, the shell thickness should be tailored to strike a balance between the need to control nanotoxicity and maximize photoluminescence while maintaining the appropriate nanocomposite size.

Responding to the fact that the surface chemistry of QD nanocomposites influences their solubility, dispersity, optical properties, and probe conjugation, both silica and polymers have been utilized together in QD modification aimed at achieving the most desirable properties. Various multifunctional QD nanocomposites have been fabricated using polymer or silica as a matrix to encapsulate multiple components in one nanocomposite, a method that greatly expands the application of QDs in bioimaging, biosensing, drug delivery, and drug therapy.

2.4 Multifunctional QD Nanocomposites for Multimodal Imaging, Drug Delivery, and Cancer Therapeutics

Although their excellent fluorescent properties render QDs among the most attractive nanomaterials in bioimaging applications, they require further functionalization before being able to perform multiple functions in biomedical applications. Compositing QDs with other functional materials has been one approach shown to promote QD multifunctionality in multimodal imaging, drug delivery, diagnostics, and therapeutics.

2.4.1 QD Nanocomposites for Multimodal Imaging

Currently, various bioimaging approaches, such as optical imaging, magnetic resonance imaging (MRI), positron emission tomography (PET), and radioactive imaging, are used to target specific biomolecules or tissues [83-87]. However, no

one technique can provide complete and detailed information regarding cellular structure, location, and biomolecular activity due to limitations in resolution or sensitivity [88]. In response to this challenge, a multimodal strategy combining two or more complementary imaging methods has been developed to collect a variety of visual data.

Gadolinium (Gd) ion–chelated polymers, which are widely used as biocompatible contrast agents for MRI, have been composited with QDs to fabricate nanocomposites for simultaneous fluorescent and magnetic resonance detection. Silica–shelled QDs incorporated with Gd complexes have also been prepared for multimodal bioimaging [89]. Although both fluorescent and MRI imaging have been performed in *in vitro* cell tests, only fluorescent images have been obtained in *in vivo* animal studies of brain circulation, and without MRI results, the *in vivo* application of the Gd–QD composites cannot be evaluated.

Paramagnetic lipids generated by chelating Gd ions with lipid molecules have been combined with QDs to obtain paramagnetic micelles. After conjugation with annexin A5 proteins, the resulting nanocomposites can be utilized for the detection of apoptosis cells *in vitro* using both fluorescent microscopy and MRI [90]. Recently, the same structured nanocomposites have been intravenously administered into tumor–bearing mice for *in vivo* molecular multimodal imaging of tumor angiogenesis after conjugation with RGD peptides [91, 92]. The results demonstrate that the use of the paramagnetic QD nanocomposites for tumor angiogenesis imaging

achieves both cellular and macroscopic level (Fig. 2.2).

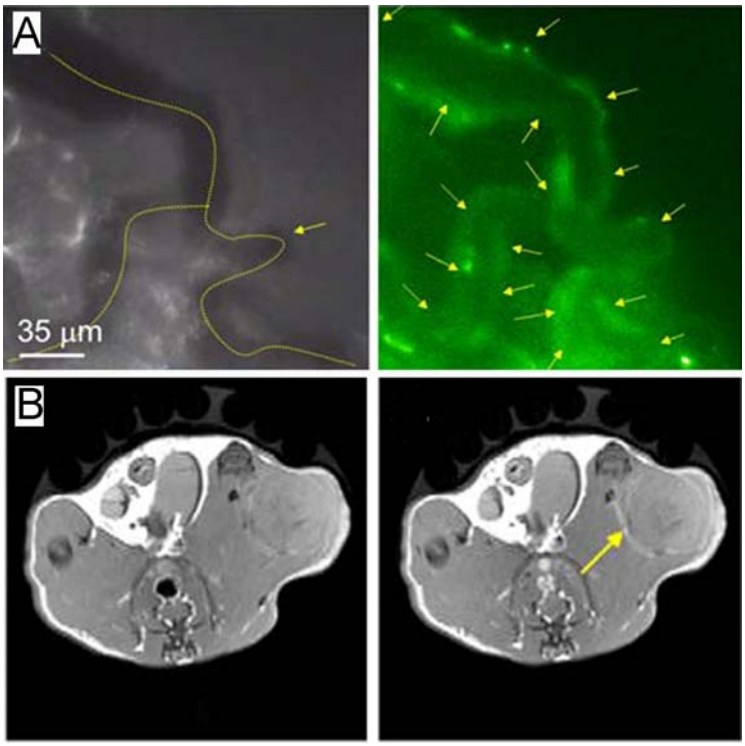

Figure 2.2 (A) Bright–field and fluorescent images of tumor blood vessels labeled with RGD–paramagnetic polymer–QD nanocomposites. (B) MRI of tumor angiogenesis before (left image) and 45 min after (right image) the injection of the RGD–paramagnetic polymer–QD nanocomposites. (Reproduced from Ref. [91, 92])

Various strategies have been developed to couple magnetic nanoparticles (MNPs) and QDs for the fabrication of nanocomposites with both magnetic and fluorescent properties, which have application in facile target recognition, enrichment, and sorting [39, 93, 94]. Although MNPs are high–contrast nanoprobes for MRI, the application of MNP–QD nanocomposites in multimodal imaging is greatly hampered by MNP–caused fluorescence quenching [94]. The QY of a silica–encapsulated

MNP–ZnS/CdSe QD nanocomposite is only 4.8%, significantly lower than the original 14.5% of ZnS/CdSe QD [94]. However, a recent study was able to increase the QY of an Fe_2O_3–CdSe nanocomposite up to 42% [95] by linking Fe_2O_3 MNPs with CdSe QDs via hydrophobic force without the use of a silica coating shell to eliminate the influence of silica on QD fluorescence. Additionally, because several QDs encapsulate one MNP with a space when using this approach, it may limit the fluorescence quenching of MNP. The newly synthesized Fe_2O_3–CdSe nanocomposite may be a promising material in simultaneous fluorescent and MRI imaging. When Fan *et al.* synthesized QD–capped magnetite nanorings with a high level of luminescence and a magnetic vortex core they found that the prepared nanorings exhibit much stronger magnetic resonance than do commercial superparamagnetic MNPs. As they have also been demonstrated useful in the fluorescent imaging of composite–labeled bladder cancer cells, QD–capped magnetite nanorings are promising materials for dual–modal imaging.

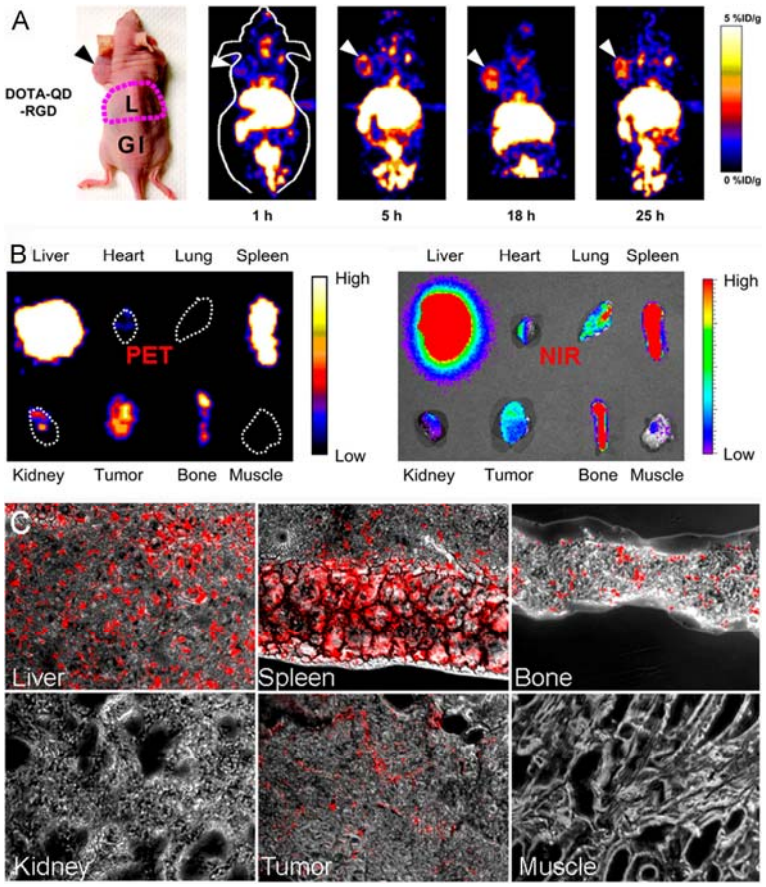

Figure 2.3 (A) *In vivo* PET of tumor–bearing mice after the injection of QD–DOTA–RGD at different times. (B) *Ex vivo* PET (left) and NIR fluorescent (right) images of harvested tissues and tumors 5 hr after injection of QD–DOTA–RGD. (C) Histological analysis of QD–DOTA–RGD distribution in tumors and other tissues. (Reproduced from Ref. [96])

PET is a nuclear medicine imaging technique whose use provides highly sensitive and quantitative data. Gambhir et al. have conjugated ^{64}Cu with near–infrared–emitting QDs to enable micro–PET imaging [97] while probing the *in vivo* biodistribution of QDs. However, multimodal imaging property, especially fluorescence imaging, has not been shown in the study. The first QD nanocomposite found successful for PET–fluorescence dual–modal imaging was synthesized by

Chen and coworkers in 2007 by modifying near–infrared emitting QDs with RGD peptides and 1,4,7,10–tetraazacyclodocecane–N,N′,N″,N‴–tetraacetic acid (DOTA) ^{64}Cu chelators (Fig. 2.3) [96]. The researchers investigated time–dependent tumor targeting and nanocomposite biodistribution in different organs with *in vivo* PET images and *ex vivo* fluorescence/PET images, respectively, and performed histological imaging of the QD–emitted fluorescence to identify the location of QD–DOTA–RGD in the tumor and other tissues at the cellular level. Their work clearly demonstrates that using PET together with fluorescence imaging provides more complete biomedical data from different angles.

2.4.2 QD Nanocomposites for Drug Delivery

Due to the large surface area of nanomaterials, allowing the loading of large quantities of drugs, and their small size, allowing *in vivo* transportation of drugs, the design of nanomaterial–based drug delivery systems is one of the most active research areas in nanotechnology. To overcome the great challenge of monitoring the *in vivo* or intracellular location of drug carriers, QDs have been composited into drug delivery systems for efficient tracking of the drug carriers [21, 98].

Polymers have been used to capsulate both QDs and drugs to create a drug delivery nanocomposite in which the side chains of the polymer molecule not only provide functional groups for probe conjugation but also enhance the dispersion of the nanocomposites in aqueous solutions. Biodegradable poly (D,L–lactic–co–glycolic acid) has been employed to encapsulate CdSe/ZnS

nanocrystals and doxorubicin, an anti–cancer drug. After functionalization with folate, the polymer capsules with sizes ranging from 100 nm to 200 nm can target *KB* cancer cells *in vitro* [99]. Chitosan, another natural biodegradable polymer, has also been used to fabricate QD–drug–loading polymer nanocapsules. The *in vitro* release profiles in phosphate buffer solution show that the drug release from the nanocomposite lasts for several days, indicating its high capacity for sustained release [100]. To further control the drug release, a nanogel containing pH–sensitive poly(acrylic acid) has been applied as a matrix to encapsulate QDs and drugs, with the pH–dependent drug release from the nanocomposite being observed through changes in the degree to which the nanogel swells [101]. An intelligently designed QD–aptamer drug delivery system in which aptamers are covalently linked on the surface of QDs to enable drug loading and target cell recognition would be able to not only image the location of the drug carrier but also measure the release of the drugs. Formation of the nanocomposites causes the quenching of QD fluorescence via Föster resonance energy transfer (FRET) between QDs and doxorubicin. The recovery of the QD fluorescence was examined to sense the drug release profile [102].

One active research area has been the investigation of the impact of the nanostructures serving as drug carriers on the drug–loading capacity of various pharmaceuticals. Using mesoporous silica nanotubes composed of CdS QDs for drug delivery has been found to allow the pharmaceutical ibuprofen to reach a level of

740 mg/g silica, significantly higher than those that can be reached using other structured silica nanomaterials [103]. Another tube–shaped drug delivery system made by conjugating QDs to carbon nanotubes [104] has been demonstrated to have a high level of loading efficiency for the anticancer reagent paclitaxel, with the sole concern with its use being that the carbon nanotube may quench QD fluorescence.

QD–based drug delivery systems with magnetic properties have also been investigated. Very recently, Chen and Liu *et al.* reported on the use of a nanocomposite consisting of a drug–loading polymer core, a single crystal Fe_3O_4 shell, and Zn–Cu–In–S QDs attached to the shell that is capable of imaging, magnetically controlling, and monitoring drug release *in situ* (Fig. 2.4) [105]. Upon high–frequency magnetic field treatment, the single crystal nanoshell undergoes lattice deformation to form polycrystals with various orientations, resulting in drug release from the core. Because the magnetically induced temperature increment causes surface oxidation as well as QD photobleaching, the drug release process is correlated with fluorescence reduction. Therefore, as drug release from the nanocomposites is triggered by the surrounding magnetic field, the process can be monitored *in situ* by measuring the QD fluorescence, a practical principle that has been demonstrated in drug therapy targeting *HeLa* cancer cells.

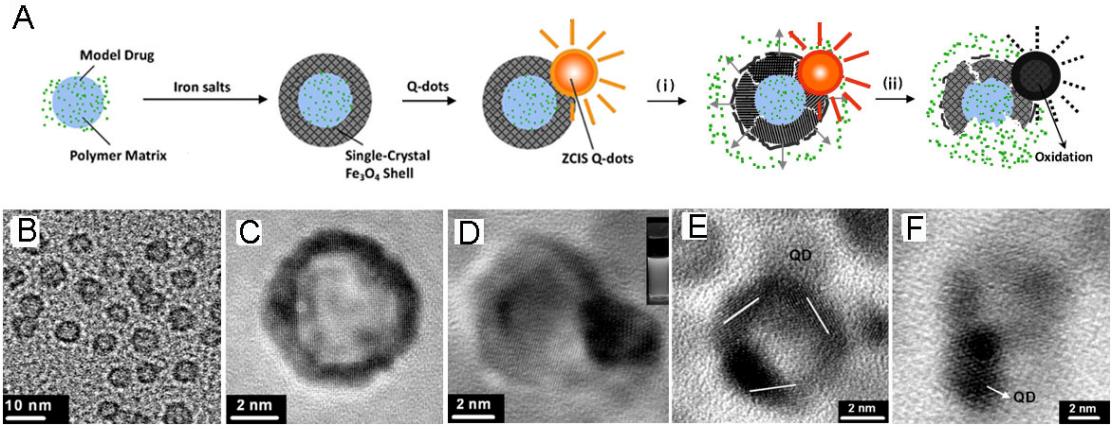

Figure 2.4 A polymer Fe_3O_4–QD–composited multifunctional nanodevice capable of imaging, magnetically controlling, and monitoring drug release *in situ*. (Reproduced from Ref. [105])

As current research into QD nanocomposite–based drug delivery systems remains at the infant stage, it is primarily limited to *in vitro* testing. Even though cultured cell testing has verified the specificity of the nanocarriers, a culture medium cannot adequately mimic the *in vivo* environment in the animal or human body, calling for *in vivo* animal testing for further investigation of the transport, targeting, drug–release, and therapeutic effectiveness of QD nanocomposite–based drug carriers that allow for monitoring via measurement of QD fluorescence.

2.4.3 QD Nanocomposites for Cancer Therapeutics

Conventional treatments and pharmaceuticals for cancer, the second leading cause of death worldwide, severely damage not only cancerous tissue, their intended target, but also healthy tissue. Thus, the development of nanomaterials with unique properties that can specifically target tumor cells without harming healthy cells is a

primary research objective. As an external magnetic field could greatly enhance the environmental temperature surrounding MNPs, these particles are promising nanomaterials for hyperthermia therapy. MNPs and fluorescent QD nanocomposites fabricated for multimodal imaging have been employed for magnetic field–assisted therapeutics [106-108] in which QDs served as fluorescence labels for imaging.

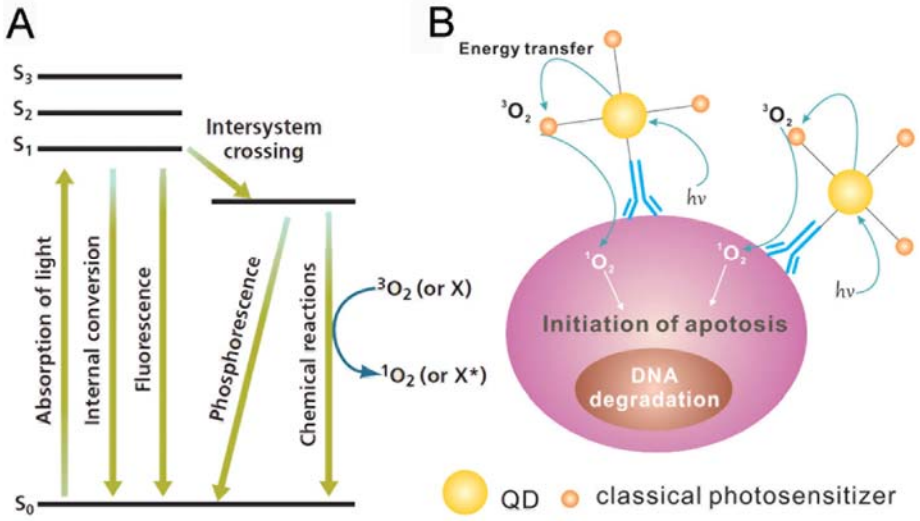

Figure 2.5 Photodynamic cancer therapy using QD–photosensitizer nanocomposites. (Reproduced from Ref. [118])

Burda *et al.* has synthesized a QD–phthalocyanine nanocomposite for photodynamic therapy in which QDs function as energy donors transferring energy to phthalocyanine under irradiation. After gaining energy from the QDs, the photosensitizers become excited and react with the nearby oxygen molecules to generate reactive singlet oxygen ($1O_2$), which induce cytotoxic effects that kill surrounding tumor cells [109]. Although several studies have demonstrated that this

process occurs with the use of several QD–photosensitizer nanocomposites (Fig. 2.5) [110-114], these studies were limited to investigation of the optical properties of the nanocomposite and the measurement of reactive oxygen, and did not evaluate the use of the nanocomposites in practical clinical applications. Clearly, conducting *in vitro* cell assays and *in vivo* animal tests is of great importance for gaining greater understanding of the biological responses of the target cells or tissues to the nanocomposites.

2.5 QD Nanocomposites for Specific Biomedical Applications

In recent years, QDs have been combined with other components to expand their biosensing applications and enhance the sensitivity and specificity of their biosensing capability. After linking one QD to one gold nanoparticle with a sequence–designed single strand DNA molecule for the fabrication of a nanoparticle–based molecular beacon, as shown in Fig. 2.6a [115], it has been found that the gold nanoparticle in the resulting hairpin structure greatly quenches the QD fluorescence through FRET because the two ends of DNA are brought very close to one another. However, after the target DNA hybridized with the loop part of the molecular beacon, the hairpin structure could not form, increasing the distance between the QD and the gold nanoparticle greatly beyond the Föster radius, and thus restoring QD fluorescence.

One test of DNase or proteinase activity based on the same principle uses an

enzyme–sensitive DNA or protein to link the QD and gold nanoparticle [116]. The digestion of the protein or DNA separates the QD and gold nanoparticle, resulting in fluorescence recovery. A dual–color sensor for the detection of double–strand DNA has been designed using a QD–ruthenium (Ru) complex nanocomposite (Fig. 2.6b) in which QD fluorescence is quenched by the Ru complex. Due to its strong affinity with the Ru complex, the double–strand DNA destroys the nanocomposites and frees the QDs. The fluorescence from the double–strand DNA incorporated Ru complex and the QD fluorescence result in dual–emission detection [117]. In the design of QD–nanocomposite biosensors based on FRET, the QD emission should be carefully matched to the acceptor fluorophore absorbance and the length of the linkage materials should be delicately adjusted to achieve the highest level of FRET efficiency.

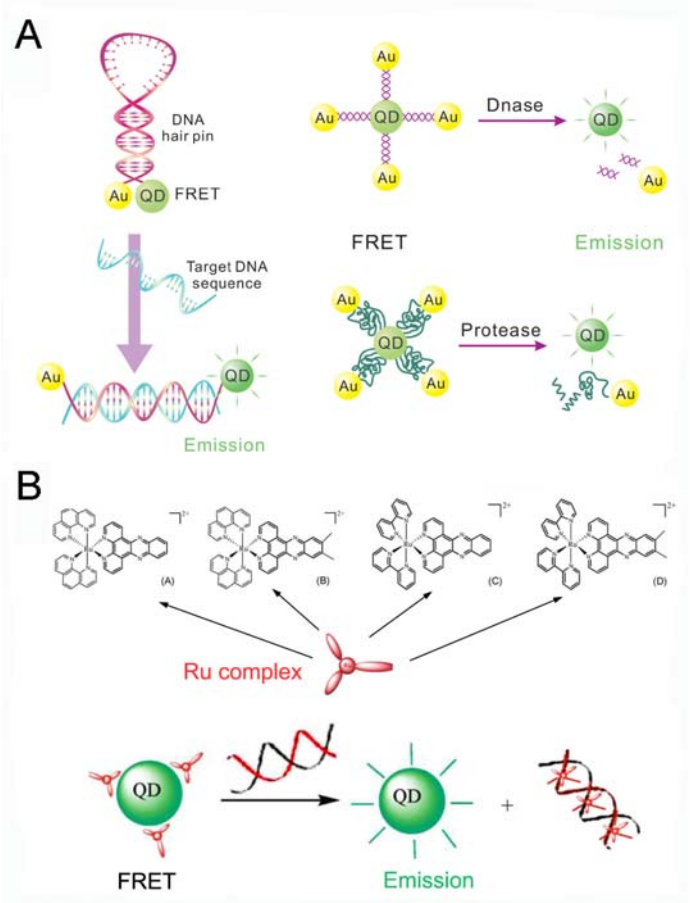

Figure 2.6 (A) Molecular beacon constructed with QD–gold nanoparticle nanocomposites for DNA hybridization detection and DNase or proteinase activity measurement. (Reproduced from Ref. [115, 116]) (B) QD–Ru complex dyads for dual–color fluorescence detection of double–strand DNA. (Reproduced from Ref. [117])

As one of the best light–harvesting materials, QDs have been hybridized with CNT, TiO_2, and graphene to produce QD–based photoelectrochemical solar cells [118-124]. Light irradiation can induce the dissociation of electrons and holes in the conduction and valence bands of QDs, respectively. Based on the principle that electrons inject into the electrode to produce a photocurrent when the band energy is favorable and that holes are scavenged by suitable electrolytes to regenerate QDs (Fig. 2.7), QD–based photoelectrochemical sensors can be fabricated by measuring

the change in the photocurrent. In a CdS/CNT/glutamate dehydrogenase hybrid biosensor, the electrons generated from the dehydrogenase enzymatic reaction in the presence of glutamate combine with the light–induced holes in the valence bands of QDs to generate a stable photocurrent, with any increases/decreases in the level thereof indicating the concentration of glutamate in the sample [125].

In a photoelectrochemical CdS–TiO_2 nanocomposite sensor constructed for the detection of a cancer biomarker, the capture of the biomarker by the pre–immobilized antibody significantly reduces the photocurrent due to the blockage of electron transfer from the electron donor to the electrode (Fig. 2.7) [126]. Using a similar mechanism, a recent study has fabricated a CdS–polyamidoamine nanocomposite film for the detection of cell capture [127]. This means of QD nanocomposite–based photochemical measurement is a label–free approach suitable for the detection of any antibody–antigen pair. As nanotechnology research continues to advance, a greater number of biocompatible and energy favorable QD nanocomposites will be developed and applied to enhance detection and diagnostic sensitivity and specificity.

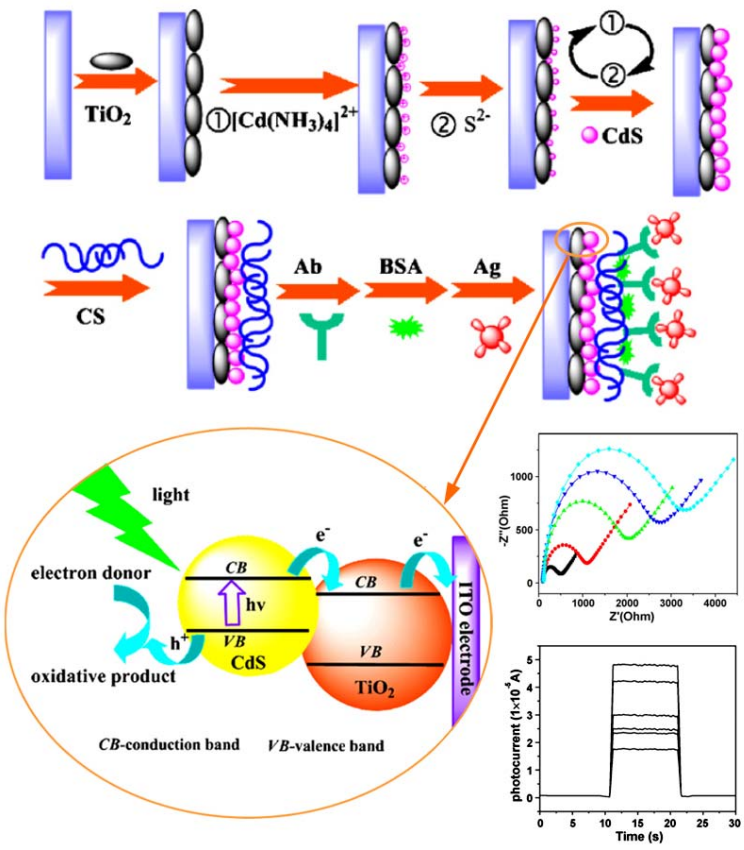

Figure 2.7 QD–nanocomposite biosensor based on photoelectrochemistry. Inset shows the photocurrent generation mechanism of a CdS–TiO_2 electrode. (Reproduced from Ref. [126])

QD–based multicolor–encoded nanocomposites serving as barcodes for biomolecular or bioreaction coding provide a rapid and high–throughput analysis platform for the development of multiplex biosystems. In 2003, Sha *et al.* [128] reported the first use of a QD barcode system in the biomedical field, describing the development of barcoding composites with unique emission spectra and intensities produced by controlling the ratio of various QDs on latex microspheres employed for single nucleotide polymorphism genotyping. As shown in Fig. 2.8(a), different emission patterns indicate the single nucleotide change in the DNA sequences and, if

considered in tandem with the hybridization signal, the genotype of the original DNA can be automatically analyzed with flow cytometry. The barcodes have also been applied to encode DNA hybridization and multiplex immunoreactions [129, 130]. In principle, this QD–based barcode system could provide numerous states for biolabeling if the detection instrument has sufficient resolution, thus greatly facilitating the high–throughput assay of multicomplex biosystems, such as genome, transcriptome, and proteome systems.

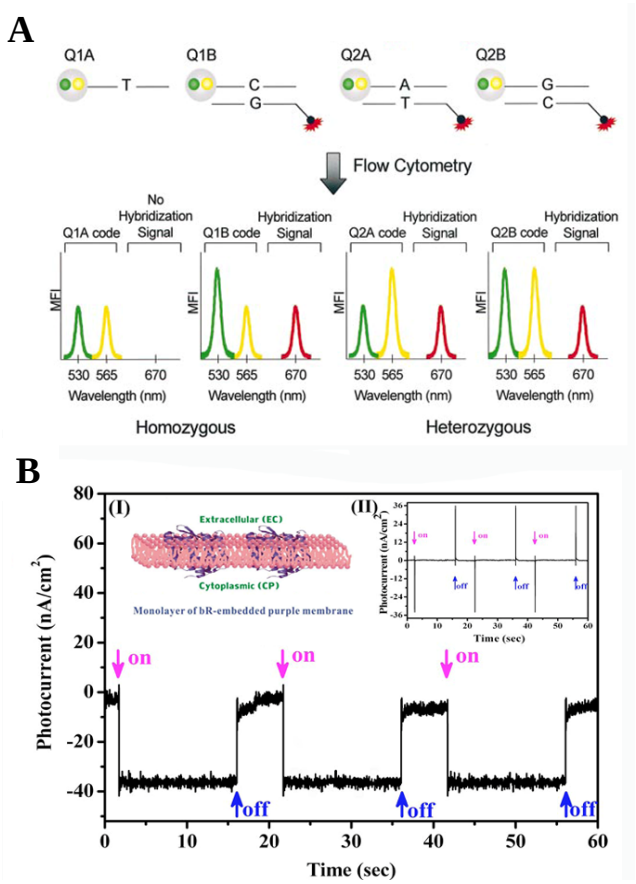

Figure 2.8 (A) QD–based multicolor–encoded nanocomposites serving as barcodes for single nucleotide polymorphism genotyping. (Reproduced from Ref. [128]) (B) Stationary current generated from the photocycle of a hybrid bacteriorhodopsin/QD bionanosystem. (Reproduced from Ref. [131])

Continued development of nanomaterials may lead to the identification of unique biosystem properties that allow for the development of specific biomedical applications. For example, the light absorption of bacteriorhodopsin, a protein component of the cytoplasmic membrane of *Halobacterium salinarum*, has been shown to trigger a change in protein conformation that results in light–driven proton transportation from the cytoplasmic to the extracellular side of the membrane. Normally, the light irradiation induces a transient photocurrent with a spike shape, but a stationary photocurrent has been observed in hybrid QD/bacteriorhodopsin bionanocomposites. This emission from the excited QDs has been proposed to be involved in the protein state change that further contributes to the new pattern of photocurrent (Fig. 2.8) [131]. These findings may inspire other uses of QDs in the performance improvement or functional change of biocomponents, ultimately leading to the fabrication of intelligent bionanohybrid devices for medical applications.

2.6 Perspectives

Although two studies to date have investigated the antimicrobial activity of QDs, both focused solely on CdSe–core QDs. Since the core materials determine the chemical and physical properties of QDs, further affecting their interaction with microbes, it is of great importance to study the antimicrobial activities of QDs composed of other core materials. One challenge is that research into QD

antimicrobial effects has been limited to determination of the survival rate of bacteria exposed to QDs. Research should be expanded to exploration of the effects of QDs on cellular antioxidative systems, as well as identification of the biomolecular and photophysical mechanism behind QD antibacterial properties.

Coating QDs with polymer and silica is currently considered the best means of reducing heavy metal leaching from QD cores, but has been observed to decrease QY in most cases. The development of novel biocompatible coating materials that can maintain or enhance QD fluorescence is therefore of great research interest. Another research goal is the development of an environmentally friendly approach for the one–step synthesis of biomolecule–coated QDs in order to simplify the fabrication process.

The design of QD nanocomposites should not only focus on the selection of components with different functions but also exploration of the components' unique shapes and/or nanostructures for specific applications, such as drug delivery and *in vivo* targeting. As spherically shaped nanocomposites without rigidly controlled nanostructures have been developed by simply encapsulating QDs within other components, future research should focus on the fabrication of QD–based nanocomposites of various unique shapes and engineered nanostructures to improve the performance of bioimaging and biosensing applications, especially *in vivo* drug delivery and therapy.

Although the biocompatibility and biomedical utility of nanocomposites in such

fields as biosensing, multimodal imaging, diagnostics, and therapy have been demonstrated, great challenges must be overcome before they can be used in clinical therapeutics and nanopharmaceuticals. More *in vivo* animal studies must be conducted to investigate the effects of the complex real–world biological environment on nanocomposite–based biodevices, and the pharmacokinetics, protein adsorption, biodistribution, degradation, and excretion pathways of QD–based nanocomposites must be identified to advance understanding of the *in vivo* behaviors of QD nanocomposites and to limit their nanotoxicity.

Currently available QD–composited materials are mainly limited to those composed of polymers and/or inorganic nanocrystals. It is of great research interest to compose QDs of various biomolecules for application to multiple biosensing, bioimaging, and drug delivery systems, particularly specific biomolecule–modified or composed QDs that can be used to study complex biological processes at the intra– and intercellular levels.

As the nanocomposing of QDs with various novel nanomaterials for unique functions progresses, more attention will be focused on novel nanomaterials and their specific applications. For example, graphene, an especially promising nanomaterial with excellent optical, mechanical, and electronic properties [118, 132, 133], has been integrated with QDs to fabricate FRET–based biosensors and used in drug delivery systems [134-136]. A QD–graphene complex has great potential as the basis of intelligent multifunctional biomedical nanodevices.

With considerable research effort, the compositing of QDs with various nanomaterials and biomolecules will lead to the development of nanocomposites for functions beyond fluorescence labeling, thus extending the application of nanocomposites in the study of biological, physiological, pathological, and pharmacological processes. The future commercialization of QD nanocomposites could provide extraordinary health and economic benefits to individuals, society, industry, and the economy.

Chapter 3 Experimental Approaches

3.1 Materials and Equipment

3.1.1 Reagents and Chemicals

3.1.1.1 Chemicals

Sodium tellurite (100 mesh, 99%), mercaptosuccinic acid (MSA), sodium borohydride (99.995%), Rhodamine 6G, peptone, yeast extract, sodium chloride, agar, cytochrome c, L–cysteine, agarose, 3–(4,5–dimethylthiazol–2–yl)–2,5–diphenyl tetrazolium bromide, hemoglobin, glucose oxidase, zirconium propoxide, cyclohexane, n–hexanol, and ethanol (anhydrous, ≥99.95% pure) were purchased from Sigma–Aldrich; cadmium chloride hemipentahydrate was purchased from Acros Oganics; and sodium citrate tribasic dihydrate was purchased from Fluka. All chemicals were of analytical grade and used without further purification, and all water was deionized using a Millipore system before use.

3.1.1.2 Reagents and Kits

TRIZOL reagent (Invitrogen, USA), First–Strand Synthesis System (Invitrogen, USA) and PCR Master Mix (Takara, Japan) were used to conduct genetic analysis. All primers for PCR were ordered from Sigma–Aldrich.

3.1.1.3 Buffers and Medium

The Lysogeny broth (LB) medium for *E. coli* growth was prepared as following: 10 g of NaCl, 10 g of Tryptone, and 5 g of yeast extract were stirred into 900 mL of deionized water, and the subsequent mixture was adjusted to a 7.4 of pH with the addition of NaOH. After the addition of the chemicals, the volume was then adjusted to 1L with deionized water and sterilized by autoclaving (120°C, 20 min).

The following buffers were used in agarose gel electrophoresis:

(1) The 6× loading dye buffer consisted of the following:

6 mL	Glycerol
1.2 mL	0.5 M EDTA
0.009 g	Xylene cyanol
2.8 mL	deionized H_2O

The loading dye buffer was mixed with PCR products at a ratio of 1:5.

(2) The 0.5× tris–borate–EDTA (TBE) running buffer consisted of the following:

54 g	Tris base
27.5 g	Borate
20 mL	0.5 M EDTA
10L	deionized H_2O

(3) The 1.2% agarose gel was prepared by dissolving 0.6 g of agarose into 50 mL of 0.5× TBE buffer.

The buffers used in the SDS–PAGE included sample buffer, running buffer, and running gel solution.

(1) The 5× sample buffer, a protein sample preparation, was mixed with protein at a ratio of 1:4 and consisted of the following:

10% w/v	SDS
10 mM	Dithiothreitol, or beta–mercapto–ethanol
20 % v/v	Glycerol
0.2 M	Tris–HCl, pH 6.8
0.05% w/v	Bromophenolblue

(2) The 1x running buffer for electrophoresis was prepared by dissolving 3.01 g of Tris base, 14.4g of Glycine, and 1g of SDS into 1L of deionized water.

(3) The running gel solution (12%) used for resolving the gel preparation consisted of the following:

H_2O	1.2 ml
1.5 M Tris–HCl, pH 8.8	3 ml
10% (w/v) SDS	40 µl
Acrylamide/Bis–acrylamide (30%/0.8% w/v)	3.1 ml
10% (w/v) ammonium persulfate (APS)	40 µl
TEMED	5 µl

The stacking gel was prepared by mixing 1ml of Acrylamide/Bis–acrylamide (30%/0.8% w/v), 630µl of Tris–HCl (1M, pH6.8), and 25 µl of 10% SDS into 3.6 ml of deionized water, and then adding 25 µl of 10% APS and 5 µl TEMED just before gelling occurred.

3.1.2 Equipment

Field–emission scanning electron microscopy (FESEM) (JSM–6700F JOEL, Japan) was used to characterize the material and cell morphologies.

Atomic force microscopy (AFM; SPM 3100, Veeco Instruments Inc., USA) was used to characterize the surface morphologies of the treated/non–treated bacteria.

Fourier transform infrared (FTIR) spectroscopy was conducted using the Nicolet

Magna IR 560 ESP spectrophotometer (Thermo Nicolet, USA).

X–ray diffraction (XRD) spectra were collected at room temperature on a Bruker AXS X–ray diffractometer (USA) using Cu Kα radiation (λ =1.5418 Å) with a θ–2θ scan configuration.

UV–visible (UV–VIS) spectra were measured on a HITACHI U–2800 double–beam system.

Photoluminescence (PL) spectra of different QDs and QD composite suspensions were collected using an Aminco Bowman II luminescence spectrometer (Thermo Electron, USA) with an illumination source at 350 nm.

Fluorescent images and time–series images were acquired with a Zeiss LSM 510 Meta confocal microscope (Carl Zeiss, Germany).

RNA and cDNA sample quality control were maintained using a NanoDrop^{TM} 1000 Spectrophotometer (Thermo Scientific) and an Agilent 2100 Bioanalyzer (Agilent Technologies).

Hydrodynamic size and zeta potential were recorded using a Nano–ZS instrument (Malvern Instruments Ltd., UK).

3.1.3 Other Materials

E. coli K12 (ATCC 29181), *HeLa*, *PC 12,* and *Raw 264.7* cells were purchased from ATCC (USA).

3.2 Methodology

The methods used in the majority of the experiments described in several chapters are summarized here. The specific experimental approaches used in only one chapter are described in the corresponding chapter.

3.2.1 CdTe QD Synthesis

Highly fluorescent MSA–capped CdTe nanocrystals were synthesized according to Bao's route [137]. Briefly, 2 mL of cadmium chloride solution (0.08 M) was diluted within 40 mL of deionized water, and then 100 mg of trisodium citrate dehydrate, 2 mL of sodium tellurite (Na_2TeO_3) solution (0.02 M), 100 mg of sodium borohydride, and 25 mg of MSA were added under vigorous stirring. The solution was loaded into a 50 mL Teflon–lined stainless steel autoclave and then maintained at 180 °C for 45 min. During preparation, the oxygen in the solution did not need to be removed because the Te source, Na_2TeO_3, is stable in air. Before conducting antimicrobial assays, freshly synthesized QDs were washed three times in 50% ethanol by centrifugation (4000 g, 5 min) to remove residual chemicals. The pigmented layer was suspended into a phosphate–buffered solution (PBS, pH 7.4) and diluted to desired concentrations.

3.2.2 Material Characterization

In this study, FTIR was used to survey the functional groups on the surfaces of nanomaterials and conduct spectral analysis of cell supernatant. FTIR spectra were

recorded in the range of 400 to 4000 cm^{-1} using a Nicolet Magna IR 560 ESP spectrophotometer.

XRD was used to characterize the crystallographic structure of nanomaterials. The wide–angle XRD patterns were measured from 5 to 90 degrees (2θ) at a scan rate of 0.5 degree min^{-1}.

The morphological studies were conducted using FESEM, HRTEM, and AFM, with the morphologies of nanomaterials observed using FESEM and HRTEM and the surface morphologies of *E. coli* cells observed using AFM (in contact mode) and FESEM.

The hydrodynamic sizes of QDs, proteins, and QD–protein combinants were measured at 25 ^{o}C at an equilibration time of 3 min. To obtain zeta potential measurements, sample solutions were centrifuged at 2,000 g for 5 min before the study. Each sample was tested three times at 25 ^{o}C at an equilibration time of 5 min.

3.2.3 Cell Culture

The cells were cultured in Dulbecco's Modified Eagle's Medium (DMEM) or RPMI 1640 medium supplemented with 10% FBS in a humidified atmosphere containing 5% CO_2 at 37^{o}C.

3.2.4 Characterization of Cell Surface

The *E. coli* cell cultures were harvested by centrifugation at 5000×g, 4℃. After

three washes, the cell pellets were resuspended in a 0.05 M phosphate buffer. For the FESEM observation, the cell pellets were resuspended in a 0.05 M phosphate buffer containing 5% glutaraldehyde as a fixative and fixed for 4~6 hrs. The fixed cell suspensions were then dropped onto the substrate, a piece of filter membrane with a pore size of 100 nm. After drying in the incubator, the membranes with the cells were gradually dehydrated using 30%~100% ethanol and dried in a vacuum oven at room temperature. Before observation, the membranes were coated with Pt to make them conductive. For the AFM observation, the cells did not need pretreatment. The cell suspensions were dropped onto mica and rinsed with deionized water several times and, after air–drying, could be directly observed.

3.2.5 Biocompatibility Testing

Briefly, cells were seeded into a 96–well culture plate and grown for 24 hrs. QDs and QD nanocomposites were then added into each well at different concentrations. After another 24 hrs, the cells were treated with MTT reagent to form purple–colored formazan. After dissolving formazan in DMSO, a BioTek microplate reader was used to measure the absorbance at 570 nm.

Chapter 4 Bactericidal Activity of CdTe QDs and Its Mechanism[a]

4.1 Introduction

Although there are several reports on antimicrobial activities of QDs [28, 29], all studies focus on the antimicrobial effects of CdSe–core QDs. QDs with different core materials may have a distinct interaction with microbes as their chemical and physical properties play vital roles in bioactivities. It is of great importance to investigate the antimicrobial activities of QDs composed of other core materials. The mechanism of the interaction between nanoparticles and bacteria needs to be better understood. Although ROS has been proposed to be a key player in mediating the antimicrobial activity of QDs [28, 29], the studies so far are still limited to determine the survival rate of bacteria exposed to QDs. The effects of QDs on bacterial antioxidative response, biomolecule oxidative damage, and the biological molecular mechanism of QDs' antibacterial properties have not been studied yet.

In this study, the investigation of the bactericidal activity and mechanism of CdTe QDs, one of the most widely used QDs, is reported. The binding capability of the QDs on the surface of *E. coli* is explored to verify the diffusion pathway of ROS. Further, the negative influences of the QDs on the antioxidative system were

[a] Reproduced in part with permission from [Z. S. Lu, C. M. Li, H. F. Bao, *et al.*, *Langmuir*, 24 (2008), 5445–5452.] Copyright[2008] with permission from American Chemical Society

systematically studied by measuring oxidative damage of *E. coli* cells and determining expression levels of related genes and activities of antioxidative enzymes. Based on the results, I proposed a biomolecular mechanism to explain the bactericidal activity of CdTe QDs.

4.2 Preparation and Measurement

4.2.1 Bacteria Growth and CdTe QDs Treatment

The synthesized CdTe QDs with orange emission and good physical and optical properties were used in the following tests (Fig. 4.1). Before conducting bactericidal assays, freshly synthesized QDs were washed three times in 50% ethanol by centrifugation (4000 g, 5 min) to remove residual chemicals. The pigmented layer was suspended into PBS (pH 7.4) and diluted to desired concentrations. *E. coli K12* (ATCC 29181) was cultured with aeration at 37°C in an LB medium. The culture mixtures with an absorbance of 0.6 at 600 nm (approx 6×10^8 cells per mL) were centrifuged at 4000 g for 10 min to collect the cells. After being washed, the bacteria were suspended in PBS again to obtain the original absorbance. QDs were dropped into the suspensions, followed by incubation at 37°C for 2 hrs.

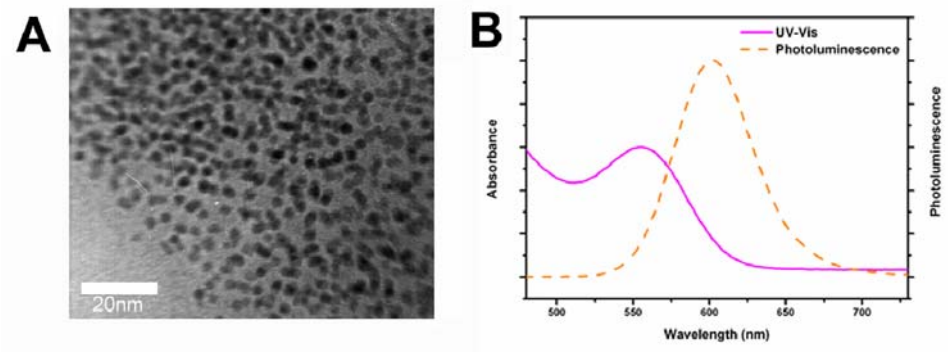

Figure 4.1 (A) TEM image of a large population of orange emission MSA–coated QDs. (B) UV–vis and PL spectra of synthesized orange–emitted QDs.

4.2.2 Colony–Forming Capability Test

After being exposed to different concentrations of QDs at 37°C for 2 hrs, *E. coli* suspensions were diluted to 2×10^3 cells per mL. 100 μL of the cell suspension was spread onto LB agar plates. After agar plates were incubated at 37°C in the dark for 12 hrs, the number of the colonies was counted to evaluate the bactericidal effect of QDs. Survival percentage was defined as the following formula:

$$\text{Survival\%} = \frac{\text{Colony numbers of treated bacteria}}{\text{Colony numbers of control bacteria}} \times 100\%$$

4.2.3 Semi–Quantitative Reverse Transcription Polymerase Chain Reaction (RT–PCR) Assay

Total RNA samples were extracted from nontreated and QDs–treated bacteria, respectively, using TRIZOL reagent. The reverse transcription was conducted by using a first–strand synthesis system to produce cDNA. The sequences of the

primers for PCR were shown in Table 4.1. After incubation at 94°C for 5 min, PCR amplification was performed for 30 cycles. Agarose gel (1.2%) electrophoresis was carried out to separate the amplified products, which appearing as bands with the predicted sizes in the gels were visualized under the UV light after being stained with ethidium bromide. The intensity of each band was determined using LabImage software (Kapelan GmbH, Bio–Imaging Solutions, Germany). The net intensity of the 16S rRNA gene was used to normalize the data to correct any error in the amount of input RNA.

Table 4.1. PCR primers for antioxidative genes

Gene name	Sequence (5' > 3')	Bases (bp)	Products (bp)
sod A upper	AGCTGATCACCAAACTGGACC	21	194
lower	CGCTTTTTCAAATTCTGC	18	
zwf upper	AATGTTCTGAAGTCGTGGTCT	21	218
lower	ATGCGTCTGATTAAAGGTT	19	
nfo upper	ATGCCTTTATAGATGAAATGC	21	217
lower	AGATGTTCGAATTTAAACCC	20	
16S upper	CGCAAGGTTAAAACTCA	17	541
lower	TACTTCTTTTGCAACCCACTC	21	

4.2.4 Enzyme Activity Assay

Proteins were extracted from the treated and non–treated bacteria using freeze

thaw method. After centrifugation, the protein supernatants were collected and used in the following enzyme activity assays.

The peroxidase activity was measured in reaction mixtures containing 10 mM H_2O_2, 1.6 mM o–diarising and 40 mM 3–amino–1,2,4–triazole in 50 mM potassium phosphate + 0.5 mM EDTA with pH 7.0 at 25°C. After 20 µL of protein supernatant was added into the mixture, the change of the absorbency at 436 nm was measured for 60 s. One unit of the peroxidase activity was defined as one optical change at 436 nm/min.

The activity of superoxide dismutase (SOD) was assayed by the xanthine oxidase/cytochrome c method [138]. The reaction mixture contained 10 mM cytochrome c and 50 mM xanthine in 50 mM potassium phosphate + 0.1 mM EDTA with pH 7.8 at 25°C. The reduction of cytochrome c by superoxide anion was measured by UV–vis spectrometry at 550 nm. Reactions were started by adding xanthine oxidase in an amount sufficient to cause an absorbance change of 0.025/min at pH 7.8. One unit of the SOD activity was defined as a 50% decrease in the rate of cytochrome c reduction.

4.2.5 Measurement of Protein Carbonyl and Lipid Peroxides

Contents of protein carbonyl were detected by the reaction with 2,4–dinitrophenylhydrazine (DNPH) [139]. The product, 2,4–dinitrophenylhydrazone, was spectrophotometrically quantified at 370 nm. 200 µL of the protein supernatant was mixed with 1mL of 10 mM DNPH in 2 M HCl.

The control sample contained 1 mL of 2 M HCl instead of the DNPH solution. Samples were incubated in the dark for 1 hr, vortexing every 10 min. After adding 500 μL of 10% trichloroacetic acids (TCA), mixtures were centrifuged for 15 min at 12,000 g. The pellets were collected and washed three times with 1 mL of ethanol–butylacetate (1:1 v/v). Then, pellets were dissolved in 1.5 mL of 6 M guanidine–HCl and centrifuged as above. The supernatant was collected, and its absorbency was measured at 370 nm. Carbonyl content was expressed as micromoles of carbonyl per milligram of protein with a molar extinction coefficient of 22.0 mM^{-1} cm^{-1}.

Products of lipid peroxidation were measured by the thiobarbituric reacting substances (TBARS) assay [140]. The TCA–treated cell suspension was centrifuged for 10 min at 4,000 g. The supernatant was mixed with 2 mL of 20 mM butylated hydroxytoluence and saturated thiobarbituric in 0.1 M HCl. After being heated at 100°C for 60 min, a 1.5 mL aliquot was chilled with ice followed by mixing with 1.5 mL butanol. The mixture was centrifuged for 10 min at 4,000 g to collect the supernatant for spectrophotometrically measurement at 535 nm. Contents of TBARS were presented as picomoles per milligram of protein by applying a molar extinction coefficient of 156 $mM^{-1}cm^{-1}$.

4.2.6 Data Analysis

All tests were repeated in independent experiments. Differences between different groups were tested for significance using Student's t-test (Origin 6.0). The

"p" value is a probability with a value ranging from zero to one. When p value is less than 0.05, the result is statistically significant.

4.3 Concentration–Dependent Bactericidal Activity of CdTe QDs

The Gram–negative bacterium *E. coli* is selected as the testing microbe since it is a well–studied model organism in antimicrobial experiments. By comparing the colony–forming capability of nontreated and QDs–treated bacteria, the QD bactericidal activity was evaluated. The QDs show a significant toxic effect on *E. coli* even at the concentration as low as 80 nM (Fig. 4.2). A 92% decrease in the viability of bacteria is observed as the QD concentration reaches 200 nM. The results demonstrate the concentration–dependent bactericidal activity of CdTe QDs. It is quite similar to the reported antibacterial effect of CdSe–core QDs where the number of colony–forming unit (CFU) reduced when the exposure concentration of CdSe QDs increased [29]. The antibacterial concentration range determined in this study is also consistent with that for CdSe QDs reported by Kloepfer *et al* [28].

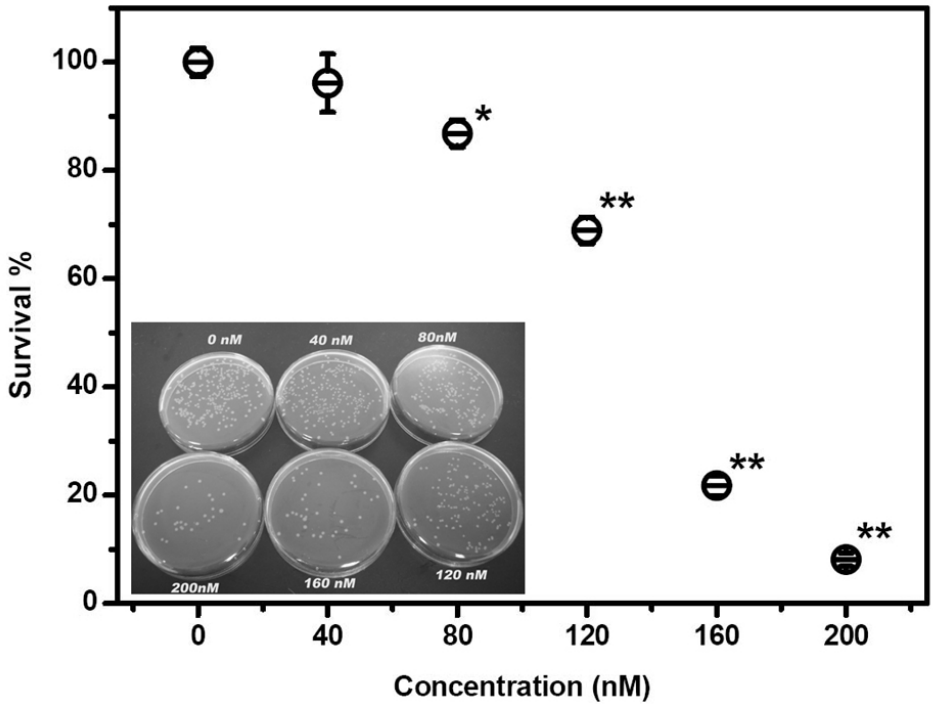

Figure 4.2 Bactericidal activities of CdTe QDs. After being exposed to different concentrations of QDs at 37 °C for 2 hrs, *E. coli* cells were spread onto LB medium agar plates and incubated at 37 °C for 12 hrs (n=3). *: $p < 0.05$, **: $p < 0.01$. Inset shows the formation of bacterial colonies on agar plates.

4.4 Effects of CdTe QDs on *E. coli* Surface Morphology

Bactericidal effects are usually accompanied by a change in bacterial surface morphology. To further verify the antibacterial activity, contact–mode AFM microscopy was conducted to investigate the effects of CdTe QDs on *E. coli* surface morphology. The rod shape, the surface structure, and flagella of individual *E. coli* can be clearly seen in Fig. 4.3. As AFM images show, CdTe QDs treatment significantly changes the morphology of the bacterium. Small dots on the native cell surface are all replaced by big clusters after incubation with CdTe QD (Fig. 4.3B,

4.3F). The small dots may be the pili, which are protein tubes extended out from the outer membrane to facilitate bacterial conjugation and/or the attachment of bacteria on a surface. The formation of large clusters after QD treatment is possibly caused by the oxidative damage to pili proteins. From section curves, it can be observed that holes on the surface of the treated bacterium are much deeper than those on the native *E. coli* cell wall. Oxidative damage to the cell wall of *saccharomyces cerevisiae* have been reported to cause similar membrane damage [141]. The results of colony–forming assay and AFM microscopy indicate that CdTe–core QDs can act as a bactericidal nanomaterial and could have the potential to be formulated as novel antimicrobial materials with superior optical properties.

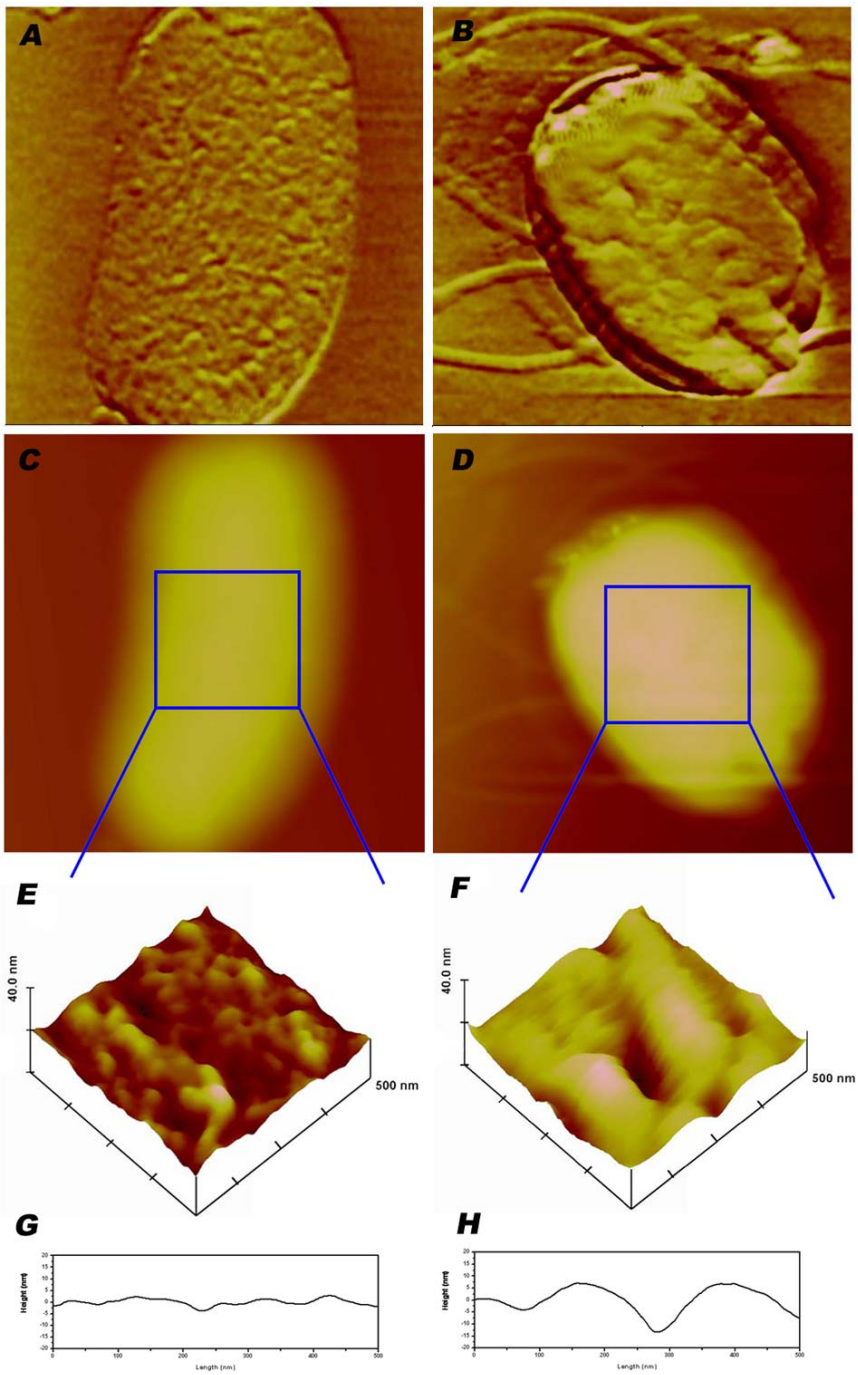

Figure 4.3 CdTe QD–induced surface morphological change of *E. coli*. (A) Friction image of nontreated *E. coli*. (B) Friction image of QD–treated *E. coli*. (C) Height image of nontreated *E. coli*. (D) Height image of QD–treated *E. coli*. The image size in panels A–D is 4 μm. (E) 3–D height magnified image of nontreated *E. coli* surface. (F) 3–D height magnified image of QD–treated *E. coli* surface. The image size of panels E and F is 500 nm. (G) Section curve for image E. (H) Section curve for image F.

4.5 Binding of CdTe QDs on *E.coli*

4.5.1 PL Spectra of QDs–Bacterial Mixture and Bacteria Suspension

It is unknown how CdTe QDs react with *E. coli* to cause the antibacterial effects. Heavy metal ions released from CdTe core, which is always accompanied by the decomposition of QDs, are suspected to be the possible cause. Since QD decomposition leads to the blue shift of the QD emission peak [30, 142], PL spectra of both QDs–bacterial mixture and bacteria suspension were monitored respectively before and after the incubation to verify this assumption. It can be seen from Fig. 4.4A that as the time increases peak intensities of QD emission gradually decline in the QDs–bacteria mixture, while the emission peak wavelength slightly shifts from 602 nm to 605 nm. The red shift caused by the aggregation of QDs on the surface of *E.coli* is observed instead of a blue shift, possibly indicating that CdTe QDs do not decompose during the incubation to release heavy metal ions for the bactericidal activity.

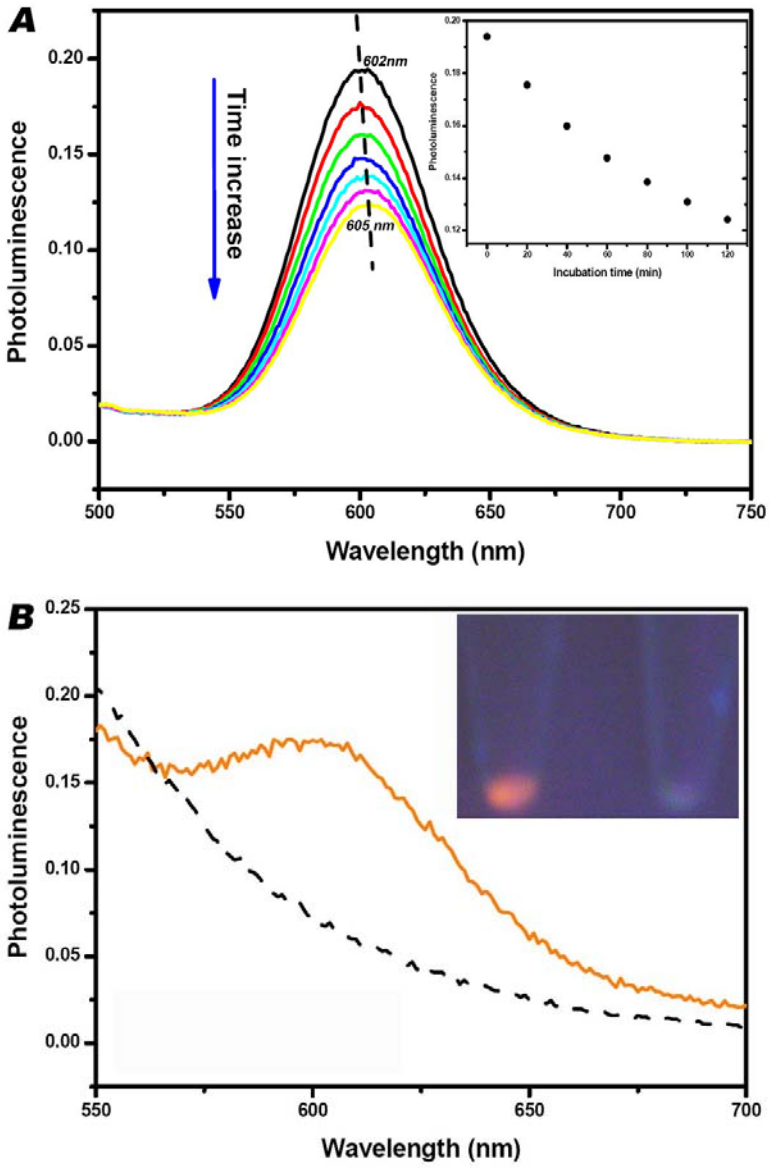

Figure 4.4 PL spectra of QDs–bacteria mixtures and bacteria suspensions. (A) PL spectra of QDs–bacteria mixtures that were measured at an interval of 20 min. (B) PL spectra of bacteria before (dash line) and after (solid line) 2 hr of QDs incubation. The inset shows the fluorescence of QD–treated and nontreated bacterial pellets with the illumination at 330 nm.

As being discussed in chapter 2, QDs can transfer energy to nearby oxygen molecules to induce the formation of singlet molecular oxygen ($1O_2$) and hydroxyl

free radicals (OH•) [63, 143-145]. This study shows that CdTe QDs can increase the level of ROS in bacterial culture medium (Fig. 4.5). ROS could be the key players in biocidal effects of CdTe QDs. However, the life time of $1O_2$ is about 10^{-6} to 10^{-5} seconds [146], and OH• can only react with the surrounding molecules.[147] If ROS play a key role in the bactericidal effect, the QDs must be close enough to bacterial cells. In this study, PL spectrophotometry and confocal microscopy were conducted to investigate whether QDs can bind with *E. coli*. As shown in Fig. 4.4B, no emission peak is observed in bacteria suspension before QDs treatment. After a 2–hr exposure to 200 nM QDs, a significant emission peak corresponding to the QDs appears in the pellet suspension. The inset of Fig. 4.4B also illustrates that the pellet of QDs–treated bacteria under the illumination at 330 nm emits orange fluorescence, whereas the *E. coli* pellet without QDs exposure has no emission. It is known that the diffusion coefficient of oxygen is about 10^{-5} cm^2 s^{-1}, and ROS should have an identical value [148]. The time for ROS diffusion into the bacterium should be around 10^{-7} s, considering the nanoscaled thickness of *E.coli* cell wall and membrane [149]. Therefore, in comparison to the lifetime of ROS (~10^{-5} to 10^{-6} s), QDs induced ROS could have enough time to diffuse into the cells.

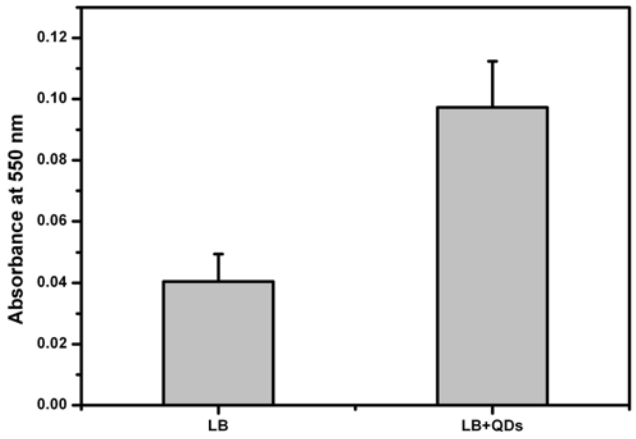

Figure 4.5 Cytochrome c reductions in pure LB medium and LB–QD mixture. The higher absorbence at 550 nm indicates that more cytochrome c has been reduced by ROS.

4.5.2 Confocal Micrographs of Nontreated and QD–Treated *E. coli*

Confocal microscopy further demonstrates the association of QDs and bacteria (Fig. 4.6). Most of the QDs–exposed *E. coli* cells present fluorescence under the irradiation, but no fluorescence can be observed in nontreated bacteria. It has been reported that CdTe QDs could self–assemble on bacterial flagella nanotubes [150] and that QDs without surface conjugations cannot be transported into the bacteria owing to the lack of endocytosis mechanism [151]. In this work, QDs should only be adsorbed on the surface and flagella of *E. coli*.

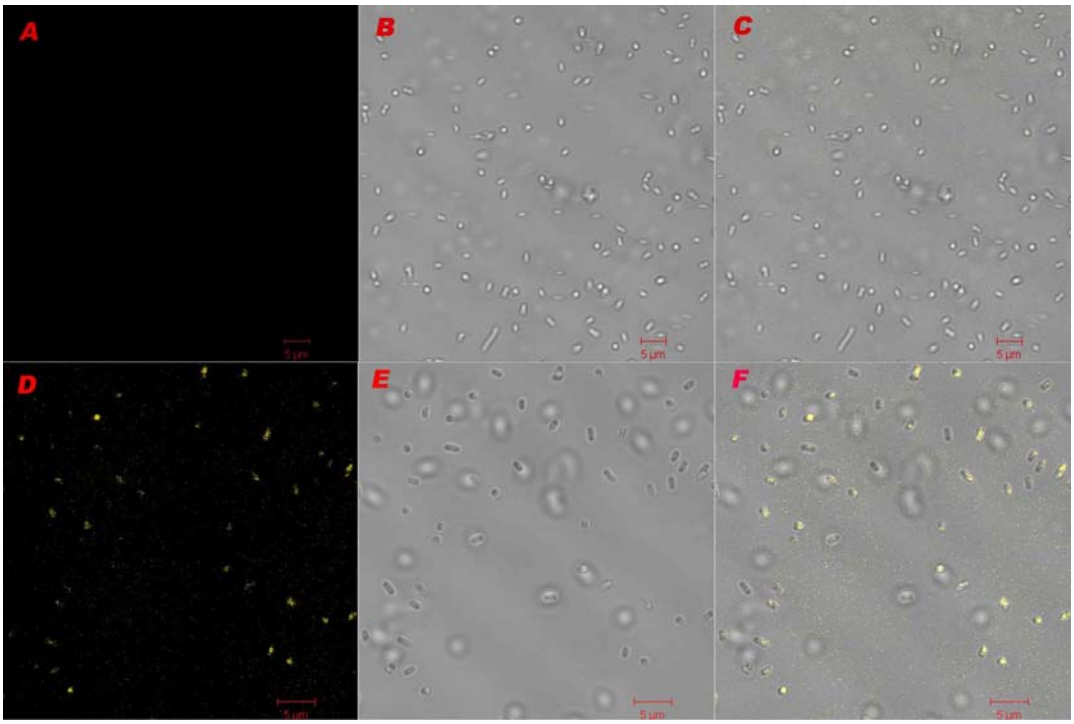

Figure 4.6 Confocal micrographs of nontreated and QD–treated *E. coli*. (A) Fluorescent micrograph of nontreated *E. coli*. (B) Bright field micrograph of nontreated *E. coli*. (C) Merged micrograph of A and B. (D) Fluorescent micrograph of QD–treated *E. coli*. (E) Bright field micrograph of QD–treated *E. coli*. (F) Merged micrograph of D and E.

4.5.3 AFM Imaging

To further verify the location of QDs, AFM was conducted to image the QD–treated bacterial cells. An AFM image of a typical *E.coli* cell was shown in Fig. 4.7, from which the cell body and the flagella can be observed. The height image with larger amplification (Fig. 4.7B) clearly illustrates the attachment of QDs on bacterial flagella. The arrows in the phase image (Fig. 4.7D) indicate the association of QDs to the bacterial cell wall. The AFM images together with the results of PL and confocal micrographs suggest that the MSA–capped CdTe QDs can bind on the

surface of bacteria, providing an immediate contact for the easy diffusion of ROS into the bacterium.

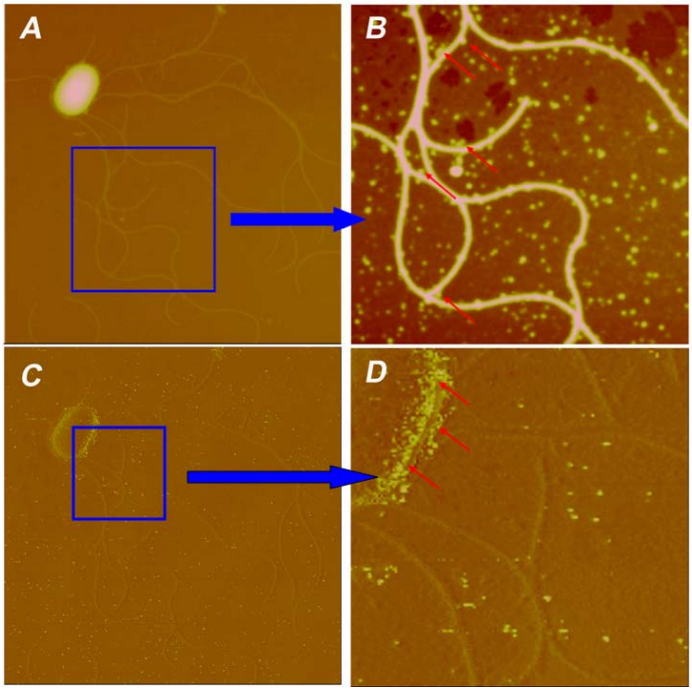

Figure 4.7 AFM micrographs show the binding of QDs with flagella and surface of *E.coli*. (A) Height image of a QDs–treated *E.coli*. Image size: 8.5 μm. Z scale: 500 nm. (B) The flagella–QDs association. Image size: 4μm; Z scale: 20 nm. (C) Phase image of a QDs–treated *E.coli*. Image size: 8.5 μm; Phase scale: 100 degree. (D) Cell wall–QDs association. Image size: 2.5 μm; Phase scale: 100 degree.

4.6 Effects of CdTe QDs on Antioxidative System of *E.coli*

4.6.1 QD–Induced Down–Regulations of ROS–Related Genes in *E. coli*

In biological aerobic organisms, an antioxidative system can protect the cells from the oxidative damage caused by ROS. Thus, although the adsorption of QDs on

surfaces of *E. coli* could possibly make ROS enter into a bacterial cell, their antibacterial effect still depends on the anti–oxidative response of bacteria. The response of the *E. coli* antioxidative system to CdTe QDs should be considered in the mechanism of the QDs bactericidal activity.

In this work, with a semi–quantitative RT–PCR assay, a number of ROS–related genes were chosen as target genes to explore whether QDs could affect the cellular antioxidative system by regulating gene expressions. *nfo*, *sod A* and *zwf* genes encode endonuclease IV, manganese–superoxide dismutase (Mn–SOD) and glucose–6–phosphate dehydrogenase (G6PDH), respectively. 16 S rRNA, a non–coding RNA gene, was used as the internal control in this experiment. Fig. 4.8 shows that expressions of three target genes are significantly down–regulated in 200 nM QD–treated samples. The expression level of *nfo* gene is inhibited up to 50% by the QDs treatment. The down–regulation of *nfo* gene can inhibit the activity of endonuclease IV, and further affect the DNA repair system. About 10% down–regulations of *sod A* and *zwf* are observed. Since Mn–SOD and G6PDH are vital enzymes that can eliminate ROS in *E. coli* cells under the stress environment, down–regulations of *sod A* and *zwf* genes could significantly reduce activities of anti–oxidative enzymes to suppress the cell anti–oxidation capability.

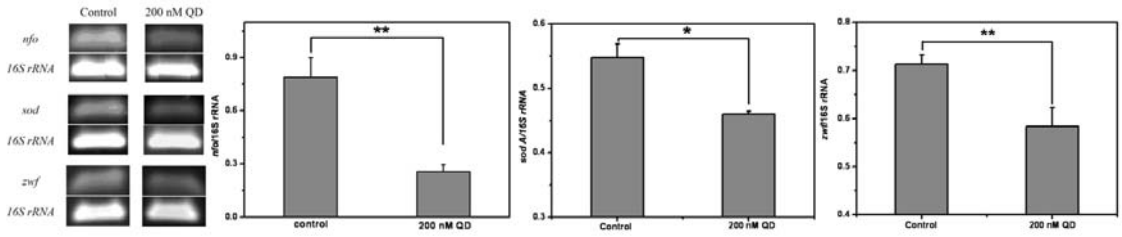

Figure 4.8 QD–induced down–regulations of ROS–related genes in *E. coli*. (n=3). *: $p < 0.05$, **: $p < 0.01$.

4.6.2 QDs–Induced Inhibition on Activities of Antioxidative Enzymes in *E. coli*

To further confirm whether gene expression down–regulation could affect the antioxidative system, activities of antioxidative enzymes in QD–treated *E. coli* were investigated. Two of the most crucial enzymes in the ROS elimination system, SOD and peroxidase, were monitored. As illustrated in Fig. 4.9, QDs could cause the decline of activities of both peroxidase and SOD in a dose–dependent manner. Even if the concentration is only 40 nM, QDs could still inhibit the activity of peroxidase significantly. For the SOD activity, it was negatively affected by an exposure to 120 nM or higher level of QDs ($p < 0.05$, compared to control samples). It can be found that 200 nM QDs could lead to decreases of activities for both peroxidase and SOD. These results are greatly in agreement with the findings in the RT–PCR experiment. Thus, treatment with QDs can not only down–regulate expressions of ROS–related genes, but also reduce activities of antioxidative enzymes in *E. coli*. Apparently, both effects of QDs on *E. coli* revealed from RT–PCR and enzyme activity assays could result in the accumulation of ROS in bacteria.

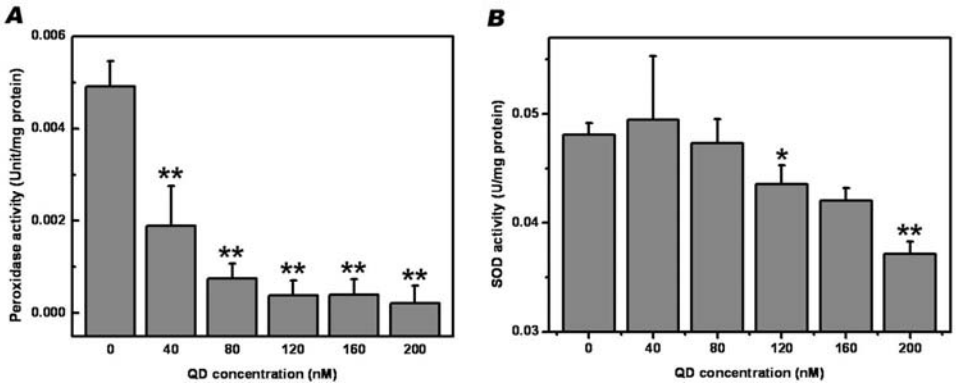

Figure 4.9 Effects of the QDs on activities of antioxidative enzymes in *E. coli*: (A) Peroxidase; (B) SOD. (n=3). *: $p < 0.05$, **: $p < 0.01$.

4.7 QD–Induced Oxidative Damage to Proteins and Lipids in *E. coli*

Once ROS begins to accumulate, the oxidative stress in cells can firstly damage biomolecules such as protein and lipid. Thus, oxidative damage to biomolecules is regarded as indicators of the formation of oxidative stress in cells. It is essential to study whether ROS accumulation in bacteria causes the oxidative stress and damage of biomolecules for fully understanding the bactericidal mechanism. TBARS and protein carbonyl contents, biomarkers of lipoperoxidation, and protein oxidative modifications were used to quantitatively determine levels of oxidative damage to lipids and proteins in *E. coli*, respectively. Results of the lipoperoxidation damage demonstrate a dose–effect relationship between TBARS and QDs concentrations (Fig. 4.10A). At concentrations higher than 120 nM, the level of TBARS in cells increases significantly. Protein carbonyl contents in *E. coli* are also related to QDs exposure levels. It seems that proteins are more sensitive to oxidative stress induced

by QDs than are lipids. 40 nM QDs were enough for the incurrence of significant oxidative damage of the proteins (Fig. 4.10B). This may be one of the causes of lower enzyme activities in the antioxidative system after exposure to QDs. The result here proves the formation of oxidative stress in *E. coli*. Lovrić *et al.* recently reported that N–acetylcysteine, an antioxidant, could effectively prevent the deleterious effects of QDs–induced ROS in cultured cells [152, 153], also suggesting that QDs–induced ROS plays an essential role in the cytotoxicity of QDs. This is greatly consistent with ROS–related bactericidal effects observed in this work.

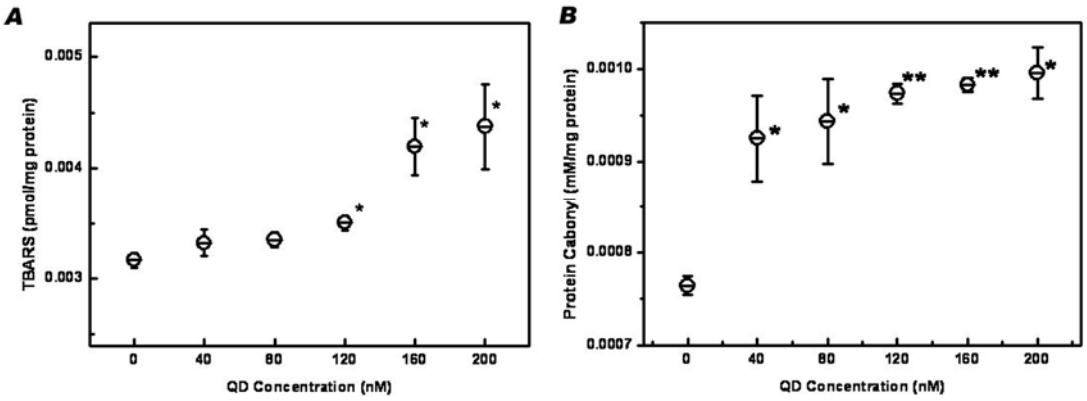

Figure 4.10 QD–induced oxidative damage to proteins and lipids in *E. coli*. (A) Effects of QDs on the TBARS level. (B) Effects of QDs on the protein carbonyl level. (n=3). *: $p < 0.05$, **: $p < 0.01$.

4.8 Mechanism of CdTe QD Bactericidal Activity

On the basis of these discoveries, I propose the mechanism of the bactericidal activity of CdTe QDs that involves both the surface binding and a ROS–dependent

pathway as shown in Fig. 4.11, in which QDs bound on the bacteria surface make the reaction of ROS with cells easily. CdTe QDs can also down–regulate expressions of antioxidative genes, resulting in low level translations of anti–oxidative enzymes to suppress the capability of removing ROS. Obviously, both effects of CdTe QDs can break the oxidant/antioxidant balance and then cause accumulation of ROS in bacteria. The superfluous ROS in bacteria oxidizes proteins and lipids, and triggers the necrosis cellular signals transduction, leading to the biocidal effects. Although TiO_2, SiO_2, ZnO and QDs nanoparticles possess different energy gaps, all of them are reported to produce ROS [58, 63]. They may have an antibacterial mechanism similar to that of CdTe QDs. The proposed mechanism might provide scientific insight to other nanoparticles–induced biocidal activity. However, the effect of different energy gaps possessed by different nanoparticles and QDs with different sizes on the amount of ROS produced and antibacterial mechanism still needs further investigations. Many of the reports on the antibacterial effects and cytotoxicity of nanomaterials focus on the toxins generated by nanomaterials. However, the mechanism of CdTe QD bactericidal activity proposed in this study suggests that, besides nanoparticle induced ROS, the response of anti–oxidative system should also be considered as a key event in antimicrobial activity and cytotoxicity of nanoparticles.

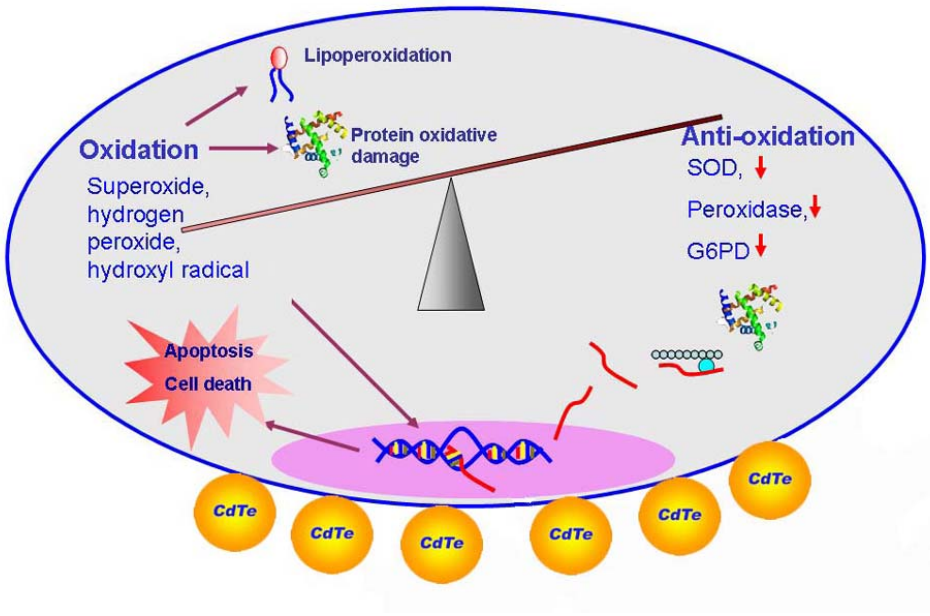

Figure 4.11 Schematic diagram of the mechanism of CdTe QD antimicrobial activity.

4.9 Conclusions

In conclusion, CdTe QDs are demonstrated to be bactericidal nanoparticles for the first time in this project. Those QDs can be bound on the bacterial surface and negatively affect the function of cellular antioxidative systems including down–regulations of antioxidative genes and decreases of antioxidative enzyme activities. Based on the results, the mechanism of the bactericidal activity of MSA–capped CdTe QDs is proposed, in which the formation of the QDs–bacteria complex and a QDs related ROS–mediated pathway are involved.

Chapter 5 QD–Induced Bacterial Growth Inhibition and Its Photophysical Mechanism[b]

5.1 Introduction

QD–induced ROS might be generated via two types of photodynamic reactions [143, 144]: an electron or hydrogen–transfer between excited triplet state QDs and other molecules, which generates free radicals, and an electron spin exchange between excited triplet state QDs and triplet oxygen, which produces singlet oxygen. Apparently, photophysical behaviors of QDs including photon absorbance, QD excitation from ground state to excited state, and QD PL emission must be closely related to their antimicrobial activity. Thus, fully understanding of the photophysical process behind QD-bacteria interactions can not only provide fundamental insight of QD nanotoxicology, but also render potentials for QD antimicrobial applications. In above chapter, the bactericidal effects of CdTe QDs have been investigated. However, to date, QD–induced bacterial growth inhibition and its photophysical mechanism have not been studied with delicate experiments, of which the relationship among QD PL intensity, ROS level and resulted biological responses needs to be thoroughly explored.

In this chapter, QD effects on bacterial growth as well as the alteration of PL intensity and ROS level in this process was investigated. The photophysical

[b] Reproduced in part with permission from [Z. S. Lu, C. M. Li, H. F. Bao, *et al.*, *J. Nanosci. Nanotech*, 9 (2009), 3252–3255.] Copyright [2009] with permission from American Scientific Publishers

mechanism behind QD-caused inhibition of bacterial growth was also discussed.

5.2 Preparation and Measurement

5.2.1 Bacterial Growth Curve

E.coli cells at log growth phase were inoculated into LB media containing 0, 10, 20, 30 and 40 nM of QDs respectively, followed by incubation at 37 ^{o}C with shaking for 22 hrs. Absorbance at 600 nm was recorded every 2 or 4 hrs to monitor the growing profiles of *E.coli*.

5.2.2 Cytochrome c Reduction Assay

Cytochrome c reduction assay is a well established method for the detection of ROS level in biological samples. When cytochrome c is reduced by receiving an electron from ROS, its absorbance at 550 nm increases while remaining absorbance at 540 and 560 nm unaltered [154]. Therefore, the intensity of cytochrome c reduction peak at 550 nm is normally used to represent the ROS level in the sample. Briefly, after culturing for desired time, 99 μl of LB medium was mixed with 1μl of 5 mg/mL cytochrome c solution. The UV–vis spectra of the samples were recorded after 5-min incubation at room temperature under dark.

5.3 QD-Caused Bacterial Growth Inhibition

The bacterial growth curve [54] was measured to monitor the bacterial population over a period as shown in Fig. 5.1, in which the optical density at 600 nm (OD600) was employed to represent cell density in the LB medium. After 18–hrs incubation, the growth of *E.coli* reaches to the stationary phase, at which the cell density decreases with an increase of the QD concentration in the LB medium. The results indicate that the bacterial growth is effectively inhibited by CdTe QDs in a concentration–dependent manner. In addition, the lag phase of QD-treated samples is prolonged to 10 hrs, which is much longer than that of negative control group. AFM was conducted to further explore the morphology of *E.coli* in this prolonged lag phase. The 40 nM QD-treated bacterium evolves an elongated shape after 8–hr incubation in comparison with the bacterial cells in the control sample (Inset I of Fig. 5.1). Since the bacterial growth usually includes the alternate cell elongation and division, the elongated bacterial shape here may imply an abnormal division during the growth of the QD treated *E.coli*. The significant down-regulation of the expression of cell division gene *Env C* (Inset II of Fig. 5.1) in the treated bacteria was demonstrated using semi–quantitative RT–PCR assay, verifying the division blocking effects of QDs on *E.coli* cells. The proliferation of bacteria involves the cell elongation and the cell division. Although the divison is inhibited, the bacteria can still take nutrition from the culture medium to grow along the length direction resulting in elongated shapes.

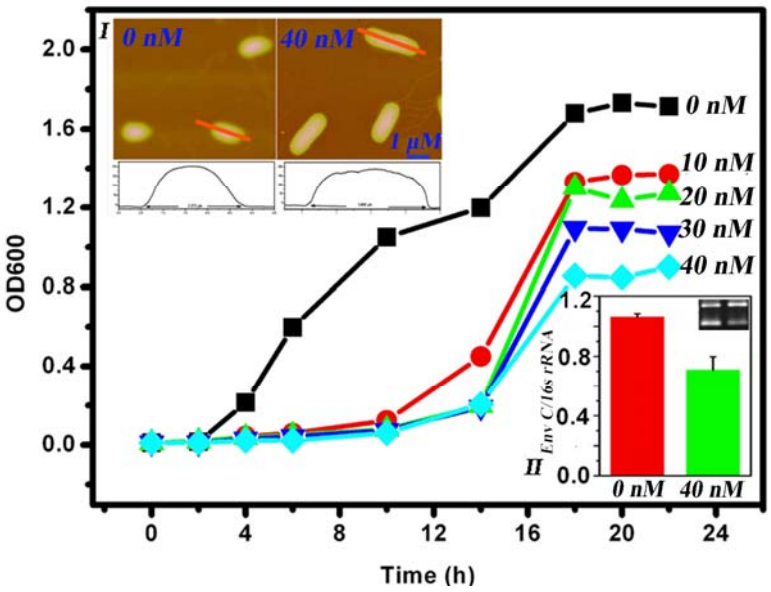

Figure 5.1 Effects of CdTe QDs on *E.coli* growth. Inset I shows AFM micrographs of *E.coli* in present of 0 nM and 40 nM QDs after 8-hr incubation. The section curves indicate that QD–treated bacteria are much longer than native ones. Inset II shows *Env C* gene expression level of *E.coli* in present of 0 nM and 40 nM of QDs after 8-hr incubation.

5.4 Optical Properties of QDs during Incubation

Since QDs have unique optical properties, their photophysical mechanism for cell growth inhibition could be accompanied by the alterations of their absorbance and PL emission. Thus, UV–vis and PL spectrometries were carried out to monitor QD photophysical behaviors in the 10–hr growth inhibition process.

The QD emission maximum reduces continuously with an increase of incubation time (Fig. 5.2A). However, no significant change on QD absorbance spectra is observed in the same time span (Fig. 5.2B), indicating that QDs keep intact while inhibiting the cell growth and that the PL decrease is not caused by QD

decomposition. The results exclude the possible influences of heavy metal ions released from the decomposed QDs [30, 155].

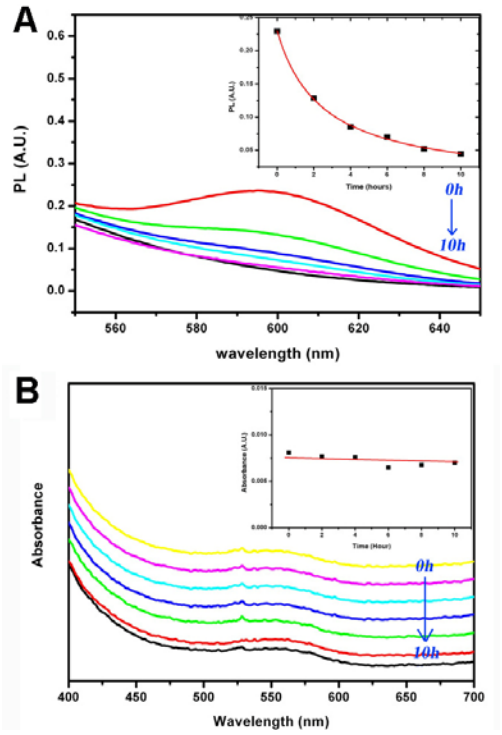

Figure 5.2 (A) PL spectra of LB medium containing 40 nM QDs after 0, 2, 4, 6, 8, and 10 hrs, respectively. Inset shows plots of PL peak intensity against time. (B) UV–vis spectra of LB medium containing 40 nM QDs after 0, 2, 4, 6, 8, and 10 hrs incubation, respectively. Inset shows plots of absorbance peak intensity against time.

5.5 Time–Dependent Alteration of QD–Generated ROS Level

ROS-caused damage of protein and DNA is considered as a common mechanism of the cellular death induced by bactericidal antibiotics [156, 157]. As being investigated in the above chapter, ROS is an essential factor in QD bactericidal

activity. To further explore the possible role of ROS in the bacterial growth inhibition, cytochrome c reduction assay was conducted as reported [158] to measure the ROS level in a LB medium containing 40 nM QDs. Upon the addition of QDs, the reduction peak is significantly enhanced (Fig. 5.3), indicating the increment of the ROS level in the medium. However, as the incubation time increases to 8 hrs, the ROS level continuously decreases. After 8 hrs, the ROS level almost returns to the basic level observed in a pure LB medium. The finding of ROS change is greatly correlated with the results in cell growth inhibition assay. It is reported that QD-induced ROS may lead to damage to biomolecules including protein, DNA and lipid [145]. At the beginning, the high level of QD–induced ROS in the culture medium may damage protein, lipid and DNA in bacteria, further resulting in the down–regulation of cell division gene and the bacterial growth inhibition. When the ROS level drops to the basic level after 8 hrs, the recovery of growth and rapid division of elongated cells could lead to a sharp increase of the bacterial density. Therefore, ROS should be the key mediator in QD–induced bacterial growth inhibition. This discovery is in agreement with ROS-involved bacterial growth inhibition caused by other photosensitive nanoparticles such as ZnO, SiO_2 and TiO_2 [58, 159].

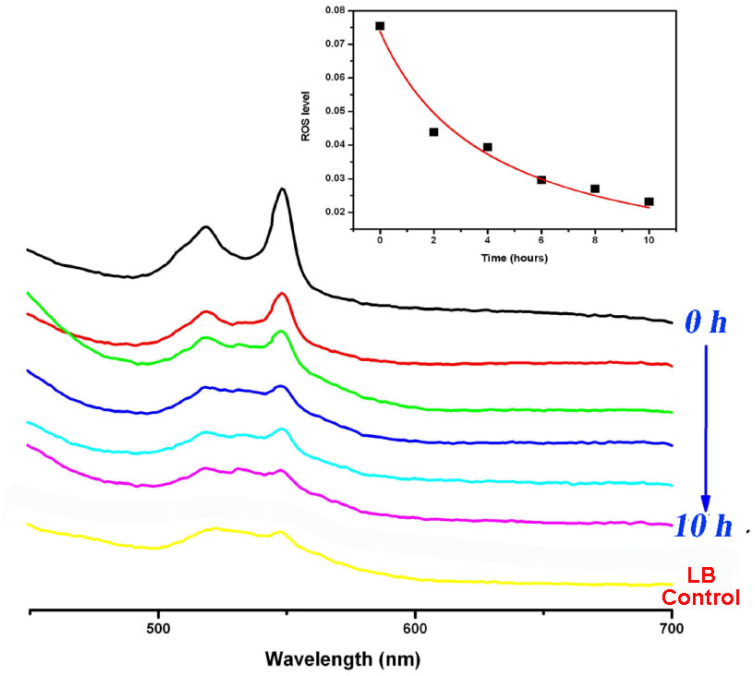

Figure 5.3 Cytochrome c reduction assay in LB medium containing 40 nM QDs after 0, 2, 4, 6, 8, and 10 hrs incubation at 37 ^{o}C. Inset shows plots of ROS level against time.

5.6 Time–Dependent ROS Generation and PL Emission

Another interesting finding is the similar time-dpendent descending trends of both PL intensity and ROS level (Insets of Fig. 5.2A and 5.3). It is likely that there is a relationship between PL intensity and ROS amount, of which fully understanding could clarify the photophysical mechanism for QDs–induced cell growth inhibition. Theoretically, absorbance of photon excites QDs from the ground electronic singlet–state S_0 to the exited singlet–state S_1, which can relax to its ground state by emitting fluorescence. The short–lived S_1 state may also convert to the excited triplet state T_1 through intersystem crossing [143, 144]. When T_1-state QDs reacts with

triplet oxygen or other molecules, the produced free radicals may inhibit the bacterial growth. Therefore, both the PL intensity and ROS generation relies on the high energy state S_1. Recently, the ligand coverage on QD surface is reported to significantly quench its fluorescence [160], so that the PL and ROS level may also relates to the QD surface properties. The hydrodynamic diameter of LB-incubated QDs is much larger than that of pristine QDs (Figure 5.4A), suggesting the adsorption of medium-sourced polypeptides or amino acids on QDs surfaces. Once polypeptides or amino acids are adsorbed on the QD surface, part of energy could transfer from S_1 state to the adsorbed quenchers, and then the reduction of PL intensity and ROS generation occurs, leading to the weak cell growth inhibition effects.

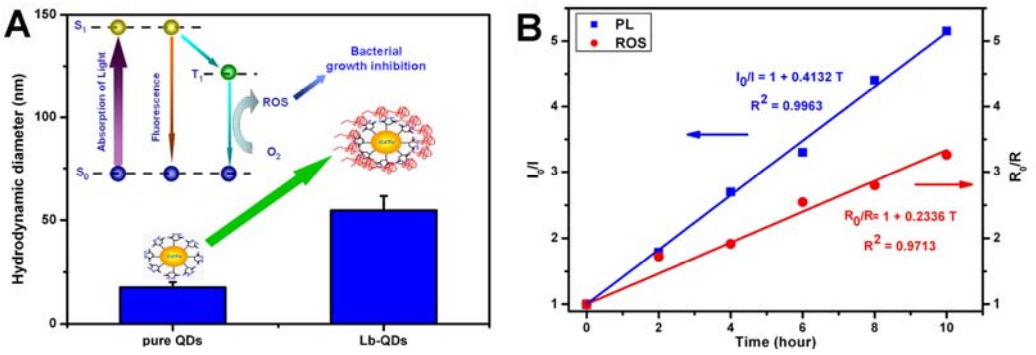

Figure 5.4 (A) Hydrodynamic sizes of pristine QDs and LB–incubated QDs. Inset shows the proposed photophysical mechanism for the bacterial growth inhibition effects of QDs. (B) The relationship between incubation time and resulting intensity of fluorescence or ROS. I_0/I (solid square) and R_0/R (solid circle) are plotted against incubation time, respectively.

To further quantitatively investigate the PL quenching and ROS level reduction,

Stern–Volmer equation was applied to simulate the data. Since various water–soluble polypeptides and amino acids, which are required for bacterial growth, are contained in LB culture medium, the adsorption of quencher might be influenced by the complicated microenvironment around QDs or competitive binding of other elements. The adsorption is likely very slow and the density of quenchers on QDs surface might be proportional to incubation time. The adsorption rate is assumed to be constant in 10 hrs. The fluorescence static quenching is simulated with the modified Stern–Volmer equation [160]:

$$I_0 / I = 1 + KT ,$$

Where T is the incubation time representing the quencher density on the QDs surface, I_0 and I are the PL intensity at 0 and T hrs, respectively, and K represents the quenching constant. The fluorescence intensity ratios, I_0/I are plotted against incubation time in Fig. 5.4B to illustrate the quenching trend. The PL quenching data fit very well to the equation over the full time range with K = 0.4132 hr^{-1} (Fig 5.4B). On the basis of the proposed mechanism, this equation can be used to model the ROS quenching process after changing I_0 and I to R_0 and R, which stand for the ROS level at 0 and T hrs, respectively. The fitting data are shown in Fig. 5.4B with the ROS quenching constant as 0.2336 hr^{-1}. The modeling results demonstrate that QD PL intensity decreases more rapidly than QD–generated ROS. It is possibly caused by supplement of the ROS generated from the photo–catalytic reaction on the QDs surface [161]. The analysis suggests that QDs fluorescence intensity could be

utilized to predict the ROS level and its final effects on the biological system. This discovery should be valuable for the evaluation of toxic, antimicrobial and cancer photodynamic therapy effects of QDs.

5.7 Conclusions

In conclusion, QD–generated ROS can inhibit the growth of bacteria by blocking cell division. Photophysical mechanism involving polypeptides or amino acids adsorption on QDs surface, fluorescence and ROS quenching is proposed on the basis of hydrodynamic size measurement, ROS assay, PL and UV–visible spectrometry. The mechanism provides fundamental insights to understand QD–induced bacterial growth inhibition and the use of QDs in antimicrobial applications. Although it has been reported that QDs could induce cytotoxicity to animal cells, as summarized by Hardman,[31] the toxic concentration level is in the range of several micromoles per liter, which is much higher than the antimicrobial concentration observed in this project. Based on the results of Chapter 4 and 5, it can be concluded that QDs have the potential to be formulated as novel antimicrobial materials. However, the use of QDs as antimicrobial materials should be cautious and limited until their long–term toxic effects are completely clear and biocompatibility is significantly improved.

Chapter 6 Biocompatible Fluorescence–enhanced ZrO_2–CdTe QD Nanocomposite for *in vitro* Cell Imaging[c]

6.1 Introduction

Heavy metal–free QDs, such as ZnS [162], Si [67] and ZnO QDs [163], have recently been developed to reduce the nanotoxicity of QDs and thereby extend their use in biological applications. However, Cd–free QDs do not have the broad size–tunable emission range offered by conventional CdTe and CdSe QDs, and offer only a relatively low level of quantum efficiency. Alternatively, various materials including chitosan [32, 33], poly(lactide–co–glycolide) [34], polyisoprene [35], amphiphilic polymers [36] and silica [37-39, 82] have been used to coat QDs to prevent the core metals from leaching out into an oxidative environment. However, some non–biocompatible polymers may introduce new toxic sources while significantly quenching fluorescence. Therefore, it is a great challenge to develop a coating material that not only improves biocompatibility but also retains a high level of QD fluorescent intensity.

Zirconia (ZrO_2), a ceramic material possessing a high level of chemical stability and mechanical strength and a low extinction coefficient [164, 165], has been extensively studied as a bio–inert material in biomedical applications such as abutment and dental implants [166]. Recently, ZrO_2 has been immobilized with

[c] Reproduced in part with permission from [Z. S. Lu, Z. H. Zhu, X. T. Zheng, et al., *Nanotechnology*, 22 (2011), 155604.] Copyright [2011] with permission from IOP publishing.

biomolecules for use in biosensing applications [167, 168]. ZrO_2–coated magnetic nanoparticles have been applied as affinity probes to selectively concentrate phosphopeptides from tryptic digestion of proteins [169].

To date, ZrO_2 has not been used to coat QDs for use in biological applications. In this chapter, a reverse microemulsion approach was used to fabricate a monodispersed ZrO_2–CdTe QD nanocomposite before the physical and optical properties of the synthesized nanoparticles were examined using FESEM, TEM, energy dispersive X–ray spectroscopy (EDX), UV–vis, and PL spectrometry, respectively. The biocompatibility of the ZrO_2–CdTe QD nanocomposite was evaluated using (3–(4,5–Dimethylthiazol–2–yl)–2,5–diphenyltetrazolium bromide (MTT) assay. The nanocomposite functionalized with folic acid has been employed to label *HeLa* cell for *in vitro* cancer cell imaging application.

6.2 Material Synthesis and Cell Imaging Testing

6.2.1 Synthesis of ZrO_2–QD Nanocomposites

To perform the typical reverse microemulsion synthesis (Scheme 1), 7.5 mL of cyclohexane, 1.77 mL of Triton X–100, 1.8 mL of n–hexanol, and 500 μL of QD (100 μM) water solution were mixed together and stirred for 30 min (800 rpm) to form a microemulsion. Zirconium propoxide solution was then dispersed into the mixture to initiate a hydrolysis reaction. After stirring for 280 min, 20 mL of acetone

was added into the microemulsion system to terminate the coating reaction. ZrO_2–QD nanocomposites were then collected by centrifugation at 8000g for 10 min, and the pellet then washed sequentially with acetone, ethanol, and water.

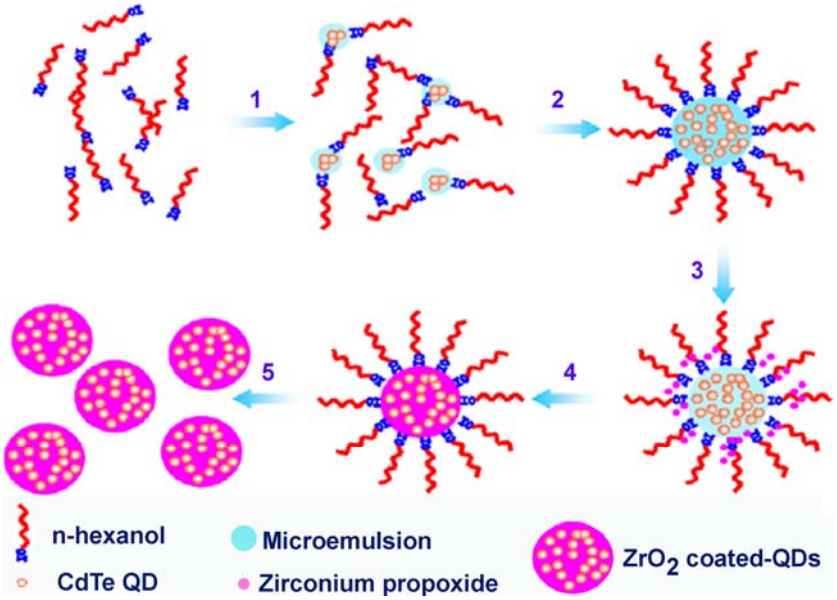

Figure 6.1 Schematic strategy for the synthesis of ZrO_2–QD nanocomposites using the reverse microemulsion approach. 1) Addition of QDs aqueous solution; 2) Formation of emulsion; 3) Addition of zirconium propoxide; 4) Hydrolysis of zirconium propoxide; 5) Collection of ZrO_2-coated QDs.

6.2.2 *HeLa* Cell Imaging

After washing with ethanol three times, the freshly synthesized nanocomposites were treated with 5% (v/v) glycidyl methacrylate (GMA) in ethanol to introduce epoxy groups onto the nanoparticle surfaces, in accordance with the methodology followed in previous studies [170, 171]. Folic acid was dissolved into ethanol and

mixed with epoxy group functionalized ZrO_2–QD nanoparticles under stirring for 2 hrs. After washing three times with distilled water, the folic acid–immobilized nanocomposites were collected by centrifugation at 8000 g for 10 min.

The cells were treated with folic acid–immobilized nanocomposites for 12 hrs. Before testing, the cells were washed three times with PBS at pH 7.4. Fluorescent images were acquired with a Zeiss LSM 510 Meta confocal microscope.

6.3 Physicochemical Properties of ZrO_2–QD Nanocomposites

The water–soluble MSA QDs synthesized by a hydrothermal method were found to be very uniform, having diameters of ~3 nm (Fig. 6.2A and B) and, as shown in the HRTEM micrograph in the inset of Fig. 6.2B, an excellent crystalline structure. The UV–vis and PL spectra of the MSA–QDs (data not shown) show a high level of absorbance and desirable emission properties, consistent with the results reported in previous chapters.

As hydrolysis of zirconium propoxide is relatively rapid, the precursor was diluted with an anhydrous ethanol to precisely control the reaction rate to obtain uniformly coated spherical ZrO_2–QD composites with an average size of 30 nm in diameter (Fig. 6.2C). The thickness of the ZrO_2 coating layer could be easily adjusted by controlling the reaction time. The lattice planes in the HRTEM image indicated that a number of QDs had been encapsulated by ZrO_2 (Fig. 6.2D), and that the sizes and lattice planes of the encapsulated QDs were the same as those of the

original CdTe QDs. The EDX spectrum further confirmed that the components of the synthesized nanocomposites were CdTe QDs and ZrO_2 (Fig. 6.2E). The overall results indicate that ZrO_2–QD nanocomposites had been successfully fabricated using the reverse microemulsion approach.

A primary challenge in the fabrication of the QD nanocomposites is limiting their sizes to those suitable for biomedical applications. To date, the smallest silica–coated QDs, the most widely used in QD nanocomposites in biological systems, are produced at a size of ~30 nm in diameter. As prepared ZrO_2–QD nanoparticles have been found to have sizes comparable to those of silica–QD nanocomposites [38, 39], ZrO_2–QD nanocomposites could be promising substitutes for silica–capped QDs in biological applications.

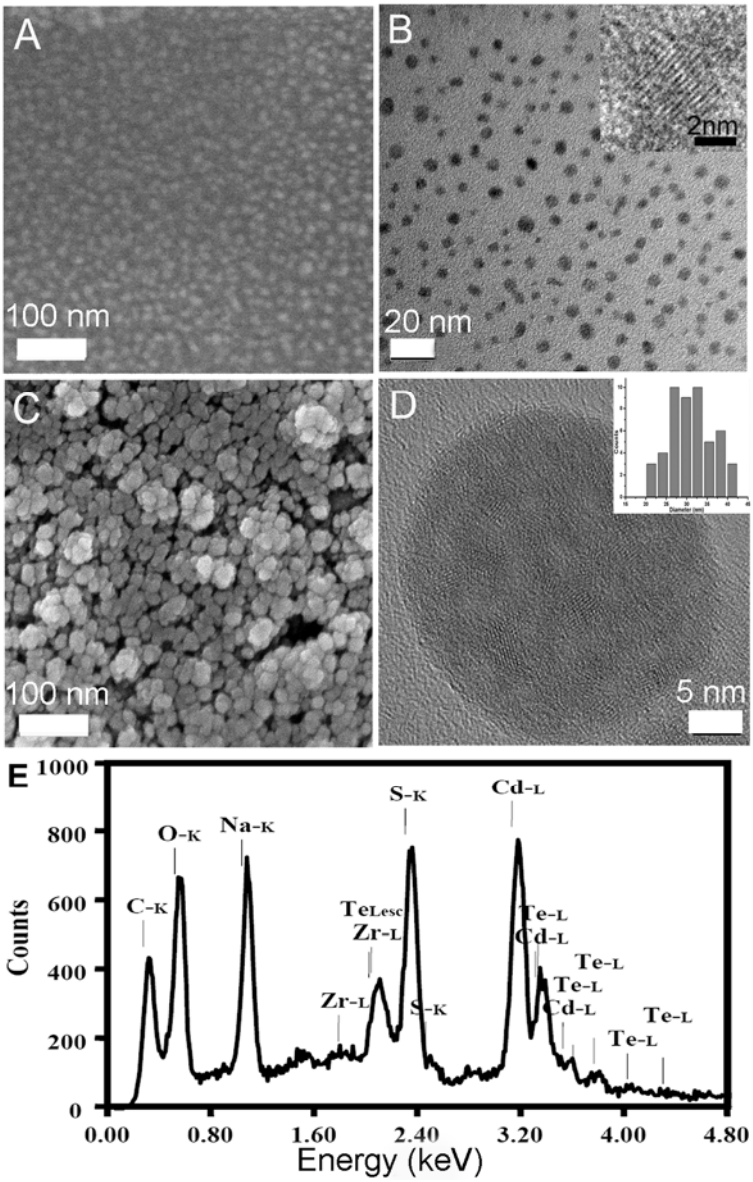

Figure 6.2 (A) SEM and (B) TEM images of CdTe QDs; (C) SEM and (D) TEM images of ZrO_2–CdTe QD composites; (E) EDX spectrum of ZrO_2–CdTe QD composites.

6.4 Optical Properties of ZrO_2–CdTe QD Composites

In addition to their size, the optical properties of the synthesized composites are very critical in bioimaging applications. One critical property that has been observed is QD fluorescence quenching in the coating process [34, 172], and other synthesis conditions may have a significant impact on optical properties. When the effects of

the hydrolysis reaction time and the precursor (zirconium propoxide) concentration on composite were investigated, the PL intensity of the ZrO_2–coated QDs was found to increase with increasing reaction time until reaching a peak intensity plateau at 280 min, as being shown in Fig. 6.3A. The enhancement of the fluorescence may be due to the altered surface chemistry of the CdTe QDs. Pristine QDs may have surface defects to reduce the QY by surface non-radiative electron energy transitions. The ZrO_2 shell could passivate QD surface to increase quantum yield. Thus, with increasing of the reaction time more ZrO_2 is coated on the QD surface, further eliminating its surface defects to enhance the fluorescence. In addition, the high transmittance of ZrO_2 shell in the wavelength range of 350 to 1100 nm also warrants efficient excitation and emission of the encapsulated QDs for the enhanced fluorescence. The fluorescence intensity does not increase further upon completion of the hydrolysis reaction, which also supports the proposed mechanism above. Moreover, the fact that a maximum peak plateau was achieved after a reaction time of 280 min may indicate that all QD surface defects had been repaired within this reaction time, and that it is thus the optimal reaction time.

Interestingly, along with the fluorescence enhancement, a red shift from 555 nm to 562 nm was observed, a phenomenon that may be attributed to the encapsulation of a number of CdTe QDs in one composite, as is shown in the HRTEM micrograph. Exciton energy from the larger bandgap QD is transferred to its neighbored QDs with smaller bandgap, which causes redshift of the emission peak. The QD

concentration in the reaction system could be controlled to prevent the QD aggregation in the composites for avoiding the redshift. A well–defined absorption peak with a peak wavelength at 500 nm was observed in the UV–vis spectra (data not shown) for both pristine and ZrO_2–encapsulated QDs, indicating that neither growth nor decomposition of pristine QDs occurs during synthesis [173].

Fig. 6.3B exhibits the effect of precursor concentration on the fluorescence of nanocomposites. The peak wavelength red shifts as the concentration of precursor increases from 0 to 30 mg/mL. With an increase of precursor concentration to 15 mg/mL, the PL peak intensity continuously increases before decreasing, indicating that 15 mg/mL is the optimal precursor concentration in enabling a proper reaction rate to form a compact ZrO_2 shell that can passivate the QD surface effectively.

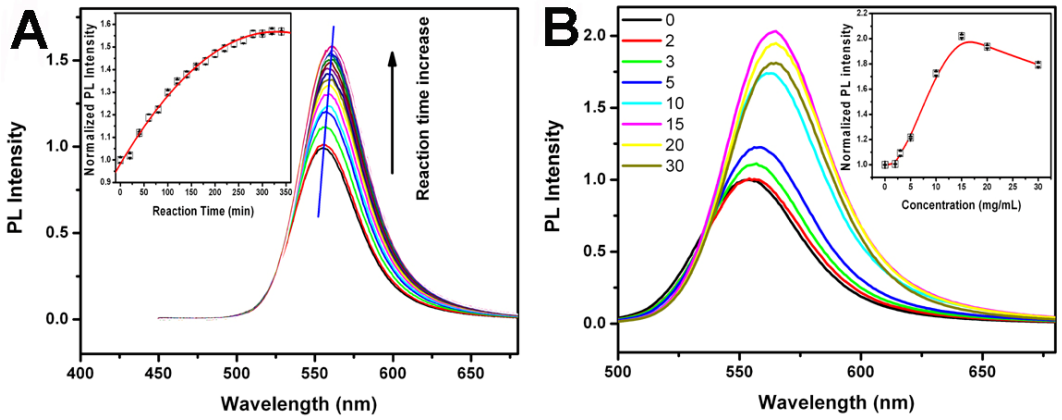

Figure 6.3 Impact of the reaction time (A) and the precursor concentration (B) on the fluorescence of synthesized ZrO_2–QD nanocomposites.

6.5 Photostability of ZrO_2–QD Nanocomposites

Due to their high level of fluorescence stability under irradiation, QDs are promising substitutes for conventional organic dyes in bioimaging applications. The stability of the synthesized ZrO_2–QDs nanocapsules under UV irradiation was studied by using a 350 nm light source to excite both pristine and ZrO_2–encapsulated CdTe QDs for stability comparison. The plot of normalized PL peak intensity versus irradiation time in Fig. 6.4 shows that while the pristine QDs exhibited a stable level of fluorescence emission, the PL intensity of the ZrO_2–QD nanocomposites continuously increased with an increase in the irradiation time until reaching a plateau value at 1320 s. This interesting phenomenon, which has been also observed in silica–coated QDs [37, 38, 174], may be due to surface passivation or photoactivated rearrangement of the surface.

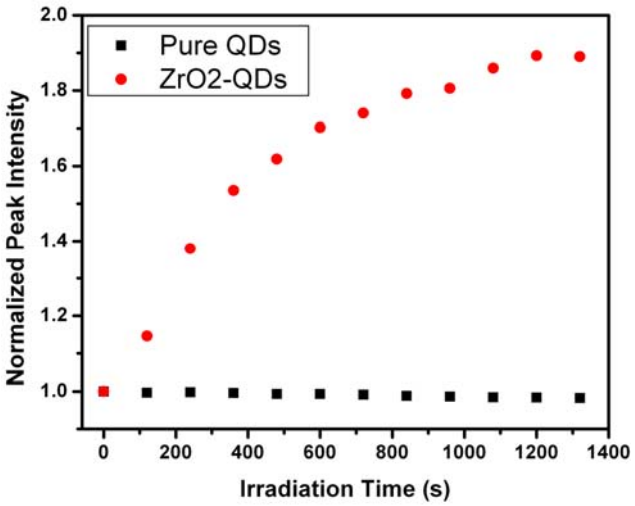

Figure 6.4 Stability of fluorescence of pristine QDs and ZrO_2–QD nanocomposites under UV irradiation (350 nm). The PLs were normalized by the PL intensity of QDs and ZrO_2–QD nanocomposites at 0 s, respectively.

6.6 Biocompatibility of ZrO_2–QD Nanocomposites

To reduce the reported nanotoxicity of CdTe QDs [31, 175], QDs are often coated with various materials. In this study**,** both pristine and ZrO_2–coated QDs were found to be cytotoxic to *HeLa* cells, as shown in Fig. 6.5. However, the level of cell viability of ZrO_2–QD nanocomposites was found to be significantly higher than that of pristine QDs at the same concentration. Most notably, the ZrO_2–QD nanocomposite–treated cells were observed to undergo no significant change in viability at a concentration of 100 nM, and to maintain 75% of cell viability at a concentration as high as 800 nM. The results indicate that the ZrO_2 shell reduces the toxic effects of CdTe QDs on *HeLa* cells and that 100 nM ZrO_2–QD nanocomposites can be safely utilized for *HeLa* cell imaging.

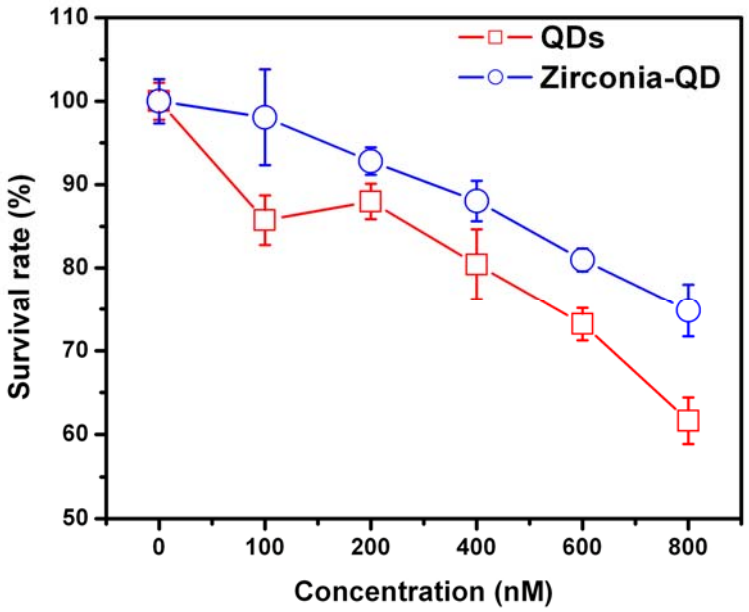

Figure 6.5. Cytotoxicity of CdTe QDs and ZrO_2–QD nanocomposites to *HeLa* cells.

6.7 Use of ZrO_2–QD Nanocomposites for *HeLa* Cell Imaging

After functionalization with folic acid, the ZrO_2–QD nanocomposites were used to label the *HeLa* cells for cell imaging. The labeled cells exhibited fluorescence under irradiation, but no fluorescence was observed in the control images (Fig. 6.6). As shown in Fig. 6.6, green fluorescence can be observed in the *HeLa* cells and almost all the cells in the image are labeled, indicating that the cells can be effectively labeled by the folate-functionalized nanocomposites. The well-spread shapes of the cells also suggest good biocompatibility of the nanocomposites. The folate receptor has been reported to be located on the membrane of tumor cells, including tumorous *HeLa* cells [176]. The nanoparticles should be attached to the membrane of the cells. The images suggest great potentials to use the ZrO_2–QD nanocomposite for *in vitro* cell imaging as an efficient alternative or complimentary tool to conventional organic dyes.

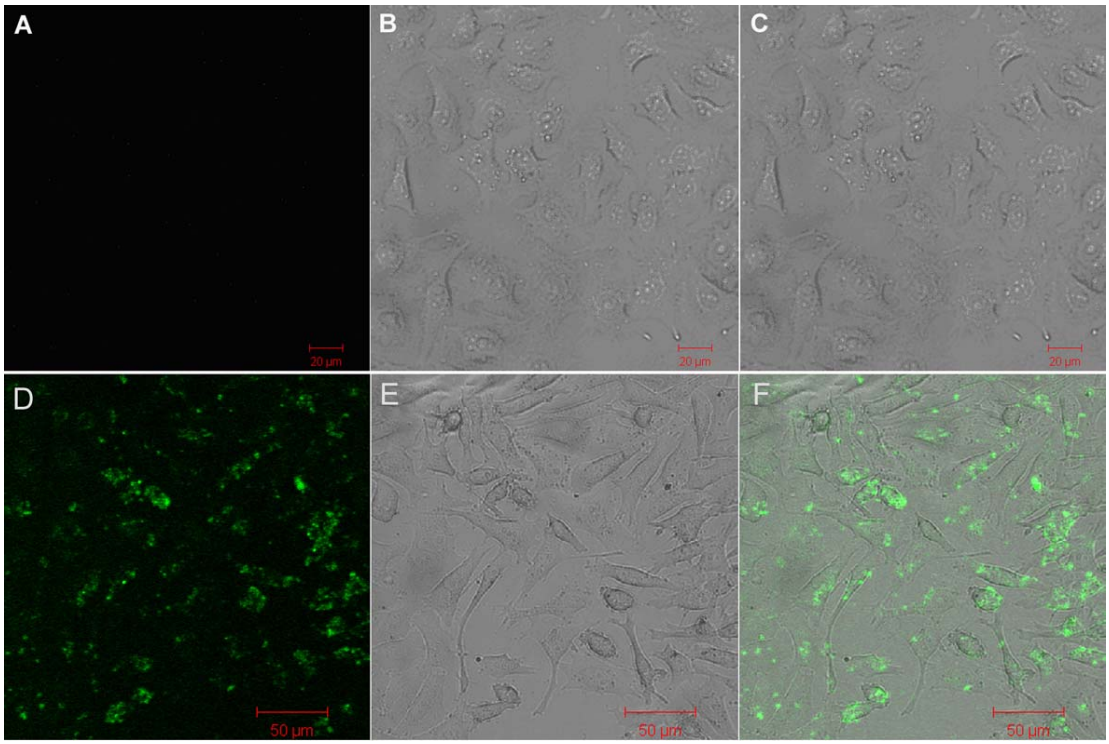

Figure 6.6 Application of ZrO_2–QD nanocomposites to *HeLa* cell imaging.

6.8 Conclusions

For the first time, this study fabricated biocompatible ZrO_2–QD nanocomposites that exhibited enhance fluorescence emission using the reverse microemulsion approach. Subsequent measurement and analysis of the synthesized nanocomposites demonstrated that they were ~30 nm in diameter, a size suitable for biological applications, and exhibited continuously increased emission under light illumination until reaching a plateau value almost two times that of pristine QDs. MTT assay analysis further indicated that their level of biocompatibility is superior to that of pristine CdTe QDs. After functionalization with folic acid, the nanocomposites

demonstrated their utility in successful cell imaging by effectively labeling *HeLa* cells. Based on these results, it can be concluded that ZrO_2–QD nanocomposites are promising biocompatible nanomaterials that, due to their higher levels of fluorescence and biocompatibility, may be able to replace or complement QDs in bioimaging applications. The fabrication approach used in this study may also be appropriate for the fabrication of other small ZrO_2–coated nanoparticles.

Chapter 7 Extracellular Microbial Synthesis of Biocompatible Protein–coated CdTe QDs for Cell Imaging[d]

7.1 Introduction

The organometallic method [41, 177, 178] and water–based synthesis [137, 179-181] with thiols as capping ligands are the two successful routes for the synthesis of highly fluorescent CdTe QDs. However, the current methods involve highly toxic chemicals, such as trioctylphosphane or trioctylphosphane oxide, and require high temperatures. There is a great need to develop a cost–effective, environment–friendly and reproducible method to synthesize CdTe QDs with controlled structures and properties.

Recently, biological organisms have been employed to synthesize QDs with precisely controlled sizes, shapes, and functionalities [182]. The preparation of ZnS nanoparticles by sulfate–reducing bacteria under anaerobic conditions and by *Rhodobacter sphaeroides* has been reported [183]. Many microorganisms, such as *Fusarium oxysporum* [184], *Schizosaccharomyces pombe* [185], *Rhodopseudomonas palustris* [186] and *E.coli* [151], have been used to synthesize CdS QDs. PbS QDs have been prepared using *Torulopsis spp.* [187]. These approaches are carried out at ambient temperature and are considered as environment–friendly methods. However, the controllable synthesis of QDs with tunable fluorescence emission is still a

[d] Reproduced in part with permission from [H. F. Bao[#], Z. S. Lu[#], X. Q. Cui, *et al.*, *Acta Biomater.*, 6 (2010), 3534–3541. # Contribution equally to this work] Copyright [2010] with permission from Elsevier.

challenge for the microbial synthesis approach. Although a yeast–based biosynthesis of CdSe QDs with different fluorescence emission wavelengths has recently been reported, a complicated procedure including cell washing, cell disruption and removal of cell fragments is required because of the intracellular localizations of CdSe nanocrystals [188]. Thus, the development of a biosynthesis approach that produces fluorescence–tunable QDs extracellularly using a widely used and easily cultured microorganism without complicated post–treatments is of great importance in extending the applications of biosynthesized QDs. Although ZnS, PdS, CdS and CdSe QDs have been fabricated by microorganisms [151, 183-188], CdTe QDs, one of the most popular nanocrystals, have not been reported to be biosynthesized to date.

E.coli is a gram negative bacterium that is frequently used as a model organism in biological studies, particularly in molecular biology. Most *E.coli* strains are harmless and can be easily cultured under aerobic or anaerobic conditions at 37°C. Since ordinary *E.coli* has been reported to synthesize CdS QDs [151], it might be an ideal biofactory to microbially fabricate CdTe QDs.

In this work an approach using *E. coli* K12 (ATCC 29181) cells is investigated to biosynthesize protein–coated CdTe QDs with tunable fluorescence emission. The method allows one–step preparation of protein–coated CdTe QDs from Cd and Te precursors. The crystallinity of the biosynthesized protein–coated CdTe QDs was measured by TEM and XRD. The physical properties and cytotoxicity of them were

studied in comparison with the QDs synthesized by a conventional approach.

7.2 Preparation and Measurement

7.2.1 Biosynthesis of CdTe QDs

In the biosynthesis, *E. coli* was grown with aeration at 37°C in LB medium, a mixture containing 10 g peptone, 5 g yeast extract and 10 g NaCl per litre (pH 7.0). When the absorbance of bacteria cultures rose to 0.6 at 600 nm, 1 ml of *E. coli* solution was diluted to 45 ml with LB medium in a single necked flask and then 4 ml of 0.04 M cadmium chloride ($CdCl_2$), 100 mg of trisodium citrate dihydrate, 1 ml of 0.04 M Na_2TeO_3, 60 mg MSA and 50 mg of $NaBH_4$ were added under stirring, followed by incubation at 37°C in a shaking incubator (200 rpm). Using this approach CdTe nanocrystals could be reproducibly biosynthesized.

Bacteria–free LB medium containing bacteria–secreted proteins was prepared as follows. After one–day culture the bacteria were removed from the medium by centrifugation at 6000g for 10 min. Before biosynthesis the prepared LB medium was filtered using a polycarbonate membrane (Millipore) with a pore size of 200 nm. Subsequently, 4 ml of 0.04 M $CdCl_2$, 100 mg of trisodium citrate dihydrate, 1 ml of 0.04 M Na_2TeO_3, 60 mg of MSA and 50 mg of $NaBH_4$ were added to the medium for the biosynthesis of CdTe nanocrystals.

7.2.2 Cell Imaging Tests

The washed QDs were dissolved in PBS and linked with folic acid via 1–Ethyl–3–(3–dimethylaminopropyl) carbodiimide. Then, the functionalized QDs were incubated with *HeLa* cells for 12 hrs. The fluorescent micrographs were captured by laser scanning confocal microscopy (LSCM).

7.2.3 Sodium Dodecyl Sulfate Polyacrylamide Gel Electrophoresis (SDS–PAGE)

The collected QDs were washed three times with 50 % ethanol. After mixing with glycerol the QDs samples were loaded onto a 12% SDS–PAGE gel and electrophoresed at 90 V for 90 min. The fluorescent images were captured using a ScanArray GX scanner with UV irradiation. For the protein samples images were obtained with a scanner after staining with Commassie brilliant blue.

7.3 Optical Properties of Microbial Synthesized QDs

The UV–Vis and the PL spectra of the extracellularly bio–synthesized CdTe QDs after different incubation times were recorded to monitor the growth of the QDs (Fig. 7.1). The QD samples tested were taken from the reaction vessel at different incubation times and were centrifuged to remove bacteria without any further treatment. All samples showed well–resolved absorption maxima of the first electronic transition. With the prolongation of the incubation time a red shift of the absorption edge can be observed (Fig. 7.1A), indicating growth of CdTe QDs during

the biological treatment process. The emission spectra seemed excessively green for CdTe QDs, implying very small particles. In terms of the literature procedure [173], the average particle size of the biosynthesized QDs could be estimated from the spectra to be in the range of 2.0–3.2 nm after 9 days. As shown in Fig. 7.1B, the biosynthesized QDs possessed strong fluorescence emission. The PL emission peak position of QDs shifts from 488 (blue emission) to 551 nm (yellow–green emission) with increasing QD size because of quantum confinement. It is worthy of note that the full width at half maximum (FWHM) was ~40 nm when λ_{em} = 488 nm, reflecting the narrow particle size distribution. In addition, the value of FWHM increased from 40 to 75 nm with the growth of CdTe QDs. This phenomenon may be ascribed to the effect of Ostwald ripening [189]. The luminescence of CdTe QDs was dominated by near band edge luminescence and the PL QY of biosynthesized CdTe QDs with an emission peak at 510 nm was about 15% (compare with Rhodamine 6G in absolute ethanol according to Peng and Peng [190]). The UV–vis and PL results demonstrate that CdTe nanocrystals with tunable size–dependent emission from blue to green can be produced using *E.coli* by controlling the incubation time. In comparison with the biosynthesized emission–tunable CdSe QDs in living yeast cells [188] this extracellular synthesis approach using *E.coli* make the harvesting of QDs much easier.

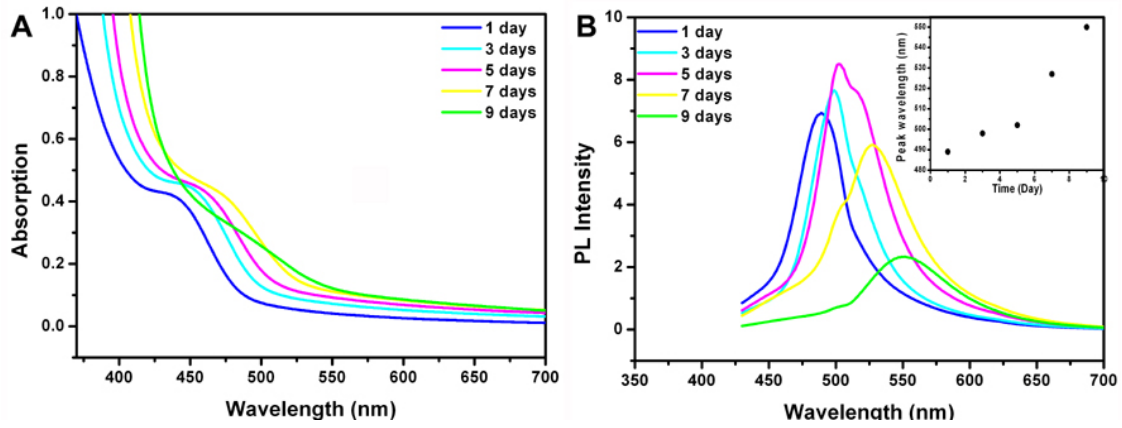

Figure 7.1 (A) UV–vis and (B) PL spectra of extracellularly biosynthesized CdTe QDs recorded after incubation with *E. coli* for 1, 3, 5, 7, 9 days, respectively. Inset: Peak wavelengths of the PL spectra plotted against incubation time.

7.4 Physical Properties of Microbial Synthesized QDs

Besides the optical properties, the physical properties are also important in determining the quality of QDs. In this study TEM and XRD were used to analyze the size and the crystallinity of the biosynthesized CdTe QDs. Many small spots can be found in the TEM image of the synthesized CdTe QDs (Fig. 7.2A), revealing the spherical particle shape and uniform size. The high resolution TEM micrograph shown in Fig. 7.2B shows that the QD size is ~2–3 nm, which is in agreement with the size estimated from the UV–vis spectra. The inset image further illustrates that the CdTe nanocrystals have lattice planes with a spacing of 0.32 nm, corresponding to the d spacing of the (111) planes of the cubic zinc blende structure of the bulk CdTe crystal. The lattice planes in the HRTEM images are also consistent with the XRD pattern (Fig. 7.2C), which exhibits the relatively strong peak (~27.5^{o}) indexed

to the (111) planes of the standard pattern for cubic CdTe [191]. These findings indicate the uniform size and good crystallinity of the biosynthesized CdTe QDs.

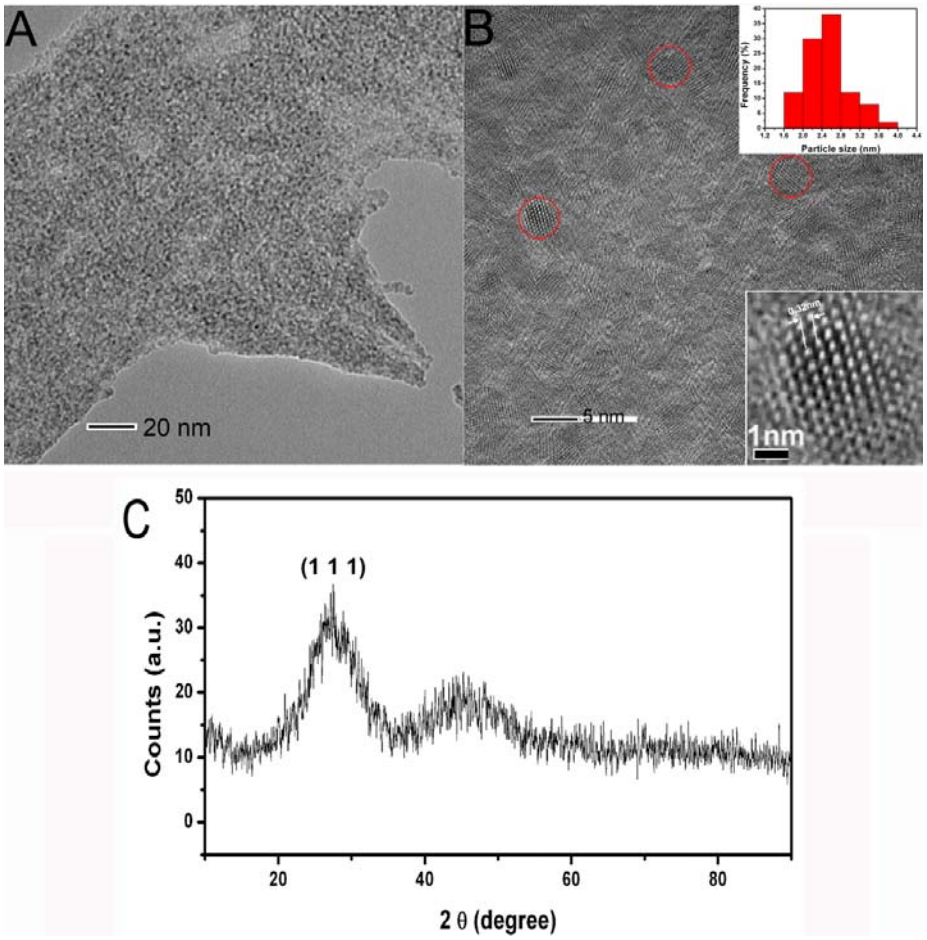

Figure 7.2 (A) TEM and (B) HRTEM images of extracellularly biosynthesized CdTe QDs. The insets show the size distribution (top) and crystallite (bottom) of the QDs. The lattice planes are marked with circles. (C) The XRD pattern of the corresponding sample.

7.5 Surface Properties of the Microbial Synthesized QDs

The good crystallinity and superior optical properties provide the opportunity for biosynthesized CdTe QDs to be utilized in different applications. The surface

properties of the QDs may further influence their biocompatibility, immobilization and functionalization in practical usage. Hence, hydrodynamic size, zeta potential and FTIR were measured to investigate the surface properties of the biosynthesized QDs. In the UV–vis and TEM characterizations the sizes of the QDs were determined to be 2–3 nm. Larger hydrodynamic sizes of QDs are shown in Fig. 7.3A due to the spreading of capping molecules in aqueous phase. By comparing the hydrodynamic size of hydrothermally and microbially synthesized QDs, it was found that the biosynthesized QDs were larger than hydrothermally synthesized MSA–capped QDs (Fig. 7.3A), suggesting the presence of larger capping materials on the biosynthesized QDs. To confirm the coating layer on the CdTe QDs' surface, zeta potential, an indication of net particle charge, was measured (Fig. 7.3B). The average zeta potentials of the biosynthesized CdTe QDs and the hydrothermally synthesized MSA–capped CdTe QDs were –36.4 and –19.1 mV, respectively, clearly showing significantly different net particle charges, indicating the existence of different coating layers on the surfaces of CdTe QDs. The strongly negative charges on the QDs surface may contribute to stable suspension of the nanocrystals in solution, offering good solubility for the easy application of biosynthesized QDs in bioimaging.

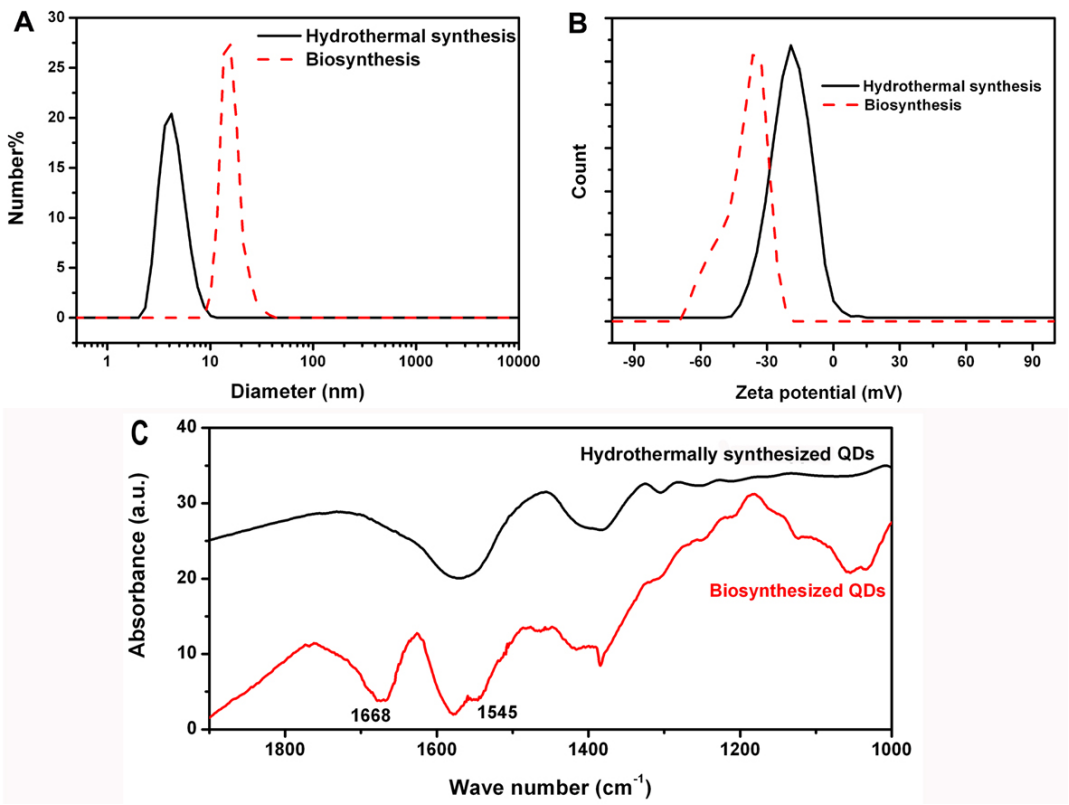

Figure 7.3 Comparisons of (A) hydrodynamic size, (B) zeta potential and (C) FTIR spectra between extracellularly biosynthesized and hydrothermally synthesized CdTe QDs

Since *E.coli* secretes a large number of proteins into the medium at different growth stages as shown in Fig. 7.4, proteins, especially metal binding proteins, may form the capping layer of the CdTe QDs. FTIR was applied to determine the chemical composition of the QD surface. Fig. 7.3C shows that the biosynthesized CdTe QDs have two infrared absorption bands centered at 1668 and 1545 cm^{-1}, which can be assigned to the bending vibrations of the amide I and amide II bands of protein molecules, respectively. Similar results were reported in studies of microbially synthesized CdS nanocrystals [186]. The data prove that the biosynthesized QDs are capped with protein molecules, which may further affect the

biocompatibility of the QDs.

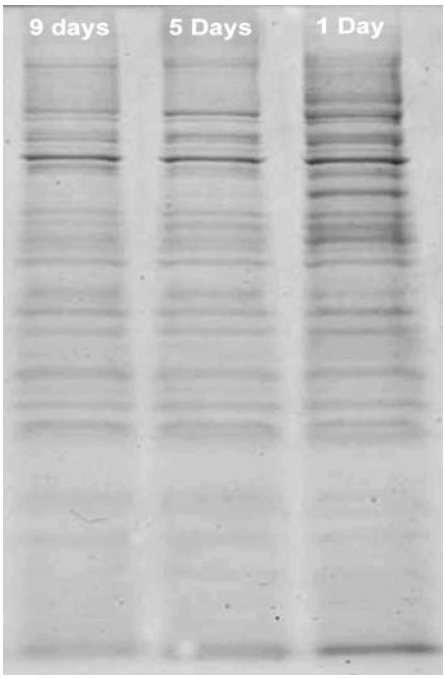

Figure 7.4 The expression profiles of bacteria–secreted proteins in the LB medium after incubation at 37 °C for 1 day, 5 days and 9 days.

7.6 Biocompatibility and Cell Imaging of the Synthesized QDs

In recent years the nanotoxicity has greatly limited the biomedical applications of QDs [192, 193]. Coating QDs with biocompatible materials is considered a good approach to modifying them in order to reduce the nanotoxicity [32, 33, 39]. In this study, protein–capped CdTe nanocrystals were produced by a biosynthetic process. A MTT assay was used to investigate the cytotoxicity of hydrothermally synthesized MSA–capped and biosynthesized QDs. Fig. 7.5A shows that the hydrothermally

synthesized QDs at concentrations > 500 nM were observed to have significant toxic effects on PC 12 cells, while the biosynthesized QDs maintained a cell viability of 92.9% even at a concentration as high as 2 μM. The results indicate that biosynthesized QDs had much better biocompatibility than the hydrothermally synthesized QDs, which can be attributed to the naturally generated proteins cap on the CdTe QDs synthesized in an environment favorable to bacteria. Folic acid, which specifically targets folate receptors on tumor cell membranes, was immobilized on the biosynthesized QDs for *in vitro HeLa* cell imaging. As shown in Fig. 7.5B, green fluorescence can be observed in the *HeLa* cells, indicating effectively labeling of the cells by the QDs. The well–spread shape of the cells also suggests good biocompatibility of the QDs. The images suggests significant potential for utilization of the QDs for *in vitro* cell imaging, as an efficient alternative or complimentary tool to conventional organic dyes.

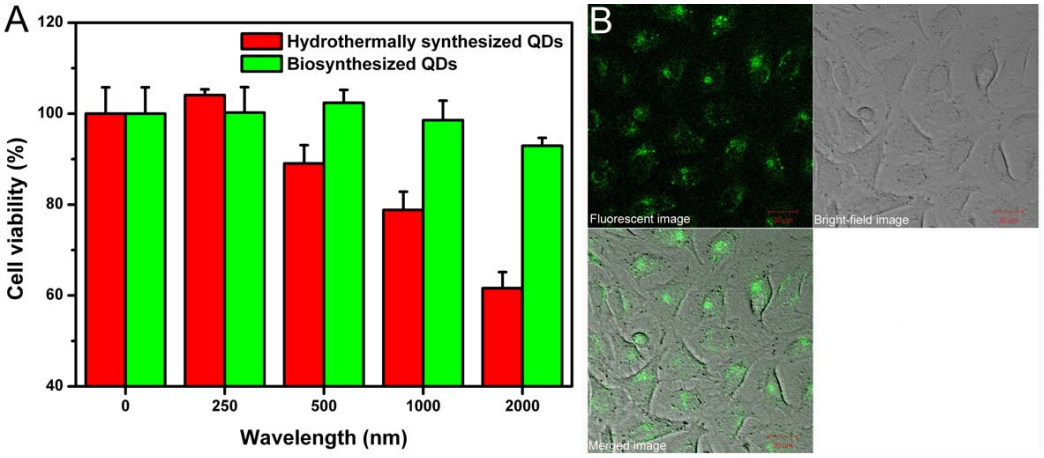

Figure 7.5 (A) Cytotoxicity of hydrothermally synthesized and biosynthesized QDs. (B) Phagocytosis of biosynthesized QDs by *HeLa* cells.

7.7 Mechanism for Extracellular Microbial Synthesis of CdTe QDs

7.7.1 Functions of Bacteria–Secreted Proteins

The protein coating layer on the QD surface may not only improve the biocompatibility of QDs, but also suggest the possible role of bacteria–secreted proteins in the biosynthetic process. In order to confirm the function of the bacteria–secreted proteins during the production of QDs, *E.coli*–free LB medium containing bacteria–secreted proteins was employed in biosynthesis. Fig. 7.6A displays the protein bands of pure LB medium and bacteria–free LB medium after one day culture of *E.coli*. Small peptides containing in the LB medium may form a broad band, which can be seen in both samples, at the bottom of the SDS–PAGE gel. The narrow band in the right lane proves the existence of bacteria–secreted proteins in the bacteria–free LB medium. After incubation at 37 °C for different times growth of the QDs was monitored using PL spectrometry (Fig. 7.6B). Within 9 days culture, a shift in the emission peak from 449 to 473 nm can be observed, evidencing the growth of QDs in the LB medium containing bacteria–secreted proteins. The emission peak of pure LB medium did not change significantly (Fig. 7.6C). The data indicate that even without bacterial cells CdTe crystals still can be synthesized and that biosynthesis of the QDs was only dependent on the bacteria–secreted proteins. In addition, QDs in the medium without bacteria grew much more slowly than those in an *E.coli* suspension. The slow growth rate may be due to the lower amount of proteins in the medium without continuous replenishment by bacteria. In a control

experiment under identical conditions but without *E.coli* or *E.coli* secreted proteins CdTe nanocrystal could not be produced, demonstrating that *E.coli* plays a critical role in the biosynthesis of CdTe QDs.

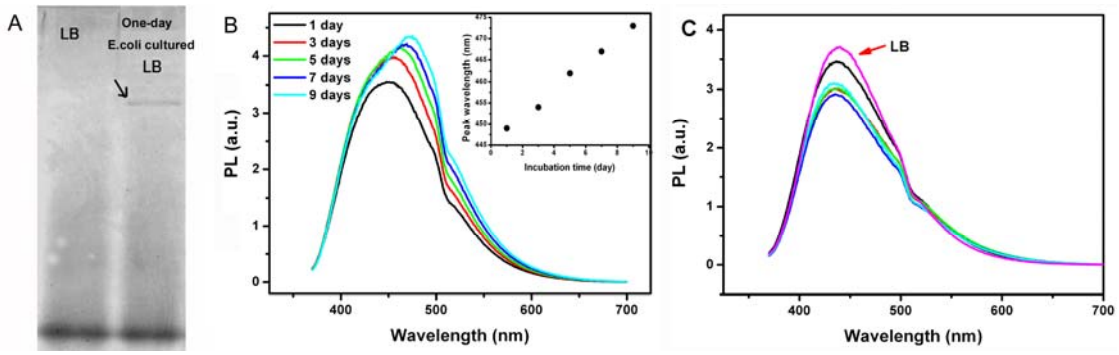

Figure 7.6 (A) SDS–PAGE gel of pure LB medium and an *E.coli*–free LB medium containing bacteria–secreted proteins. The arrow indicates the band of bacteria–secreted proteins. The molecular weight of the protein bands decreases from up to down. (B) PL spectra of biosynthesized CdTe QDs in *E.coli*–free LB medium containing bacteria–secreted proteins at different incubation times. (Inset) Peak wavelengths of PL spectra plotted against incubation time. (C) PL spectra of pure LB medium containing Cd and Te precursors after incubation 37 °C for 0, 1, 3, 5, 7 and 9 days, respectively.

7.7.2 Relation between Bacterial Growth and QD Synthesis

Since the biosynthesis progresses a relatively long period (9 days), living of the *E.coli* cells must be affected by the changes in the culture environment. The absorbence of the *E.coli* suspension at 600 nm was recorded, to determine the growth status of bacteria in the medium (Fig. 7.7A). After 1 day incubation the

absorbence reached a maximum (A_{600}=2.043), showing rapid growth of *E.coli* during this stage. The SEM image in Fig. 7.7B also displays typical rod–shaped bacteria with smooth cell surfaces. However, the absorbence decreased continuously after 3 days culture, maintaining at a stable level after 7 days. At this stage, the large numbers of bacteria exhausted the nutrients in the medium. The growth of *E.coli* was limited and many cells died. The SEM micrograph in Fig. 6.7C shows that *E.coli* cells incubated for 7 days were longer and narrower. Elongated *E.coli* cells can usually be found in environments with a strong heavy metal stress or limited nutrients [194]. The damaged surfaces also suggest death of the bacteria. During 9 days the QD emission changed from blue to yellow green while the bacteria experienced a complete life cycle. Results here further demonstrate that the biosynthesis of CdTe nanocrystals does not directly rely on living bacteria. The evidence here agrees well with the above findings in the experiment on biosynthesis in LB medium containing proteins. Interestingly, in the inset of Fig. 7.1B a clear two–stage growth with day 5 as the inflection point can be distinguished on the basis of the maximum peak shift. The second, faster growth stage may possibly be due to the release of endogenous proteins from dead *E.coli* cells after 5 days culture.

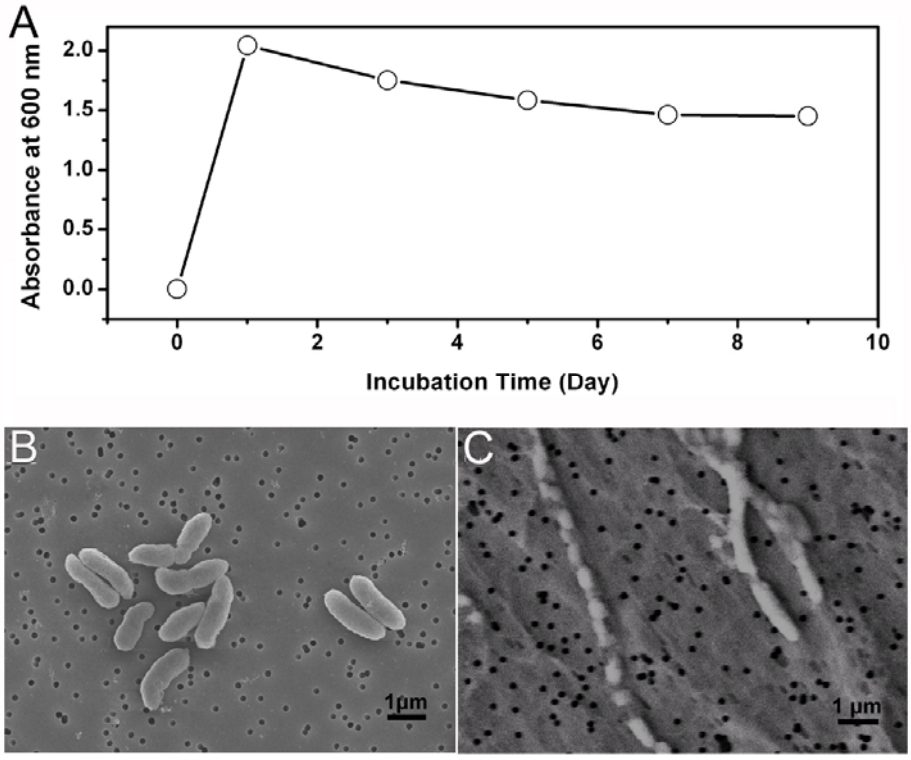

Figure 7.7 (A) Change in the bacterial amount during the biosynthesis process. (B) SEM image of *E.coli* after 1 day incubation. (C) SEM image of *E.coli* after 7 days incubation.

7.7.3 Extracellular Location of the Biosynthesized QDs

After centrifugation to harvest the QDs in LB medium, the pellet at the bottom of the tube also emits fluorescence upon UV excitation (Inset in Fig. 7.8A). The PL spectra in Fig. 7.8A reveal that the pellet possessed a weaker fluorescence with the same emission peak as that of QDs in medium, indicating the same size distribution of the QDs in both the pellet and supernatant. The confocal micrograph also shows the presence of QDs in the elongated *E.coli* (Fig. 7.8B). As mentioned in chapter 4, without surface conjugations QDs cannot be transported into the bacteria [28]. Restricted transport of intracellular and extracellular QDs would not produce the

same size distribution of QDs in both the pellet and supernatant. Thus, the QDs in the pellet may only have been located on the surface of *E.coli* cells. The TEM images prove the existence of QDs on the bacterial outer membrane (Fig. 7.8C). In chapter 4 it was found that QDs could be adsorbed onto the *E.coli* outer membrane. Thus, the QDs attached to the membrane may be the results of the surface adsorption of extracellularly synthesized CdTe nanocrystals.

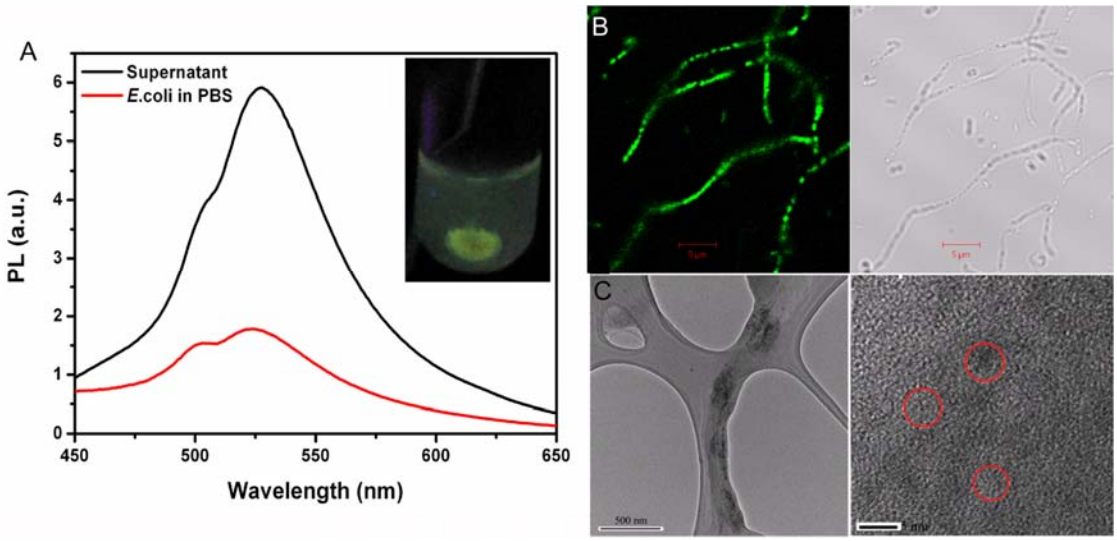

Figure 7.8 (A) PL spectra of the biosynthesized CdTe QDs in the LB supernatant (black) and centrifuged *E. coli* in PBS (red) solution incubated at 37°C for 7 days. (Inset) Photograph of centrifuged *E. coli* pellet upon UV–excitation (365nm). (B) Confocal images of *E.coli* after 7 days incubation. (C) TEM and HRTEM images of the as synthesized CdTe QDs on bacterial membrane after 7 days incubation. The lattice planes are marked with circles.

7.7.4 Mechanism

Based on the results presented above, a mechanism for the microbial synthesis

of protein coated CdTe QDs is proposed (Fig. 7.9). The CdTe nanocrystals are nucleated according to the following chemical reactions [195]:

$$4TeO_3^{2-} + 3BH_4^- = 4Te^{2-} + 3BO_2^- + 6H_2O$$

$$Cd^{2+} + Te^{2-} = CdTe$$

When the precursors are incubated with *E. coli* in LB medium the CdTe nanocrystals are nucleated extracellularly. Ostwald ripening occurs, preceding the growth of CdTe QDs with good crystallinity. At this growth stage bacteria–secreted proteins bind to components dissolved from the nucleated nanocrystals, accelerating the dissolution of small nanocrystals. Then, the binding proteins pass CdTe components to larger nanocrystals, resulting in the growth of CdTe QDs. Meanwhile, proteins cap the surface of the synthesized QDs to produce a coating layer. Selection of the Te precursor is very critical in the biosynthesis of CdTe QDs. In this work CdTe QDs were biosynthesized using Na_2TeO_3 to replace Na_2S, which was used to prepare CdS QDs [151, 196]. QDs have been found to have toxic effects on *E. coli* in above chapters. However, *E.coli* can evolve to adapt the environment and to grow under very severe conditions [197, 198]. It could be assumed that *E. coli* cells exposed to extreme environmental conditions are forced to initiate specific defense mechanisms to overcome metal ion QD stress, generating more metal binding proteins and thus promoting the biosynthesis of QDs. Further investigation needs to be carried out to confirm the mechanism proposed above.

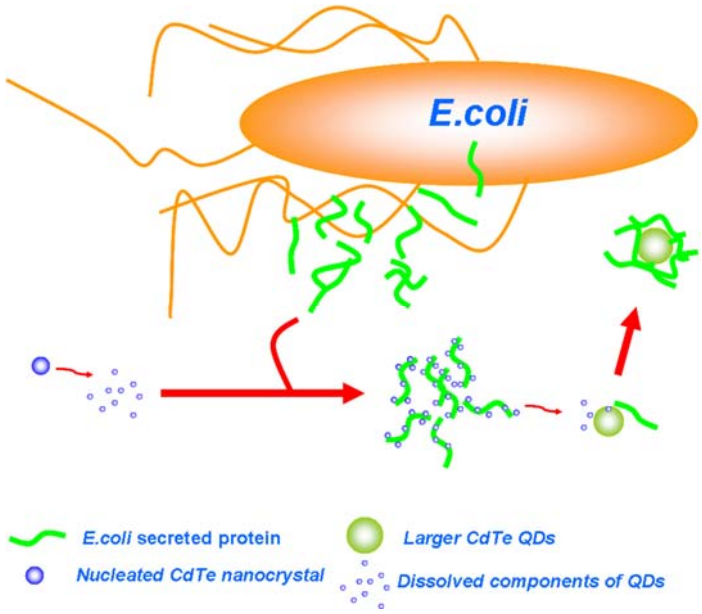

Figure 7.9 Schematic diagram of the mechanism for the biosynthesis protein–coated CdTe QDs.

7.8 Conclusions

In brief, this work demonstrates an efficient extracellular–biosynthetic method for the one–step preparation of protein–coated CdTe QDs with tunable fluorescence emission and good crystallinity. The results indicate that a surface protein capping layer on the QDs improves their biocompatibility. *HeLa* cell fluorescent images further demonstrate the capability of the QDs in *in vitro* cell imaging. Investigations of bacteria growth and bacterial morphology and QD biosynthesis in LB medium containing only *E.coli*–secreted proteins revealed that the extracellular synthesis of protein–coated CdTe QDs directly relied on the *E.coli*–secreted proteins, and a mechanism for protein–assisted biosynthesis of QDs has been proposed. Comparing

with other approaches, this method allows one–step extracellular preparation of the biocompatible protein–CdTe QD nanocomposites with tunable fluorescence emission in aqueous solutions at lower temperatures. As optical imaging agents, the low bleaching photoluminescence properties and high biocompatibility of the biosynthesized protein–coated CdTe QDs render them extremely useful for bioimaging and bio–labeling applications.

Chapter 8 Investigation of Shape Effect on Phagocytosis Using Differently Structured CdTe QD–cystine Composites[e]

8.1 Introduction

Phagocytosis is an essential component of the body's innate immunity to internalize targets with a size larger than 300 nm via the innate immune defense mechanism [199]. In drug delivery, the avoidance of phagocytosis of the drug carrier before it reaches the desired cell population is an important and challenging task. Considerable research work has been focused on factors that influence the phagocytosis of drug carriers [200]. The size and surface chemistry of carriers, two well–known factors, have been used to guide the design of new drug delivery systems [200-203]. Recently, particle shape has been also recognized as a vital factor to greatly affect the macrophage phagocytosis of particulate materials [204, 205]. To date, understanding of shape effects on phagocytosis is still limited to polymer particles. However, inorganic materials such as carbon nanotubes, layered double hydroxides, silica particles, calcium carbonate microcapsules and QDs have been also widely employed as drug carriers [206-210]. Since the surface properties can affect the phagocytosis [168, 201-203], inorganic particles with distinct surface chemistry may result in a different paradigm of the shape effect from polymer ones. Therefore, there is a need to advance knowledge of the shape effect of inorganic

[e] Reproduced in part with permission from [Z. S. Lu, Y. Qiao, X. T. Zheng, *et al.*, *Med. Chem. Comm.*, 1 (2010), 84–86] Copyright [2010] with permission from Royal Society of Chemistry publishing.

materials on phagocytosis.

8.2 Preparation and Measurement

8.2.1 Synthesis of CdTe QD–Cystine Composites

CdTe QD–cystine composites were fabricated with a procedure similar to the approach used in QD synthesis, with minor modifications. In brief, 2 mL of cadmium chloride solution (0.04 M) was diluted in 22.5 mL of deionized water, and then 800 mg of trisodium citrate dehydrate, 0.5 mL of sodium telluride solution (0.04 M), certain amounts of L–cysteine, and 15 mg of sodium borohydride were added with vigorous stirring. After 15 min, the resulting mixture solution was loaded into a Teflon–lined stainless steel autoclave with a volume of 75 mL. The autoclave was maintained at 180°C for 40 min and then cooled to room temperature with flowing water. As described in the previous work [179], L–cysteine was oxidized to L–cystine, in which CdTe nanocrystals were incorporated to form precipitates. By controlling the amount of L–cysteine added (6.0 mg, 12.5mg and 25 mg) different shaped CdTe QD–cystine composite particles were produced. The precipitates were collected by centrifugation at 6000 g for 10 min. After washing with water three times, the composite particles were suspended in water for further characterization.

8.2.2 Time–Lapse LSCM Characterization

The cells were cultured at a density of $2\times10^5/cm^2$ on 5cm round glass coverslips

for 24 hrs under standard culture conditions. Before each measurement, the coverslip was dammed with a home–made chamber that allowed the cell–attached surface of the coverslip to be immersed in 1 mL fresh culture medium. 50 μL colloidal suspension of composite particles was injected into the culture medium and bright–field images as well as fluorescent images were captured every 1 min for 1 hr by the confocal microscope. The observation area was randomly selected from the coverslip. Bright–field and fluorescent images were merged to display the behaviors of the particles and macrophage cells. Typical stages of phagocytosis were selected to compose time–series images to better exhibit the internalization process.

8.2.3 Internalization Experiment

The internalization experiment was conducted following a published procedure, with modifications [211]. Particles were incubated with the cells over a time course range from 30 min to 4 hrs. After specific periods of incubation, the cells were washed with PBS three times to remove free particles. A cell scraper was applied to detach the cells from the culture plate. The collected cells were observed under a microscope. The internalization percentage was calculated with the following formula. 3 individual tests were repeated and at least 50 cells were counted in each test.

$$Internalization\ percentage(\%) = \frac{Number\ of\ cells\ with\ particles}{Number\ of\ counted\ cells} \times 100\%$$

8.3 Morphology and Surface Properties of CdTe QD–Cystine Composites

In this work, various shaped CdTe QD–cystine composites synthesized via a one–pot cysteine–assisted hydrothermal approach were utilized to study the shape effects on macrophage phagocytosis. As described in previous works [137, 179, 212, 213], in the synthesis process L–cysteine was oxidized to L–cystine, with which CdTe nanocrystals were incorporated to form precipitates. By adjusting the amount of L–cysteine in the precursor mixtures, sphere, rod and needle structures within a range of sizes phagocytosable by macrophages were obtained (Insets of Fig. 8.1), which could be used to resemble the morphologies of common macrophage targets such as pollen, bacteria and worms.

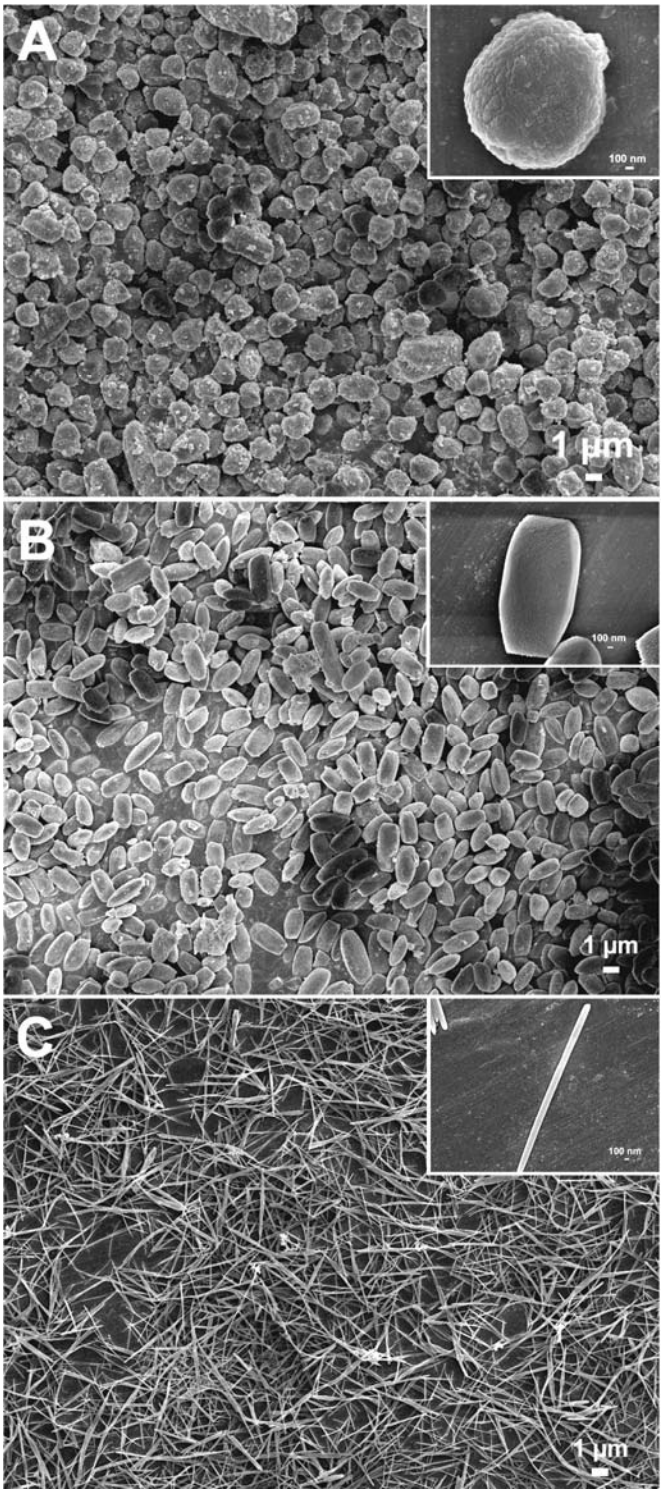

Figure 8.1 SEM micrographs of CdTe QD–cystine composites with controllable shapes: (A) microspheres, (B) microrods and (C) microneedles.

Since surface chemistry is a critical factor for the phagocytosis of particles, it is

of great importance to precisely control the surface properties of the synthesized microstructures to avoid possible interferences on the following phagocytosis experiments. FTIR was performed to identify the surface functional groups of each composite. As shown in Fig. 8.2, the IR adsorption bands at 2905 and 467 cm^{-1}, which can be assigned respectively to CH_2–S asymmetric stretching and S–S stretching vibration, confirm the oxidation of cysteine to cystine. The bands indexed the NH^{3+} deformation at 1602 and 1560 cm^{-1} validate the existence of NH_2 groups from the cystine. By comparing the FTIR spectra of the three composites, it is observed that they possess the same IR bands, indicating that the surface properties of the synthesized products are identical. Therefore, the difference caused by the surface chemical properties is negligible in the following phagocytosis experiment.

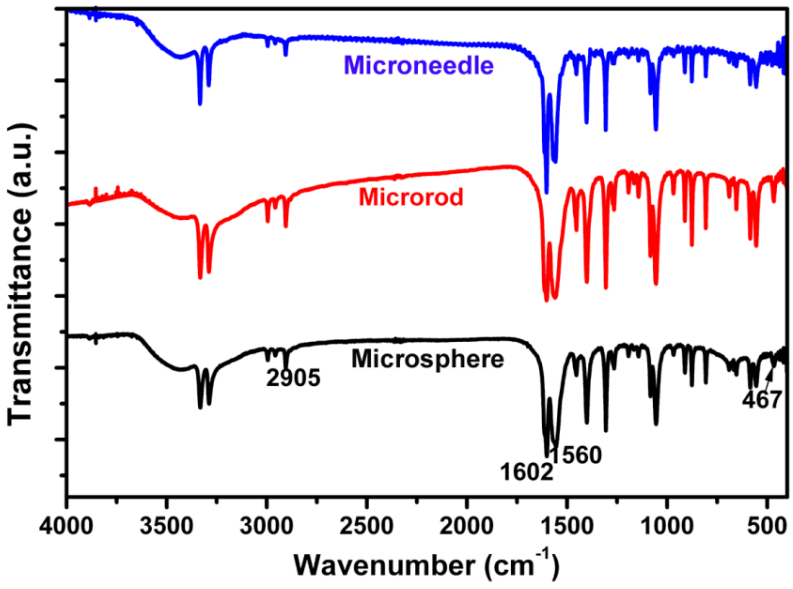

Figure 8.2 FTIR spectra of CdTe QD–cystine composites with sphere, rod and needle shapes.

8.4 Cellular Internalization Profiles of CdTe QD–Cystine Composites

RAW 264.7 (Mouse leukaemic monocyte macrophage cell line) cells were used as model macrophages. Quantitatively experimental study evidently reveals that the synthesized microcomposite shape can significantly affect the macrophage phagocytosis (Fig. 8.3). Over a 4–hr duration, the microspheres exhibit the highest degree of internalization (80%) and the fastest phagocytosis rate (ultimate internalization ratio is reached within one hr), whilst almost no internalization of the needle–shaped species occurs, clearly indicating significant effect of shape on the macrophage phagocytosis.

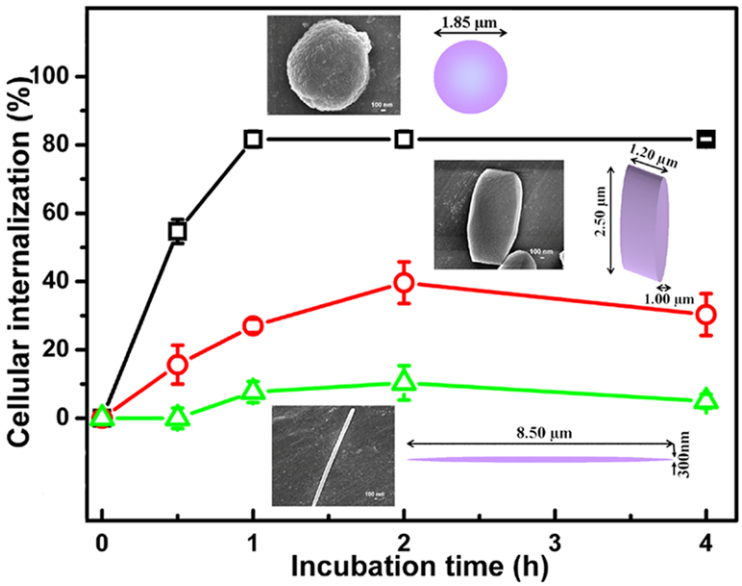

Figure 8.3 Cellular internalization profiles of sphere (square), rod (dot) and needle (triangle) shaped CdTe QD–cystine microcomposites over 4 hr at room temperature (n≥50). Insets show the morphologies of the CdTe QD–cystine composites.

8.5 Entrapment and Transportation of the Composites

8.5.1 Entrapment and Transportation of the Sphere–Shaped Composites

To better illustrate entrapment and transportation of the composite particles in macrophages, time–lapse LSCM and SEM were used to measure the phagocytosis process. As shown in Fig. 8.4A, the macrophage cell stretches its pseudopodia to adhere to the microsphere and then slowly transports it into the cell. The process may involve entrapment of the microsphere to form a phagosome and transportation of the phagosome, both of which are the primary characteristics of phagocytosis. Fig. 8.4B displays a microsphere (purple–colored) entrapped by a macrophage (olive–colored), corresponding to the 5 min LSCM image. The circled protrusion of the cell membrane indicates an internalized microsphere being transported within the cell. After internalization, the enclosed membrane forms a phagosome, which can later fuse with a lysosome to produce an acidic phagolysosome containing digestive enzymes [214]. The smaller size of the translocated protrusion than the original microsphere may be due to a partial degradation of the sphere–shaped CdTe QD–cystine particle in the phagolysosome.

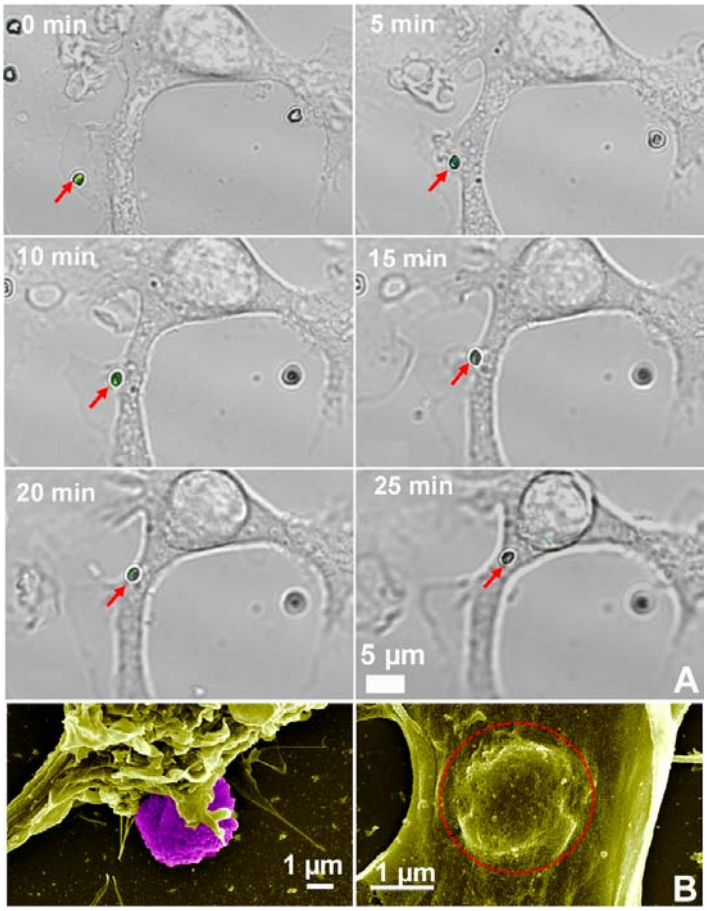

Figure 8.4 LSCM (A) and SEM (B) micrographs of the macrophage phagocytosis of CdTe QD–cystine microspheres. The red arrow indicates the microspheres. The red circle marks a microsphere inside the macrophage.

8.5.2 Entrapment and Transportation of the Rod–Shaped Composites

Unlike the microsphere, the orientation of the cell–attached CdTe QD–cystine microrod determines the local cell shape at the initial cell–particle contact point. In microrod phagocytosis, two extreme cases, in which the side (indicated with a circle, Fig. 8.5A) and the end (indicated with an arrow) of microrods as the initial contact points were investigated. From the emitted green fluorescence, the microrod

translocation can be clearly observed from the LSCM images. A microrod with the initial end–contact is taken up by the macrophage, while no engulfment is observed from the microrods with the initial side–contact in the same time course. The SEM images show an end–contacted microrod in the internalization, a side–contacted microrod in the internalization, and an internalized microrod in a phagosome, respectively (from left to right in Fig. 8.5B). The preference of macrophages for the end contact–initiated phagocytosis is suggested by comparison of the images. The results also confirm that the phagocytosis of microrods is strongly dependent on the local shape of the particle at the initial contact point with the cell, which mainly relies on the orientation of the particle.

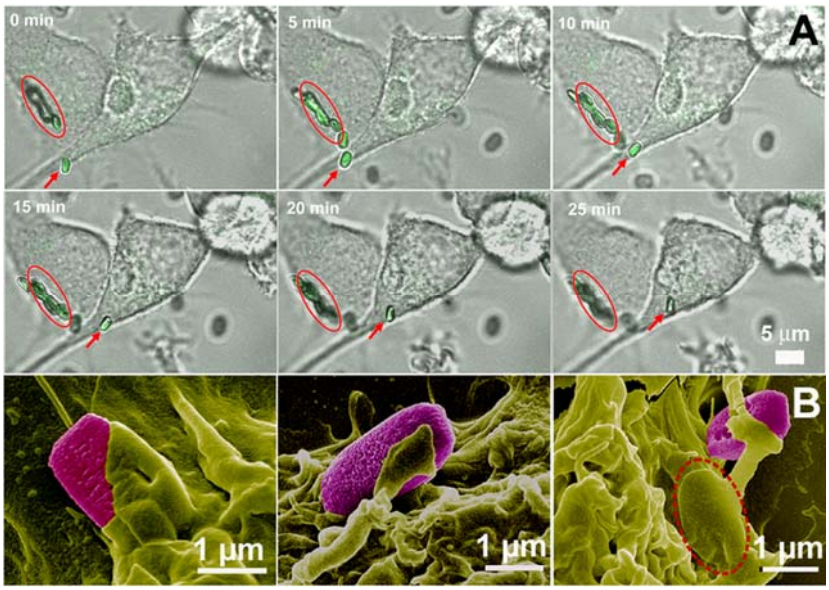

Figure 8.5 LSCM (A) and SEM (B) micrographs of macrophage phagocytosis of CdTe QD–cystine microrods. The red arrow and circle in (A) indicate end– and side–contacted microrods, respectively. The red circle in (B) indicates an internalized microrod.

8.5.3 Entrapment and Transportation of the Needle–Shaped Composites

Phagocytosis processes of both side– and end–contacted composite needles (with an aspect ratio of ~28) were studied. As shown in Fig. 8.6, neither the end nor the side contacted needles were engulfed by the macrophage cells. Interestingly, it is observed that the macrophages are trying to capture the particles by moving their surface lamellar–structures (data not shown), indicating the presence of an active way for the macrophages to capture particles.

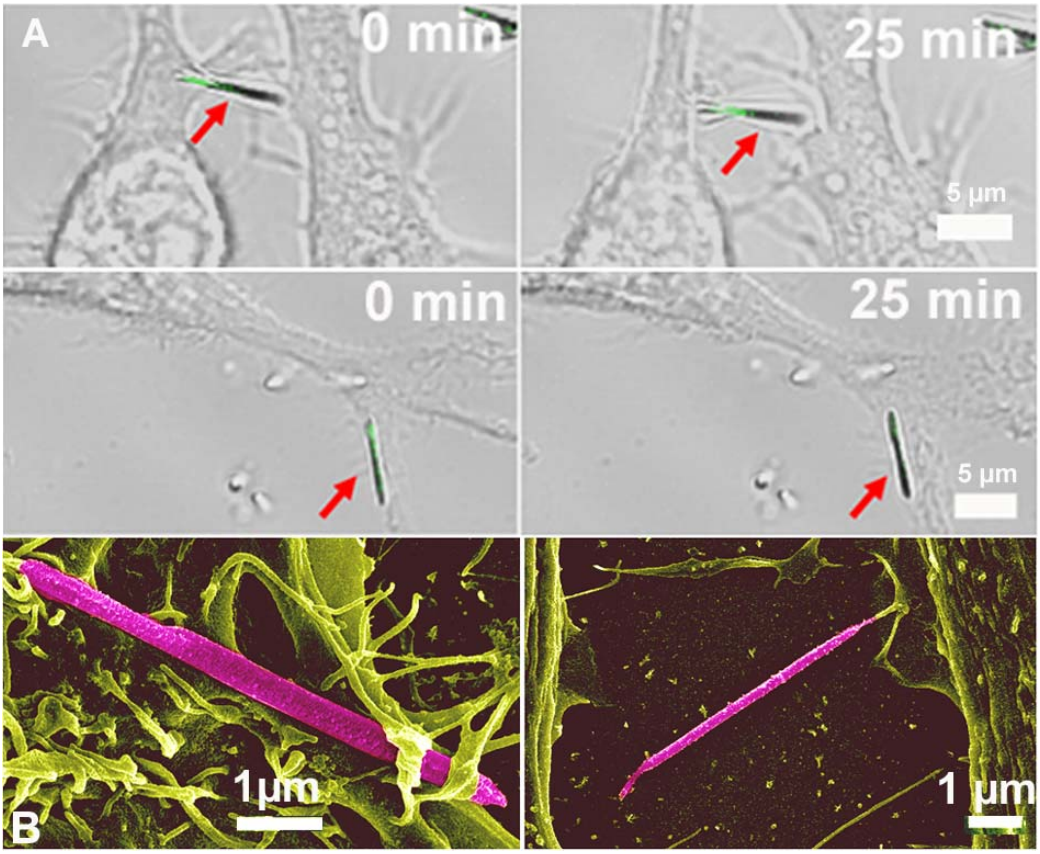

Figure 8.6 LSCM (A) and SEM (B) micrographs of macrophage phagocytosis of CdTe QD–cystine microneedles. The red arrow indicates cell–contacted microneedles.

8.6 Mechanism

A macrophage cell is favorite to internalize targets with the size of 0.3-3 μm. Phagocytosis of a particle begins with the formation of a phagocytic cup [215], in which the macrophage cell changes shape by growing out projections called pseudopodia to surround the particle. The membrane fusion of pseudopodia results in the formation of an intracellular vesicle followed by fusing with a lysosome to produce an acidic phagolysosome containing digestive enzymes. Since the microcomposite is not stable in an acidic environment, it may be decomposed to release heavy metal ions, further leading to toxic effects to the macrophage cells. The balance between driving forces from the actin polymerization and the surface energy of the distorting cell membrane is possibly responsible for the growth of a phagocytic cup [215, 216]. Since the actin polymerization force is constant in a cell, the surface energy of a cell membrane, which relies on the local curvature of the membrane, may be the key factor in the formation of a phagocytic cup. For the side–contacted rod and needle (Fig. 8.7), the ends with high curvature at the half–cup stage are very likely to cause a higher membrane surface energy, thus resulting in a large distorting force to exceed the maximum force provided by the actin polymerization and to stall the growing ends of the phagocytic cup. Thus, the macrophage cannot phagocytose the side–contacted rod– or needle–shaped particles. Engulfment inhibition by a high curvature surface has been shown in a polymer oblate particle system [205]. Although the needle particle in the end contact mode

does not have the high curvature–caused force barrier, the extremely sharp end tip that is out of the phagocytosable size range (0.3–10μm) may limit its phagocytosis even with the end contact. Interestingly, in an early study of the protein–coated polymer particles with long lengths (~10μm) and sharp ends phagocytosis was observed [217], showing a distinct behavior from the CdTe QD–cystine particles revealed in this work. Since polymer and CdTe QD–cystine particles have different surface properties [201-203], the different adsorbed protein layer might be the reason to cause the distinct phagocytosis behavior of the elongated inorganic particles discovered in this work. Bending of polymer particles has been observed, suggesting that elongated particles may not maintain their original shapes in the process of cell–particle interaction [217]. On the other hand, the inorganic CdTe QD–cystine composite particles are apparently rigid, and thus can maintain their straight needle shape to cause the inhibition of phagocytosis.

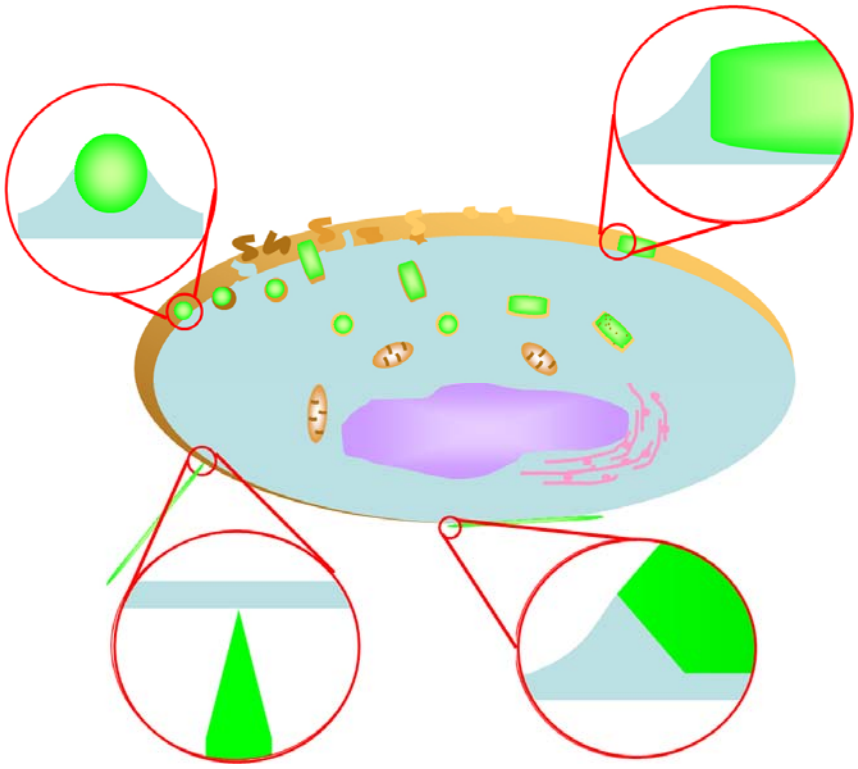

Figure 8.7 Schematic diagram of the response of macrophage phagocytic cups to an attached microsphere, a side–contacted microrod, a side–contacted microneedle and an end–contacted microneedle.

8.7 Conclusions

In summary, different shaped CdTe QD–cystine composites were synthesized to investigate the material shape effects on macrophage phagocytosis. The results indicate that the shape of inorganic particles can significantly influence the macrophage phagocytosis via the local cell shape at the initial cell–particle contact point. Macrophage–attached particles with high curvature barriers to the formation of phagocytic cup inhibit the uptake process. Furthermore, even if the particles bind

to the cells without high curvature barriers, the extremely sharp end can still stall the internalization due to the phagocytosis unfavorable size, showing a distinct feature from the polymer particles. These discoveries not only provide scientific insights into the shape dependent macrophage responses, but also offer a strategy to design optimal inorganic drug carriers that can eliminate phagocytosis from macrophages before reaching the desired cell populations.

Chapter 9 General Conclusions and Directions for Further Research

9.1 General Conclusions

In this dissertation, advances in research into QDs and their nanocomposites, in particular their antimicrobial properties and utility in biomedical applications, were thoroughly reviewed, and specially designed QD nanocomposites were developed for biomedical applications in accordance with the study goals. A primary accomplishment of this study was its demonstration of the antimicrobial activity of CdTe–core QDs for the first time in nanomaterial research. Specifically, the results of several bactericidal experiments indicated that CdTe QDs killed bacteria in a concentration–dependent manner by binding on the bacterial surface and negatively affecting the functioning of cellular antioxidative systems, including the down–regulation of antioxidative genes, and reduction of antioxidative enzyme activities. These results further indicate that the mechanism behind the bactericidal activity of CdTe QDs is based on the formation of a QD–bacteria complex and a QD–related ROS–mediated pathway.

In addition to their bactericidal capacity, CdTe QDs were found to have the capacity to inhibit bacterial growth by blocking cell division via a process in which QD–generated ROS, polypeptide or amino–acid adsorption on the QD surface, as well as fluorescence and ROS quenching are involved. Because the antimicrobial concentration of QDs is ~100 or even ~1000 times lower than the level reported to

be toxic to mammalian cells [31], QDs have high potential as novel antimicrobial materials with excellent optical properties. However, the use of QDs as antimicrobial materials should be conducted in a cautious and limited manner until their long–term toxic effects are completely understood and their biocompatibility is significantly improved.

To overcome the nanotoxicity and maintain the fluorescence emission of CdTe QDs, ZrO_2 was employed for the first time to coat QDs in the fabrication of QD nanocomposites using the reverse microemulsion approach. The prepared ZrO_2–QD nanocomposites were ~30 nm in diameter, a suitable size for biological applications, and found to possess a high level of fluorescence and allow for a time–dependent increase of emission under 350 nm of light illumination. Having been found able to effectively label *HeLa* cells, ZrO_2–QD nanocomposites show great promise as biocompatible nanomaterials with a high level of fluorescence that may be able to replace or complement QDs in biomedical applications.

Although surface coating can greatly reduce the nanotoxicity of QDs, the complex fabrication procedures involved in doing so greatly limits the application of surface–coated QDs. This research developed a one–step method for the microbial synthesis of protein–CdTe QD nanocomposites with a tunable level of fluorescence emission and a high level of crystallinity in which the surface protein capping layer on the QDs not only improves QD biocompatibility but also provides the functional groups for the bioprobe conjugation necessary for QD use in *in vitro HeLa* cell

imaging. The extracellular synthesis of protein–QD nanocomposites was found to directly depend on the *E. coli*–secreted proteins.

Responding to the need to investigate the interaction of biosystems with variously structured QD nanocomposites, the responses of macrophages to differently shaped particles were investigated using novel CdTe QD–cystine composites as models. It was found that the shape of the particles significantly influences macrophage phagocytosis via the local cell response at the initial cell–particle contact point, as well as that even if the particles bind to the cells with a phagocytosis–favorable local shape, the high aspect ratio still blocks the uptake process. These findings provide scientific insight into shape–dependent phagocytosis responses that is essential for the development and design of drug carriers.

In summary, this project expanded the biomedical applications of CdTe QDs and their nanocomposites, especially in antimicrobial, tumor–cell imaging, and macrophage phagocytosis, and described a novel approach to the fabrication of QD–based nanocomposites of various structures with a lower level of cytotoxicity compared to traditional materials. The findings of this project thus not only advance fundamental knowledge of the interaction between nanomaterials and biosystems but also reveal the great medical and commercial potential of CdTe QDs.

9.2 Directions for Further Research

Despite their relatively high level of fluorescence emission, QDs are currently

unable to meet the requirements necessary for use in practical applications targeting complex biosystems. To further expand their practical biomedical applications, QDs must be combined with other materials with unique properties to construct multifunctional QD nanocomposites. Further advances in material science and nanoengineering will lead to the development of a greater number of nanomaterials with superior chemical and physical properties and the nanocomposing of QDs with various novel nanomaterials for unique functions.

In this project, QD–cystine nanocomposites with distinct structures were developed and their role in macrophage phagocytosis was investigated. Although the utility of nanomaterials in many biosystems and applications requires that they possess a critical size, shape, and/or structure, these characteristics remain difficult or impossible to control. Future research should therefore endeavor to develop QD–based nanocomposites of various unique shapes and engineered nanostructures to extend their application to specific biosystems and improve bioimaging and biosensing performance, especially in drug delivery and therapy.

Last but not least, *in vivo* studies must be conducted to investigate the impact of the complex, real–world biological environment on QD–based nanodevices. While coated QD nanocomposites have been developed to reduce the level of QD nanotoxicity, their biocompatibility has only been evaluated with *in vitro* cultured cells, whose characteristics, unlike those of much more complex animal and human biological systems, can be carefully controlled. The impact of nanomaterials on the

pharmacokinetics, protein adsorption, immunoresponse, biodistribution, degradation, and excretion pathways within animal and human systems must be investigated before using nanodevices in *in vivo* biomedical or clinical applications. Such *in vivo* studies will greatly advance understanding of the *in vivo* behaviors of QD nanomaterials and the means of limiting their nanotoxicity.

Abbreviates

QD: quantum dot

AFM: atomic force microscope

FESEM: field emmission scanning electronic microscope

FTIR: fourier transform infrared

XRD: X–ray diffraction

HRTEM: High–resolution transmission electron microscopy

MSA: mercaptosuccinic acid

LB: Lysogeny broth

UV–VIS: UV–visible

PL: photoluminescence

LSCM: laser scanning confocal microscopy

PBS: phosphate–buffered solution

ROS: reactive oxygen species

PCR: polymerase chain reaction

SOD: superoxide dismutase

DNPH: 2,4–dinitrophenylhydrazine

TCA: trichloroacetic acids

TBARS: thiobarbituric reacting substances

CFU: colony–forming unit

SDS–PAGE: sodium dodecyl sulfate polyacrylamide gel electrophoresis

References

1. Bao, H.F., X.Q. Cui, C.M. Li, Y. Gan, J. Zhang, and J. Guo, *Photoswitchable semiconductor bismuth sulfide (Bi2S3) nanowires and their self-supported nanowire arrays.* Journal of Physical Chemistry C, 2007. **111**(33): p. 12279-12283.
2. Bao, S.J., Q.L. Bao, C.M. Li, and Z.L. Dong, *Novel porous anatase TiO2 nanorods and their high lithium electroactivity.* Electrochemistry Communications, 2007. **9**(5): p. 1233-1238.
3. Qiao, Y., S.J. Bao, C.M. Li, X.Q. Cui, Z.S. Lu, and J. Guo, *Nanostructured polyanifine/titanium dioxide composite anode for microbial fuel cells.* Acs Nano, 2008. **2**: p. 113-119.
4. Song, Q.L., C.M. Li, M.L. Wang, X.Y. Sun, and X.Y. Hou, *Role of buffer in organic solar cells using C-60 as an acceptor.* Applied Physics Letters, 2007. **90**(7).
5. Sun, C.Q., L.K. Pan, C.M. Li, and S. Li, *Size-induced acoustic hardening and optic softening of phonons in InP, CeO2, SnO2, CdS, Ag, and Si nanostructures.* Physical Review B, 2005. **72**(13).
6. Xiao, Y.H. and C.M. Li, *Nanocomposites: From fabrications to electrochemical bioapplications.* Electroanalysis, 2008. **20**(6): p. 648-662.
7. Ariga, K., X.L. Hu, S. Mandal, and J.P. Hill, *By what means should nanoscaled materials be constructed: molecule, medium, or human?* Nanoscale, 2010. **2**(2): p. 198-214.
8. Cai, Y.R. and J.M. Yao, *Effect of proteins on the synthesis and assembly of calcium phosphate nanomaterials.* Nanoscale, 2010. **2**(10): p. 1842-1848.
9. Cooper, D.R. and J.L. Nadeau, *Nanotechnology for in vitro neuroscience.* Nanoscale, 2009. **1**(2): p. 183-200.
10. Dhand, C., M. Das, G. Sumana, A.K. Srivastava, M.K. Pandey, C.G. Kim, M. Datta, and B.D. Malhotra, *Preparation, characterization and application of polyaniline nanospheres to biosensing.* Nanoscale, 2010. **2**(5): p. 747-754.
11. Xie, X.W. and W.J. Shen, *Morphology control of cobalt oxide nanocrystals for promoting their catalytic performance.* Nanoscale, 2009. **1**(1): p. 50-60.
12. Elisabeth S. Papazoglou and A. Parthasarathy, *Bionanotechnology*. SYNTHESIS LECTURES ON BIOMEDICAL ENGINEERING #7, ed. J.D. Enderle. 2007: Morgan & Claypool.
13. Hao, R., R.J. Xing, Z.C. Xu, Y.L. Hou, S. Gao, and S.H. Sun, *Synthesis, Functionalization, and Biomedical Applications of Multifunctional Magnetic Nanoparticles.* Advanced Materials, 2010. **22**(25): p. 2729-2742.
14. Haun, J.B., T.J. Yoon, H. Lee, and R. Weissleder, *Magnetic nanoparticle biosensors.* Wiley Interdisciplinary Reviews-Nanomedicine and Nanobiotechnology, 2010. **2**(3): p. 291-304.
15. Jha, N. and S. Ramaprabhu, *Development of Au nanoparticles dispersed carbon nanotube-based biosensor for the detection of paraoxon.* Nanoscale, 2010. **2**(5): p. 806-810.
16. Kim, C.K., P. Ghosh, and V.M. Rotello, *Multimodal drug delivery using gold nanoparticles.* Nanoscale, 2009. **1**(1): p. 61-67.
17. Mi, C.C., J.P. Zhang, H.Y. Gao, X.L. Wu, M. Wang, Y.F. Wu, Y.Q. Di, Z.R. Xu, C.B. Mao, and S.K. Xu, *Multifunctional nanocomposites of superparamagnetic (Fe3O4) and NIR-responsive rare earth-doped up-conversion fluorescent (NaYF4 : Yb, Er) nanoparticles and their applications in biolabeling and fluorescent imaging of cancer cells.* Nanoscale, 2010. **2**(7): p. 1141-1148.
18. Moros, M., B. Pelaz, P. Lopez-Larrubia, M.L. Garcia-Martin, V. Grazu, and J.M. de la Fuente,

Engineering biofunctional magnetic nanoparticles for biotechnological applications. Nanoscale, 2010. **2**(9): p. 1746-1755.

19. Ho, Y.P. and K.W. Leong, *Quantum dot-based theranostics.* Nanoscale, 2010. **2**(1): p. 60-68.
20. Pinaud, F., S. Clarke, A. Sittner, and M. Dahan, *Probing cellular events, one quantum dot at a time.* Nature Methods, 2010

7(4): p. 275-285.

21. Zrazhevskiy, P., M. Sena, and X.H. Gao, *Designing multifunctional quantum dots for bioimaging, detection, and drug delivery.* Chemical Society Reviews, 2010.
22. Klostranec, J.M. and W.C.W. Chan, *Quantum dots in biological and biomedical research: Recent progress and present challenges.* Advanced Materials, 2006. **18**(15): p. 1953-1964.
23. Yu, W.W., E. Chang, R. Drezek, and V.L. Colvin, *Water-soluble quantum dots for biomedical applications.* Biochemical and Biophysical Research Communications, 2006. **348**(3): p. 781-786.
24. Allen, P.M., W.H. Liu, V.P. Chauhan, J. Lee, A.Y. Ting, D. Fukumura, R.K. Jain, and M.G. Bawendi, *InAs(ZnCdS) Quantum Dots Optimized for Biological Imaging in the Near-Infrared.* Journal of the American Chemical Society, 2010. **132**(2): p. 470-+.
25. Du, Y.P., B. Xu, T. Fu, M. Cai, F. Li, Y. Zhang, and Q.B. Wang, *Near-infrared Photoluminescent Ag2S Quantum Dots from a Single Source Precursor.* Journal of the American Chemical Society, 2010. **132**(5): p. 1470-+.
26. Ma, Q.A. and X.G. Su, *Near-infrared quantum dots: synthesis, functionalization and analytical applications.* Analyst, 2010. **135**(8): p. 1867-1877.
27. Miao, S.D., S.G. Hickey, B. Rellinghaus, C. Waurisch, and A. Eychmuller, *Synthesis and Characterization of Cadmium Phosphide Quantum Dots Emitting in the Visible Red to Near-Infrared.* Journal of the American Chemical Society, 2010. **132**(16): p. 5613-+.
28. Kloepfer, J.A., R.E. Mielke, and J.L. Nadeau, *Uptake of CdSe and CdSe/ZnS quantum dots into bacteria via purine-dependent mechanisms.* Appl. Environ. Microbiol., 2005. **71**(5): p. 2548-57.
29. Dwarakanatha, S., J.G. Bruno, T.N. Athmaram, G. Bali, D. Vattem, and P. Rao, *Antibody-quantum dot conjugates exhibit enhanced antibacterial effect vs. unconjugated quantum dots.* Folia Microbiol (Praha), 2007. **52**(1): p. 31-4.
30. Derfus, A.M., W.C.W. Chan, and S.N. Bhatia, *Probing the cytotoxicity of semiconductor quantum dots.* Nano Letters, 2004. **4**(1): p. 11-18.
31. Hardman, R., *A toxicologic review of quantum dots: toxicity depends on physicochemical and environmental factors.* Environ Health Perspect, 2006. **114**(2): p. 165-72.
32. Tan, W.B., N. Huang, and Y. Zhang, *Ultrafine biocompatible chitosan nanoparticles encapsulating multi-coloured quantum dots for bioapplications.* Journal of Colloid and Interface Science, 2007. **310**(2): p. 464-470.
33. Nie, Q.L., W.B. Tan, and Y. Zhang, *Synthesis and characterization of monodisperse chitosan nanoparticles with embedded quantum dots.* Nanotechnology, 2006. **17**(1): p. 140-144.
34. Nehilla, B.J., P.G. Allen, and T.A. Desai, *Surfactant-free, drug-quantum-dot coloaded poly(lactide-co-glycolide) nanoparticles: Towards multifunctional nanoparticles.* ACS Nano, 2008. **2**(3): p. 538-544.
35. Yin, W., H. Liu, M.Z. Yates, H. Du, F. Jiang, L. Guo, and T.D. Krauss, *Fluorescent quantum dot-polymer nanocomposite particles by EmulsiflcationISolvent evaporation.* Chemistry of

Materials, 2007. **19**(12): p. 2930-2936.

36. Yu, W.W., E. Chang, J.C. Falkner, J.Y. Zhang, A.M. Al-Somali, C.M. Sayes, J. Johns, R. Drezek, and V.L. Colvin, *Forming biocompatible and nonaggregated nanocrystals in water using amphiphilic polymers.* Journal of the American Chemical Society, 2007. **129**(10): p. 2871-2879.
37. Dembski, S., C. Graf, T. Kruger, U. Gbureck, A. Ewald, A. Bock, and E. Ruhl, *Photoactivation of CdSe/ZnS quantum dots embedded in silica colloids.* Small, 2008. **4**(9): p. 1516-1526.
38. Koole, R., M.M. van Schooneveld, J. Hilhorst, C.D. Donega, D.C. t Hart, A. van Blaaderen, D. Vanmaekelbergh, and A. Meijerink, *On the incorporation mechanism of hydrophobic quantum dots in silica spheres by a reverse microemulsion method.* Chemistry of Materials, 2008. **20**(7): p. 2503-2512.
39. Selvan, S.T., P.K. Patra, C.Y. Ang, and J.Y. Ying, *Synthesis of silica-coated semiconductor and magnetic quantum dots and their use in the imaging of live cells.* Angewandte Chemie-International Edition, 2007. **46**(14): p. 2448-2452.
40. Nel, A., T. Xia, L. Madler, and N. Li, *Toxic potential of materials at the nanolevel.* Science, 2006. **311**(5761): p. 622-7.
41. Murray, C.B., D.J. Norris, and M.G. Bawendi, *Synthesis and characterization of nearly monodisperse CdE (E = S, Se, Te) Semiconductor nanocrystallites.* Journal of the American Chemical Society, 1993. **115**(19): p. 8706-8715.
42. Mokerov, V.G., Y.V. Fedorov, L.E. Velikovski, and M.Y. Scherbakova, *New quantum dot transistor.* Nanotechnology, 2001. **12**(4): p. 552-555.
43. Lee, W., S.H. Kang, J.Y. Kim, G.B. Kolekar, Y.E. Sung, and S.H. Han, *TiO2 nanotubes with a ZnO thin energy barrier for improved current efficiency of CdSe quantum-dot-sensitized solar cells.* Nanotechnology, 2009. **20**(33).
44. Stouwdam, J.W. and R.A.J. Janssen, *Red, green, and blue quantum dot LEDs with solution processable ZnO nanocrystal electron injection layers.* Journal of Materials Chemistry, 2008. **18**(16): p. 1889-1894.
45. Ustinov, V.M., A.E. Zhukov, A.R. Kovsh, S.S. Mikhrin, N.A. Maleev, B.V. Volovik, Y.G. Musikhin, Y.M. Shernyakov, E.Y. Kondat'eva, M.V. Maximov, A.F. Tsatsul'nikov, N.N. Ledentsov, Z.I. Alferov, J.A. Lott, and D. Bimberg, *Long-wavelength quantum dot lasers on GaAs substrates.* Nanotechnology, 2000. **11**(4): p. 397-400.
46. Dabbousi, B.O., J. Rodriguez-Viejo, F.V. Mikulec, J.R. Heine, H. Mattoussi, R. Ober, K.F. Jensen, and M.G. Bawendi, *(CdSe)ZnS Core-Shell Quantum Dots: Synthesis and Characterization of a Size Series of Highly Luminescent Nanocrystallites.* J. Phys. Chem. B, 1997. **101**(46): p. 9463-9475.
47. Hines, M.A. and P. Guyot-Sionnest, *Synthesis and Characterization of Strongly Luminescing ZnS-Capped CdSe Nanocrystals.* J. Phys. Chem., 1996. **100**(2): p. 468-471.
48. Medintz, I.L., H.T. Uyeda, E.R. Goldman, and H. Mattoussi, *Quantum dot bioconjugates for imaging, labelling and sensing.* Nat Mater, 2005. **4**(6): p. 435-46.
49. Biju, V., D. Muraleedharan, K.i. Nakayama, Y. Shinohara, T. Itoh, Y. Baba, and M. Ishikawa, *Quantum dot-Insect Neuropeptide Conjugates for Fluorescence Imaging, Transfection, and Nucleus Targeting of Living Cells.* Langmuir, 2007. **23**(20): p. 10254-10261.
50. Marin, S. and A. Merkoci, *Direct electrochemical stripping detection of cystic-fibrosis-related DNA linked through cadmium sulfide quantum dots.* Nanotechnology, 2009. **20**(5).

51. Li, R., C.M. Li, H.F. Bao, and Q.L. Bao, *Stationary current generated from photocycle of a hybrid bacteriorhodopsin/quantum dots bionanosystem.* Appl. Phys. Lett., 2007. **91**: p. 223901.
52. Stavis, S.M., J.B. Edel, K.T. Samiee, and H.G. Craighead, *Single molecule studies of quantum dot conjugates in a submicrometer fluidic channel.* Lab Chip, 2005. **5**(3): p. 337-343.
53. Voura, E.B., J.K. Jaiswal, H. Mattoussi, and S.M. Simon, *Tracking metastatic tumor cell extravasation with quantum dot nanocrystals and fluorescence emission-scanning microscopy.* Nature Medicine, 2004. **10**(9): p. 993-998.
54. Sondi, I. and B. Salopek-Sondi, *Silver nanoparticles as antimicrobial agent: a case study on E. coli as a model for Gram-negative bacteria.* J. Colloid Interface Sci., 2004. **275**(1): p. 177-82.
55. Panacek, A., L. Kvitek, R. Prucek, M. Kolar, R. Vecerova, N. Pizurova, V.K. Sharma, T. Nevecna, and R. Zboril, *Silver colloid nanoparticles: Synthesis, characterization, and their antibacterial activity.* Journal of Physical Chemistry B, 2006. **110**(33): p. 16248-16253.
56. Lyon, D.Y., L.K. Adams, J.C. Falkner, and P.J. Alvarezt, *Antibacterial activity of fullerene water suspensions: effects of preparation method and particle size.* Environ Sci Technol, 2006. **40**(14): p. 4360-6.
57. Kim, Y.H., D.K. Lee, H.G. Cha, C.W. Kim, Y.C. Kang, and Y.S. Kang, *Preparation and characterization of the antibacterial Cu nanoparticle formed on the surface of SiO2 nanoparticles.* Journal of Physical Chemistry B, 2006. **110**(49): p. 24923-24928.
58. Adams, L.K., D.Y. Lyon, and P.J. Alvarez, *Comparative eco-toxicity of nanoscale TiO2, SiO2, and ZnO water suspensions.* Water Res, 2006. **40**(19): p. 3527-32.
59. Li, P., J. Li, C.Z. Wu, Q.S. Wu, and J. Li, *Synergistic antibacterial effects of beta-lactam antibiotic combined with silver nanoparticles.* Nanotechnology, 2005. **16**(9): p. 1912-1917.
60. Lok, C.N., C.M. Ho, R. Chen, Q.Y. He, W.Y. Yu, H. Sun, P.K.H. Tam, J.F. Chiu, and C.M. Che, *Silver nanoparticles: partial oxidation and antibacterial activities.* Journal of Biological Inorganic Chemistry, 2007. **12**(4): p. 527-534.
61. Hajkova, P., P.S. Patenka, J. Horsky, I. Horska, and A. Kolouch, *Antiviral and antibacterial effect of photocatalytic TiO2 films.* Tissue Engineering, 2007. **13**(4): p. 908-908.
62. Wei, C., W.Y. Lin, Z. Zainal, N.E. Williams, K. Zhu, A.P. Kruzic, R.L. Smith, and K. Rajeshwar, *Bactericidal Activity of Tio2 Photocatalyst in Aqueous-Media - toward a Solar-Assisted Water Disinfection System.* Environmental Science & Technology, 1994. **28**(5): p. 934-938.
63. Ipe, B.I., M. Lehnig, and C.M. Niemeyer, *On the generation of free radical species from quantum dots.* Small, 2005. **1**(7): p. 706-9.
64. Chalmers, N.I., R.J. Palmer, L. Du-Thumm, R. Sullivan, W.Y. Shi, and P.E. Kolenbrander, *Use of quantum dot luminescent probes to achieve single-cell resolution of human oral bacteria in biofilms.* Applied and Environmental Microbiology, 2007. **73**(2): p. 630-636.
65. Edgar, R., M. McKinstry, J. Hwang, A.B. Oppenheim, R.A. Fekete, G. Giulian, C. Merril, K. Nagashima, and S. Adhya, *High-sensitivity bacterial detection using biotin-tagged phage and quantum-dot nanocomplexes.* Proceedings of the National Academy of Sciences of the United States of America, 2006. **103**(13): p. 4841-4845.
66. Hirschey, M.D., Y.J. Han, G.D. Stucky, and A. Butler, *Imaging Escherichia coli using functionalized core/shell CdSe/CdS quantum dots.* Journal of Biological Inorganic Chemistry, 2006. **11**(5): p. 663-669.
67. Erogbogbo, F., K.T. Yong, I. Roy, G.X. Xu, P.N. Prasad, and M.T. Swihart, *Biocompatible*

luminescent silicon quantum dots for imaging of cancer cells. Acs Nano, 2008. **2**(5): p. 873-878.

68. Li, H., W.Y. Shih, and W.H. Shih, *Stable aqueous ZnS quantum dots obtained using (3-mercaptopropyl) trimethoxysilane as a capping molecule.* Nanotechnology, 2007. **18**(49).
69. Pradhan, N., D.M. Battaglia, Y.C. Liu, and X.G. Peng, *Efficient, stable, small, and water-soluble doped ZnSe nanocrystal emitters as non-cadmium biomedical labels.* Nano Letters, 2007. **7**(2): p. 312-317.
70. Hezinger, A.F.E., J. Tessmar, and A. Gopferich, *Polymer coating of quantum dots - A powerful tool toward diagnostics and sensorics.* European Journal of Pharmaceutics and Biopharmaceutics, 2008. **68**(1): p. 138-152.
71. Kirchner, C., T. Liedl, S. Kudera, T. Pellegrino, A.M. Javier, H.E. Gaub, S. Stolzle, N. Fertig, and W.J. Parak, *Cytotoxicity of colloidal CdSe and CdSe/ZnS nanoparticles.* Nano Letters, 2005. **5**(2): p. 331-338.
72. Duan, H.W. and S.M. Nie, *Cell-penetrating quantum dots based on multivalent and endosome-disrupting surface coatings.* Journal of the American Chemical Society, 2007. **129**(11): p. 3333-3338.
73. Bucking, W., S. Massadeh, A. Merkulov, S. Xu, and T. Nann, *Electrophoretic properties of BSA-coated quantum dots.* Analytical and Bioanalytical Chemistry, 2010. **396**(3): p. 1087-1094.
74. Wang, Q., Y.C. Kuo, Y.W. Wang, G. Shin, C. Ruengruglikit, and Q.R. Huang, *Luminescent properties of water-soluble denatured bovine serum albumin-coated CdTe quantum dots.* Journal of Physical Chemistry B, 2006. **110**(34): p. 16860-16866.
75. Byrne, S.J., Y. Williams, A. Davies, S.A. Corr, A. Rakovich, Y.K. Gun'ko, Y.R. Rakovich, J.F. Donegan, and Y. Volkov, *"Jelly dots": Synthesis and cytotoxicity studies of CdTe quantum dot-gelatin nanocomposites.* Small, 2007. **3**(7): p. 1152-1156.
76. Wolcott, A., D. Gerion, M. Visconte, J. Sun, A. Schwartzberg, S.W. Chen, and J.Z. Zhang, *Silica-coated CdTe quantum dots functionalized with thiols for bioconjugation to IgG proteins.* Journal of Physical Chemistry B, 2006. **110**(11): p. 5779-5789.
77. Correa-Duarte, M.A., M. Giersig, and L.M. Liz-Marzan, *Stabilization of CdS semiconductor nanoparticles against photodegradation by a silica coating procedure.* Chemical Physics Letters, 1998. **286**(5-6): p. 497-501.
78. Rogach, A.L., D. Nagesha, J.W. Ostrander, M. Giersig, and N.A. Kotov, *"Raisin bun"-type composite spheres of silica and semiconductor nanocrystals.* Chemistry of Materials, 2000. **12**(9): p. 2676-2685.
79. Yang, Y.H., L.H. Jing, X.L. Yu, D.D. Yan, and M.Y. Gao, *Coating aqueous quantum dots with silica via reverse microemulsion method: Toward size-controllable and robust fluorescent nanoparticles.* Chemistry of Materials, 2007. **19**(17): p. 4123-4128.
80. Bakalova, R., Z. Zhelev, I. Aoki, H. Ohba, Y. Imai, and I. Kanno, *Silica-shelled single quantum dot micelles as imaging probes with dual or multimodality.* Analytical Chemistry, 2006. **78**(16): p. 5925-5932.
81. Sun, Y., F. Masia, W. Langbein, and P. Borri, *Fabrication and optical properties of thin silica-coated CdSe/ZnS quantum dots.* Physica Status Solidi a-Applications and Materials Science, 2009. **206**(12): p. 2822-2825.
82. Qian, L., D. Bera, T.K. Tseng, and P.H. Holloway, *High efficiency photoluminescence from silica-coated CdSe quantum dots.* Applied Physics Letters, 2009. **94**(7).

83. Hendrikse, N.H., G. Luurtsema, A.A. van der Veldt, and M. Lubberink, *Positron emission tomography for modeling pathophysiological processes in vivo.* Current Opinion in Drug Discovery & Development, 2008. **11**(5): p. 717-725.
84. Long, C.M. and J.W.M. Bulte, *In vivo tracking of cellular therapeutics using magnetic resonance imaging.* Expert Opinion on Biological Therapy, 2009. **9**(3): p. 293-306.
85. Modo, M., T.J. Roberts, J.K. Sandhu, and S.C.R. Williams, *In vivo monitoring of cellular transplants by magnetic resonance imaging and positron emission tomography.* Expert Opinion on Biological Therapy, 2004. **4**(2): p. 145-155.
86. Natt, O. and J. Frahm, *In vivo magnetic resonance imaging: insights into structure and function of the central nervous system.* Measurement Science & Technology, 2005. **16**(4): p. R17-R36.
87. Wittendorprechenmann, E. and M. Thellier, *SPECIFIC METHODS FOR THE IMAGING OF RADIOACTIVE-TRACERS.* Plant Physiology and Biochemistry, 1993. **31**(4): p. 609-619.
88. Jennings, L.E. and N.J. Long, *'Two is better than one'--probes for dual-modality molecular imaging.* Chem Commun (Camb), 2009(24): p. 3511-24.
89. Yang, H., S. Santra, G.A. Walter, and P.H. Holloway, *Gd^{III}-Functionalized Fluorescent Quantum Dots as Multimodal Imaging Probes.* Advanced Materials, 2006. **18**: p. 2890-2894.
90. van Tilborg, G.A., W.J. Mulder, P.T. Chin, G. Storm, C.P. Reutelingsperger, K. Nicolay, and G.J. Strijkers, *Annexin A5-conjugated quantum dots with a paramagnetic lipidic coating for the multimodal detection of apoptotic cells.* Bioconjug Chem, 2006. **17**(4): p. 865-8.
91. Mulder, W.J., K. Castermans, J.R. van Beijnum, M.G. Oude Egbrink, P.T. Chin, Z.A. Fayad, C.W. Lowik, E.L. Kaijzel, I. Que, G. Storm, G.J. Strijkers, A.W. Griffioen, and K. Nicolay, *Molecular imaging of tumor angiogenesis using alphavbeta3-integrin targeted multimodal quantum dots.* Angiogenesis, 2009. **12**(1): p. 17-24.
92. Mulder, W.J., G.J. Strijkers, K. Nicolay, and A.W. Griffioen, *Quantum dots for multimodal molecular imaging of angiogenesis.* Angiogenesis, 2010. **13**(2): p. 131-4.
93. Earhart, C., N.R. Jana, N. Erathodiyil, and J.Y. Ying, *Synthesis of carbohydrate-conjugated nanoparticles and quantum dots.* Langmuir, 2008. **24**(12): p. 6215-6219.
94. Yi, D.K., S.T. Selvan, S.S. Lee, G.C. Papaefthymiou, D. Kundaliya, and J.Y. Ying, *Silica-coated nanocomposites of magnetic nanoparticles and quantum dots.* Journal of the American Chemical Society, 2005. **127**(14): p. 4990-4991.
95. Ang, C.Y., L. Giam, Z.M. Chan, A.W.H. Lin, H. Gu, E. Devlin, G.C. Papoefthymiou, S.T. Selvan, and J.Y. Ying, *Facile Synthesis of Fe2O3 Nanocrystals without Fe(CO)(5) Precursor and One-Pot Synthesis of Highly Fluorescent Fe2O3-CdSe Nanocomposites.* Advanced Materials, 2009. **21**(8): p. 869-+.
96. Cai, W., K. Chen, Z.B. Li, S.S. Gambhir, and X. Chen, *Dual-function probe for PET and near-infrared fluorescence imaging of tumor vasculature.* J Nucl Med, 2007. **48**(11): p. 1862-70.
97. Schipper, M.L., Z. Cheng, S.W. Lee, L.A. Bentolila, G. Iyer, J. Rao, X. Chen, A.M. Wu, S. Weiss, and S.S. Gambhir, *microPET-based biodistribution of quantum dots in living mice.* J Nucl Med, 2007. **48**(9): p. 1511-8.
98. Zrazhevskiy, P. and X.H. Gao, *Multifunctional quantum dots for personalized medicine.* Nano Today, 2009. **4**(5): p. 414-428.
99. Kim, J., J.E. Lee, S.H. Lee, J.H. Yu, J.H. Lee, T.G. Park, and T. Hyeon, *Designed fabrication of a multifunctional polymer nanomedical platform for simultaneous cancer-targeted imaging and*

magnetically guided drug delivery. Advanced Materials, 2008. **20**(3): p. 478-+.

100. Yuan, Q., S. Hein, and R.D.K. Misra, *New generation of chitosan-encapsulated ZnO quantum dots loaded with drug: Synthesis, characterization and in vitro drug delivery response.* Acta Biomaterialia, 2010. **6**(7): p. 2732-2739.
101. Wu, W.T., M. Aiello, T. Zhou, A. Berliner, P. Banerjee, and S.Q. Zhou, *In-situ immobilization of quantum dots in polysaccharide-based nanogels for integration of optical pH-sensing, tumor cell imaging, and drug delivery.* Biomaterials, 2010. **31**(11): p. 3023-3031.
102. Bagalkot, V., L. Zhang, E. Levy-Nissenbaum, S. Jon, P.W. Kantoff, R. Langer, and O.C. Farokhzad, *Quantum dot - Aptamer conjugates for synchronous cancer imaging, therapy, and sensing of drug delivery based on Bi-fluorescence resonance energy transfer.* Nano Letters, 2007. **7**(10): p. 3065-3070.
103. Yang, Y.J., X. Tao, Q. Hou, and J.F. Chen, *Fluorescent mesoporous silica nanotubes incorporating CdS quantum dots for controlled release of ibuprofen.* Acta Biomaterialia, 2009. **5**(9): p. 3488-3496.
104. Guo, Y., D.L. Shi, H.S. Cho, Z.Y. Dong, A. Kulkarni, G.M. Pauletti, W. Wang, J. Lian, W. Liu, L. Ren, Q.Q. Zhang, G.K. Liu, C. Huth, L.M. Wang, and R.C. Ewing, *In vivo imaging and drug storage by quantum-dot-conjugated carbon nanotubes.* Advanced Functional Materials, 2008. **18**(17): p. 2489-2497.
105. Hu, S.H., K.T. Kuo, W.L. Tung, D.M. Liu, and S.Y. Chen, *A Multifunctional Nanodevice Capable of Imaging, Magnetically Controlling, and In Situ Monitoring Drug Release.* Advanced Functional Materials, 2009. **19**(21): p. 3396-3403.
106. Xu, Y., A. Karmakar, D.Y. Wang, M.W. Mahmood, F. Watanabe, Y.B. Zhang, A. Fejleh, P. Fejleh, Z.R. Li, G. Kannarpady, S. Ali, A.R. Biris, and A.S. Biris, *Multifunctional Fe3O4 Cored Magnetic-Quantum Dot Fluorescent Nanocomposites for RF Nanohyperthermia of Cancer Cells.* Journal of Physical Chemistry C, 2010. **114**(11): p. 5020-5026.
107. Cho, H.S., Z.Y. Dong, G.M. Pauletti, J.M. Zhang, H. Xu, H.C. Gu, L.M. Wang, R.C. Ewing, C. Huth, F. Wang, and D.L. Shi, *Fluorescent, Superparamagnetic Nanospheres for Drug Storage, Targeting, and Imaging: A Multifunctional Nanocarrier System for Cancer Diagnosis and Treatment.* ACS Nano, 2010. **4**(9): p. 5398-5404.
108. Shi, D.L., H.S. Cho, Y. Chen, H. Xu, H.C. Gu, J. Lian, W. Wang, G.K. Liu, C. Huth, L.M. Wang, R.C. Ewing, S. Budko, G.M. Pauletti, and Z.Y. Dong, *Fluorescent Polystyrene-Fe3O4 Composite Nanospheres for In Vivo Imaging and Hyperthermia.* Advanced Materials, 2009. **21**(21): p. 2170-+.
109. Samia, A.C.S., X.B. Chen, and C. Burda, *Semiconductor quantum dots for photodynamic therapy.* Journal of the American Chemical Society, 2003. **125**(51): p. 15736-15737.
110. Shi, L.X., B. Hernandez, and M. Selke, *Singlet oxygen generation from water-soluble quantum dot-organic dye nanocomposites.* Journal of the American Chemical Society, 2006. **128**(19): p. 6278-6279.
111. Ma, J., J.Y. Chen, M. Idowu, and T. Nyokong, *Generation of singlet oxygen via the composites of water-soluble thiol-capped CdTe quantum dots - Sulfonated aluminum phthalocyanines.* Journal of Physical Chemistry B, 2008. **112**(15): p. 4465-4469.
112. Idowu, M., J.Y. Chen, and T. Nyokong, *Photoinduced energy transfer between water-soluble CdTe quantum dots and aluminium tetrasulfonated phthalocyanine.* New Journal of Chemistry,

2008. **32**(2): p. 290-296.

113. Bakalova, R., H. Ohba, Z. Zhelev, M. Ishikawa, and Y. Baba, *Quantum dots as photosensitizers?* Nature Biotechnology, 2004. **22**(11): p. 1360-1361.
114. Samia, A.C.S., S. Dayal, and C. Burda, *Quantum dot-based energy transfer: Perspectives and potential for applications in photodynamic therapy.* Photochemistry and Photobiology, 2006. **82**(3): p. 617-625.
115. Cady, N.C., A.D. Strickland, and C.A. Batt, *Optimized linkage and quenching strategies for quantum dot molecular beacons.* Molecular and Cellular Probes, 2007. **21**(2): p. 116-124.
116. Suzuki, M., Y. Husimi, H. Komatsu, K. Suzuki, and K.T. Douglas, *Quantum dot FRET Biosensors that respond to pH, to proteolytic or nucleolytic cleavage, to DNA synthesis, or to a multiplexing combination.* Journal of the American Chemical Society, 2008. **130**(17): p. 5720-5725.
117. Zhao, D., W.H. Chan, Z.K. He, and T. Qiu, *Quantum Dot-Ruthenium Complex Dyads: Recognition of Double-Strand DNA through Dual-Color Fluorescence Detection.* Analytical Chemistry, 2009. **81**(9): p. 3537-3543.
118. Guo, C.X., H.B. Yang, Z.M. Sheng, Z.S. Lu, Q.L. Song, and C.M. Li, *Layered Graphene/Quantum Dots for Photovoltaic Devices.* Angewandte Chemie-International Edition, 2010. **49**(17): p. 3014-3017.
119. Bang, J.H. and P.V. Kamat, *Quantum Dot Sensitized Solar Cells. A Tale of Two Semiconductor Nanocrystals: CdSe and CdTe.* Acs Nano, 2009. **3**(6): p. 1467-1476.
120. Cao, A.N., Z. Liu, S.S. Chu, M.H. Wu, Z.M. Ye, Z.W. Cai, Y.L. Chang, S.F. Wang, Q.H. Gong, and Y.F. Liu, *A Facile One-step Method to Produce Graphene-CdS Quantum Dot Nanocomposites as Promising Optoelectronic Materials.* Advanced Materials, 2010. **22**(1): p. 103-+.
121. Chang, H.X., X.J. Lv, H. Zhang, and J.H. Li, *Quantum dots sensitized graphene: In situ growth and application in photoelectrochemical cells* Electrochemistry Communications, 2010. **12**(3): p. 483-487.
122. Gao, X.F., H.B. Li, W.T. Sun, Q. Chen, F.Q. Tang, and L.M. Peng, *CdTe Quantum Dots-Sensitized TiO2 Nanotube Array Photoelectrodes.* Journal of Physical Chemistry C, 2009. **113**(18): p. 7531-7535.
123. Kamat, P.V., *Quantum Dot Solar Cells. Semiconductor Nanocrystals as Light Harvesters.* Journal of Physical Chemistry C, 2008. **112**(48): p. 18737-18753.
124. Lu, Z., C.X. Guo, H.B. Yang, Y. Qiao, J. Guo, and C.M. Li, *One-step aqueous synthesis of graphene-CdTe quantum dot-composed nanosheet and its enhanced photoresponses.* Journal of Colloid and Interface Science, 2010. **DOI: 10.1016/j.jcis.2010.10.007**.
125. Tang, L.H., Y.H. Zhu, X.L. Yang, J.J. Sun, and C.Z. Li, *Self-assembled CNTs/CdS/dehydrogenase hybrid-based amperometric biosensor triggered by photovoltaic effect.* Biosensors & Bioelectronics, 2008. **24**(2): p. 319-323.
126. Wang, G.L., J.J. Xu, H.Y. Chen, and S.Z. Fu, *Label-free photoelectrochemical immunoassay for alpha-fetoprotein detection based on TiO2/CdS hybrid.* Biosensors & Bioelectronics, 2009. **25**(4): p. 791-796.
127. Qian, Z., H.J. Bai, G.L. Wang, J.J. Xu, and H.Y. Chen, *A photoelectrochemical sensor based on CdS-polyamidoamine nano-composite film for cell capture and detection.* Biosensors &

Bioelectronics, 2010. **25**(9): p. 2045-2050.

128. Xu, H.X., M.Y. Sha, E.Y. Wong, J. Uphoff, Y.H. Xu, J.A. Treadway, A. Truong, E. O'Brien, S. Asquith, M. Stubbins, N.K. Spurr, E.H. Lai, and W. Mahoney, *Multiplexed SNP genotyping using the Qbead (TM) system: a quantum dot-encoded microsphere-based assay.* Nucleic Acids Research, 2003. **31**(8).
129. Rauf, S., A. Glidle, and J.M. Cooper, *Application of quantum dot barcodes prepared using biological self-assembly to multiplexed immunoassays.* Chemical Communications, 2010. **46**(16): p. 2814-2816.
130. Li, J., X.W. Zhao, Y.J. Zhao, and Z.Z. Gu, *Quantum-dot-coated encoded silica colloidal crystals beads for multiplex coding.* Chemical Communications, 2009(17): p. 2329-2331.
131. Li, R., C.M. Li, H.F. Bao, Q.L. Bao, and V.S. Lee, *Stationary current generated from photocycle of a hybrid bacteriorhodopsin/quantum dot bionanosystem.* Applied Physics Letters, 2007. **91**(22).
132. Guo, C.X., Z.S. Lu, Y. Lei, and C.M. Li, *Ionic liquid-graphene composite for ultratrace explosive trinitrotoluene detection.* Electrochemistry Communications, 2010. **12**(9): p. 1237-1240.
133. Wang, M. and C.M. Li, *Magnetism in graphene oxide.* New Journal of Physics, 2010. **12**.
134. Yang, K., S.A. Zhang, G.X. Zhang, X.M. Sun, S.T. Lee, and Z.A. Liu, *Graphene in Mice: Ultrahigh In Vivo Tumor Uptake and Efficient Photothermal Therapy.* Nano Letters, 2010. **10**(9): p. 3318-3323.
135. Yang, X.Y., X.Y. Zhang, Y.F. Ma, Y. Huang, Y.S. Wang, and Y.S. Chen, *Superparamagnetic graphene oxide-Fe3O4 nanoparticles hybrid for controlled targeted drug carriers.* Journal of Materials Chemistry, 2009. **19**(18): p. 2710-2714.
136. Zhang, L.M., J.G. Xia, Q.H. Zhao, L.W. Liu, and Z.J. Zhang, *Functional Graphene Oxide as a Nanocarrier for Controlled Loading and Targeted Delivery of Mixed Anticancer Drugs.* Small, 2010. **6**(4): p. 537-544.
137. Bao, H.F., E.K. Wang, and S.J. Dong, *One-pot synthesis of CdTe nanocrystals and shape control of luminescent CdTe-cystine nanocomposites.* Small, 2006. **2**(4): p. 476-480.
138. Attar, F., E. Keyhani, and J. Keyhani, *A comparative study of superoxide dismutase activity assays in Crocus sativus L. corms.* Appl. Biochem. Micro., 2006. **42**(1): p. 101-106.
139. Oliver, C.N., P.E. Starke-Reed, E.R. Stadtman, G.J. Liu, J.M. Carney, and R.A. Floyd, *Oxidative damage to brain proteins, loss of glutamine synthetase activity, and production of free radicals during ischemia/reperfusion-induced injury to gerbil brain.* Proceedings of the National Academy of Sciences of the United States of America, 1990. **87**(13): p. 5144-7.
140. Yousef, M.I., T.I. Awad, F.A. Elhag, and F.A. Khaled, *Study of the protective effect of ascorbic acid against the toxicity of stannous chloride on oxidative damage, antioxidant enzymes and biochemical parameters in rabbits.* Toxicology, 2007. **235**(3): p. 194-202.
141. Pereira, R.D. and J. Geibel, *Direct observation of oxidative stress on the cell wall of Saccharomyces cerevisiae strains with atomic force microscopy.* Molecular and Cellular Biochemistry, 1999. **201**(1-2): p. 17-24.
142. Boldt, K., O.T. Bruns, N. Gaponik, and A. Eychmuller, *Comparative examination of the stability of semiconductor quantum dots in various biochemical buffers.* Journal of Physical Chemistry B, 2006. **110**(5): p. 1959-1963.

143. Bakalova, R., H. Ohba, Z. Zhelev, M. Ishikawa, and Y. Baba, *Quantum dots as photosensitizers?* Nat. Biotechnol., 2004. **22**(11): p. 1360-1361.
144. Bakalova, R., H. Ohba, Z. Zhelev, T. Nagase, R. Jose, M. Ishikawa, and Y. Baba, *Quantum dot anti-CD conjugates: Are they potential photosensitizers or potentiators of classical photosensitizing agents in photodynamic therapy of cancer?* Nano. Lett., 2004. **4**(9): p. 1567-1573.
145. Green, M. and E. Howman, *Semiconductor quantum dots and free radical induced DNA nicking.* Chemical Communications, 2005(1): p. 121-123.
146. Kukreja, R.C., R.L. Jesse, and M.L. Hess, *Singlet oxygen: a potential culprit in myocardial injury?* Molecular and Cellular Biochemistry, 1992. **111**(1-2): p. 17-24.
147. Oren, D.A., D.S. Charney, R. Lavie, M. Sinyakov, and R. Lubart, *Stimulation of reactive oxygen species production by an antidepressant visible light source.* Biological Psychiatry, 2001. **49**(5): p. 464-467.
148. Gubbins, K.E. and R.D. Walker, *The solubility and diffusivity of oxygen in electrolytic solutions.* J. Electrochem. Soc., 1965. **112**: p. 469-471.
149. Anuntalabhochai, S., R. Chandej, B. Phanchaisri, L.D. Yu, T. Vilaithong, and I.G. Brown, *Ion-beam-induced deoxyribose nucleic acid transfer.* Appl. Phys. Lett., 2001. **78**: p. 2393-2395.
150. Kumara, M.T., B.C. Tripp, and S. Muralidharan, *Exciton energy transfer in self-assembled quantum dots on bioengineered bacterial flagella nanotubes.* Journal of Physical Chemistry C, 2007. **111**(14): p. 5276-5280.
151. Sweeney, R.Y., C.B. Mao, X.X. Gao, J.L. Burt, A.M. Belcher, G. Georgiou, and B.L. Iverson, *Bacterial biosynthesis of cadmium sulfide nanocrystals.* Chemistry & Biology, 2004. **11**(11): p. 1553-1559.
152. Lovric, J., H.S. Bazzi, Y. Cuie, G.R. Fortin, F.M. Winnik, and D. Maysinger, *Differences in subcellular distribution and toxicity of green and red emitting CdTe quantum dots.* J Mol Med, 2005. **83**(5): p. 377-85.
153. Lovric, J., S.J. Cho, F.M. Winnik, and D. Maysinger, *Unmodified cadmium telluride quantum dots induce reactive oxygen species formation leading to multiple organelle damage and cell death.* Chemistry & Biology, 2005. **12**(11): p. 1227-34.
154. Dikalov, S., K.K. Griendling, and D.G. Harrison, *Measurement of reactive oxygen species in cardiovascular studies.* Hypertension, 2007. **49**(4): p. 717-27.
155. Chen, F.Q. and D. Gerion, *Fluorescent CdSe/ZnS nanocrystal-peptide conjugates for long-term, nontoxic imaging and nuclear targeting in living cells.* Nano. Lett., 2004. **4**(10): p. 1827-1832.
156. Dwyer, D.J., M.A. Kohanski, B. Hayete, and J.J. Collins, *Gyrase inhibitors induce an oxidative damage cellular death pathway in Escherichia coli.* Mol. Syst. Biol. , 2007. **3**: p. 91.
157. Kohanski, M.A., D.J. Dwyer, B. Hayete, C.A. Lawrence, and J.J. Collins, *A common mechanism of cellular death induced by bactericidal antibiotics.* Cell, 2007. **130**(5): p. 797-810.
158. Close, G.L., T. Ashton, A. McArdle, and M.J. Jackson, *Microdialysis studies of extracellular reactive oxygen species in skeletal muscle: factors influencing the reduction of cytochrome c and hydroxylation of salicylate.* Free Radic. Biol. Med., 2005. **39**(11): p. 1460-7.
159. Reddy, K.M., K. Feris, J. Bell, D.G. Wingett, C. Hanley, and A. Punnoose, *Selective toxicity of zinc oxide nanoparticles to prokaryotic and eukaryotic systems.* Appl. Phys. Lett., 2007. **90**(213902): p. 2139021-2139023.

160. Clarke, S.J., C.A. Hollmann, F.A. Aldaye, and J.L. Nadeau, *Effect of ligand density on the spectral, physical, and biological characteristics of CdSe/ZnS quantum dots.* Bioconjugate Chemistry, 2008. **19**(2): p. 562-568.
161. Samia, A.C., S. Dayal, and C. Burda, *Quantum dot-based energy transfer: perspectives and potential for applications in photodynamic therapy.* Photochem. Photobiol., 2006. **82**(3): p. 617-25.
162. Li, H., W.Y. Shih, and W.H. Shih, *Non-heavy-metal ZnS quantum dots with bright blue photoluminescence by a one-step aqueous synthesis.* Nanotechnology, 2007. **18**(20).
163. Moussodia, R.O., L. Balan, and R. Schneider, *Synthesis and characterization of water-soluble ZnO quantum dots prepared through PEG-siloxane coating.* New Journal of Chemistry, 2008. **32**(8): p. 1388-1393.
164. Krishna, M.G., K.N. Rao, and S. Mohan, *STRUCTURAL AND OPTICAL-PROPERTIES OF ZIRCONIA THIN-FILMS.* Thin Solid Films, 1990. **193**(1-2): p. 690-695.
165. Liu, X.Y., A.P. Huang, C.X. Ding, and P.K. Chu, *Bioactivity and cytocompatibility of zirconia (ZrO2) films fabricated by cathodic arc deposition.* Biomaterials, 2006. **27**(21): p. 3904-3911.
166. Yamasaki, M., Y. Hagiwara, T. Nagai, Y. Kawamoto, and T. Igarashi, *Effects of surface treatments on resin bond strength to zirconia ceramic abutment.* Journal of Dental Research, 2003. **82**: p. 2614.
167. Liu, S.Q., J.J. Xu, and H.Y. Chen, *ZrO2 gel-derived DNA-modified electrode and the effect of lanthanide on its electron transfer behavior.* Bioelectrochemistry, 2002. **57**(2): p. 149-154.
168. Zhu, N.N., A.P. Zhang, Q.J. Wang, P.G. He, and Y.Z. Fang, *Electrochemical detection of DNA hybridization using methylene blue and electro-deposited zirconia thin films on gold electrodes.* Analytica Chimica Acta, 2004. **510**(2): p. 163-168.
169. Lo, C.Y., W.Y. Chen, C.T. Chen, and Y.C. Chen, *Rapid enrichment of phosphopeptides from tryptic digests of proteins using iron oxide nanocomposites of magnetic particles coated with zirconia as the concentrating probes.* Journal of Proteome Research, 2007. **6**(2): p. 887-893.
170. Liu, Y.S., C.M. Li, W.H. Hu, and Z.S. Lu, *High performance protein microarrays based on glycidyl methacrylate-modified polyethylene terephthalate plastic substrate.* Talanta, 2009. **77**(3): p. 1165-1171.
171. Yu, L., Y.S. Liu, Y. Gan, and C.M. Li, *High-performance UV-curable epoxy resin-based microarray and microfluidic immunoassay devices.* Biosensors & Bioelectronics, 2009. **24**(10): p. 2997-3002.
172. Wang, C., Q. Ma, W.C. Dou, S. Kanwal, G.N. Wang, P.F. Yuan, and X.G. Su, *Synthesis of aqueous CdTe quantum dots embedded silica nanoparticles and their applications as fluorescence probes.* Talanta, 2009. **77**(4): p. 1358-1364.
173. Yu, W.W., L.H. Qu, W.Z. Guo, and X.G. Peng, *Experimental determination of the extinction coefficient of CdTe, CdSe, and CdS nanocrystals.* Chem. Mater., 2003. **15**(14): p. 2854-2860.
174. Yang, H.S., P.H. Holloway, and S. Santra, *Water-soluble silica-overcoated CdS : Mn/ZnS semiconductor quantum dots.* Journal of Chemical Physics, 2004. **121**(15): p. 7421-7426.
175. Tan, T.T., S.T. Selvan, L. Zhao, S.J. Gao, and J.Y. Ying, *Size control, shape evolution, and silica coating of near-infrared-emitting PbSe quantum dots.* Chemistry of Materials, 2007. **19**(13): p. 3112-3117.
176. Holm, J., S.I. Hansen, M. Hoier-Madsen, L. Korsbaek, H. Beckmann, and K. Josefsen, *Ligand*

binding characteristics of a glycosylphosphatidyl inositol membrane-anchored HeLa cell folate receptor epitope-related to human milk folate binding protein. Bioscience Reports, 2000. **20**(2): p. 109-118.

177. Manna, L., E.C. Scher, and A.P. Alivisatos, *Shape control of colloidal semiconductor nanocrystals.* Journal of Cluster Science, 2002. **13**(4): p. 521-532.
178. Talapin, D.V., S. Haubold, A.L. Rogach, A. Kornowski, M. Haase, and H. Weller, *A novel organometallic synthesis of highly luminescent CdTe nanocrystals.* Journal of Physical Chemistry B, 2001. **105**(12): p. 2260-2263.
179. Bao, H.F., X.Q. Cui, C.M. Li, and J.F. Zang, *Shape-controlled assembly of luminescent dumbbell-like CdTe-cystine nanocomposites.* Nanotechnology, 2007. **18**(45).
180. Rogach, A.L., L. Katsikas, A. Kornowski, D.S. Su, A. Eychmuller, and H. Weller, *Synthesis and characterization of thiol-stabilized CdTe nanocrystals.* Berichte Der Bunsen-Gesellschaft-Physical Chemistry Chemical Physics, 1996. **100**(11): p. 1772-1778.
181. Zhang, H., L.P. Wang, H.M. Xiong, L.H. Hu, B. Yang, and W. Li, *Hydrothermal synthesis for high-quality CdTe nanocrystals.* Advanced Materials, 2003. **15**(20): p. 1712-1715.
182. Dahl, J.A., B.L.S. Maddux, and J.E. Hutchison, *Toward greener nanosynthesis.* Chemical Reviews, 2007. **107**(6): p. 2228-2269.
183. Bai, H.J., Z.M. Zhang, and J. Gong, *Biological synthesis of semiconductor zinc sulfide nanoparticles by immobilized Rhodobacter sphaeroides.* Biotechnology Letters, 2006. **28**(14): p. 1135-1139.
184. Ahmad, A., P. Mukherjee, D. Mandal, S. Senapati, M.I. Khan, R. Kumar, and M. Sastry, *Enzyme mediated extracellular synthesis of CdS nanoparticles by the fungus, Fusarium oxysporum.* Journal of the American Chemical Society, 2002. **124**(41): p. 12108-12109.
185. Kowshik, M., N. Deshmukh, W. Vogel, J. Urban, S.K. Kulkarni, and K.M. Paknikar, *Microbial synthesis of semiconductor CdS nanoparticles, their characterization, and their use in the fabrication of an ideal diode.* Biotechnology and Bioengineering, 2002. **78**(5): p. 583-588.
186. Bai, H.J., Z.M. Zhang, Y. Guo, and G.E. Yang, *Biosynthesis of cadmium sulfide nanoparticles by photosynthetic bacteria Rhodopseudomonas palustris.* Colloids and Surfaces B-Biointerfaces, 2009. **70**(1): p. 142-146.
187. Kowshik, M., W. Vogel, J. Urban, S.K. Kulkarni, and K.M. Paknikar, *Microbial synthesis of semiconductor PbS nanocrystallites.* Advanced Materials, 2002. **14**(11): p. 815-818.
188. Cui, R., H.H. Liu, H.Y. Xie, Z.L. Zhang, Y.R. Yang, D.W. Pang, Z.X. Xie, B.B. Chen, B. Hu, and P. Shen, *Living Yeast Cells as a Controllable Biosynthesizer for Fluorescent Quantum Dots.* Advanced Functional Materials, 2009. **19**(15): p. 2359-2364.
189. Gaponik, N., D.V. Talapin, A.L. Rogach, K. Hoppe, E.V. Shevchenko, A. Kornowski, A. Eychmuller, and H. Weller, *Thiol-capping of CdTe nanocrystals: An alternative to organometallic synthetic routes.* Journal of Physical Chemistry B, 2002. **106**(29): p. 7177-7185.
190. Peng, Z.A. and X.G. Peng, *Formation of high-quality CdTe, CdSe, and CdS nanocrystals using CdO as precursor.* Journal of the American Chemical Society, 2001. **123**(1): p. 183-184.
191. Vogel, W., P.H. Borse, N. Deshmukh, and S.K. Kulkarni, *Structure and stability of monodisperse 1.4-nm ZnS particles stabilized by mercaptoethanol.* Langmuir, 2000. **16**: p. 2032-2037.
192. Singh, N., B. Manshian, G.J. Jenkins, S.M. Griffiths, P.M. Williams, T.G. Maffeis, C.J. Wright, and S.H. Doak, *NanoGenotoxicology: the DNA damaging potential of engineered*

nanomaterials. Biomaterials, 2009. **30**(23-24): p. 3891-914.
193. Su, Y., Y. He, H. Lu, L. Sai, Q. Li, W. Li, L. Wang, P. Shen, Q. Huang, and C. Fan, *The cytotoxicity of cadmium based, aqueous phase - synthesized, quantum dots and its modulation by surface coating.* Biomaterials, 2009. **30**(1): p. 19-25.
194. Ackerley, D.F., Y. Barak, S.V. Lynch, J. Curtin, and A. Matin, *Effect of chromate stress on Escherichia coli K-12.* Journal of Bacteriology, 2006. **188**(9): p. 3371-3381.
195. Glavee, G.N., K.J. Klabunde, C.M. Sorensen, and G.C. Hadjapanayis, *Borohydride reductions of metal Ions. A new understanding of the chemistry leading to nanoscale particles of metals, borides, and metal borates.* Langmuir, 1992. **8**(3): p. 771-773.
196. Kang, S.H., K.N. Bozhilov, N.V. Myung, A. Mulchandani, and W. Chen, *Microbial synthesis of CdS nanocrystals in genetically engineered E-coli.* Angewandte Chemie-International Edition, 2008. **47**(28): p. 5186-5189.
197. Qiao, Y., C.M. Li, S.J. Bao, Z.S. Lu, and Y.H. Hong, *Direct electrochemistry and electrocatalytic mechanism of evolved Escherichia coli cells in microbial fuel cells.* Chemical Communications, 2008(11): p. 1290-1292.
198. Riehle, M.M., A.F. Bennett, and A.D. Long, *Changes in gene expression following high-temperature adaptation in experimentally evolved populations of E-coli.* Physiological and Biochemical Zoology, 2005. **78**(3): p. 299-315.
199. Swanson, J.A., *Shaping cups into phagosomes and macropinosomes.* Nature Reviews Molecular Cell Biology, 2008. **9**(8): p. 639-49.
200. Mitragotri, S. and J. Lahann, *Physical approaches to biomaterial design.* Nature Materials, 2009. **8**(1): p. 15-23.
201. Champion, J.A., A. Walker, and S. Mitragotri, *Role of particle size in phagocytosis of polymeric microspheres.* Pharmaceutical Research, 2008. **25**(8): p. 1815-1821.
202. Pratten, M.K. and J.B. Lloyd, *PINOCYTOSIS AND PHAGOCYTOSIS - THE EFFECT OF SIZE OF A PARTICULATE SUBSTRATE ON ITS MODE OF CAPTURE BY RAT PERITONEAL-MACROPHAGES CULTURED INVITRO.* Biochimica Et Biophysica Acta, 1986. **881**(3): p. 307-313.
203. Tabata, Y. and Y. Ikada, *EFFECT OF THE SIZE AND SURFACE-CHARGE OF POLYMER MICROSPHERES ON THEIR PHAGOCYTOSIS BY MACROPHAGE.* Biomaterials, 1988. **9**(4): p. 356-362.
204. Champion, J.A., Y.K. Katare, and S. Mitragotri, *Particle shape: A new design parameter for micro- and nanoscale drug delivery carriers.* Journal of Controlled Release, 2007. **121**(1-2): p. 3-9.
205. Champion, J.A. and S. Mitragotri, *Role of target geometry in phagocytosis.* Proceedings of the National Academy of Sciences of the United States of America, 2006. **103**(13): p. 4930-4934.
206. He, Q., H. Mohwald, and J.B. Li, *Layer-by-Layer Assembled Nanotubes as Biomimetic Nanoreactors for Calcium Carbonate Deposition.* Macromolecular Rapid Communications, 2009. **30**(18): p. 1538-1542.
207. Hilder, T.A. and J.M. Hill, *Modeling the Loading and Unloading of Drugs into Nanotubes.* Small, 2009. **5**(3): p. 300-308.
208. Lim, Y.T., J.K. Kim, Y.W. Noh, M.Y. Cho, and B.H. Chung, *Multifunctional Silica Nanocapsule with a Single Surface Hole.* Small, 2009. **5**(3): p. 324-328.

209. Oh, J.M., S.J. Choi, G.E. Lee, S.H. Han, and J.H. Choy, *Inorganic Drug-Delivery Nanovehicle Conjugated with Cancer-Cell-Specific Ligand.* Advanced Functional Materials, 2009. **19**(10): p. 1617-1624.
210. Misra, R.D.K., *Quantum dots for tumor targeted drug delivery and cell imaging.* Nanomedicine, 2008. **3**: p. 271-274.
211. Gratton, S.E.A., P.A. Ropp, P.D. Pohlhaus, J.C. Luft, V.J. Madden, M.E. Napier, and J.M. DeSimone, *The effect of particle design on cellular internalization pathways.* Proceedings of the National Academy of Sciences of the United States of America, 2008. **105**(33): p. 11613-11618.
212. Bao, S.J., C.M. Li, C.X. Guo, and Y. Qiao, *Biomolecule-assisted synthesis of cobalt sulfide nanowires for application in supercapacitors.* Journal of Power Sources, 2008. **180**(1): p. 676-681.
213. Bao, S.J., Y.B. Li, C.M. Li, Q.L. Bao, Q. Lu, and J. Guo, *Shape evolution and magnetic properties of cobalt sulfide.* Crystal Growth & Design, 2008. **8**(10): p. 3745-3749.
214. Xia, Z. and J.T. Triffitt, *A review on macrophage responses to biomaterials.* Biomedical Materials, 2006. **1**(1): p. R1-R9.
215. Lee, W.L., D. Mason, A.D. Schreiber, and S. Grinstein, *Quantitative analysis of membrane remodeling at the phagocytic cup.* Molecular Biology of the Cell, 2007. **18**(8): p. 2883-92.
216. van Zon, J.S., G. Tzircotis, E. Caron, and M. Howard, *A mechanical bottleneck explains the variation in cup growth during FcgammaR phagocytosis.* Mol Syst Biol, 2009. **5**: p. 298.
217. Champion, J.A. and S. Mitragotri, *Shape Induced Inhibition of Phagocytosis of Polymer Particles.* Pharmaceutical Research, 2009. **26**(1): p. 244-249.

Appendix

Publications

1. ***Z. S. Lu***, Y. S. Liu, W. H. Hu, X. W. Lou, C. M. Li*: Rewritable multicolour fluorescent patterns for multistate memory devices with high data storage capacity. Submitted.
2. ***Z. S. Lu***, C. M. Li*: Quantum dot–based nanocomposites for biomedical applications. Submitted.
3. ***Z. S. Lu***, Z. H. Zhu, X. T. Zheng, Y. Qiao, J. Guo, C. M. Li*: Biocompatible fluorescence-enhanced ZrO_2–CdTe quantum dots nanocomposite for in vitro cell imaging. ***Nanotechnology***, 22, 155604, **2011**.
4. ***Z. S. Lu***, W. H. Hu, H. F. Bao, Y. Qiao, C. M. Li*: Interaction mechanisms of CdTe quantum dots with proteins possessing different isoelectric points. ***Med. Chem. Commun.***, DOI: 10.1039/C0MD00237B, **2011**.
5. ***Z. S. Lu***[#], C. X. Guo[#], H. B. Yang, Y. Qiao, J. Guo, C. M. Li*: One–step aqueous synthesis of graphene–CdTe quantum dot–composed nanosheets and its enhanced photoresponses. ***J. Colloid Interface sci.***, 353, 588–592, **2011**. **(# Contribution equally to this work)**
6. ***Z. S. Lu***, Y. Qiao, X. T. Zheng, M. B. Chan–Park, C. M. Li*: Effect of particle shape on phagocytosis of CdTe quantum dot–cystine composites. ***Med. Chem. Comm.***, 1, 84–86, **2010**. (***Top 10 most accessed paper in July and September 2010***)
7. ***Z. S. Lu***, C. M. Li*, H. F. Bao, Y. Qiao Q. L. Bao: Photophysical mechanism for quantum dots–induced bacterial growth inhibition, ***J. Nanosci. Nanotech***, 9, 3252–3255, **2009**.
8. ***Z. S. Lu***, C. M. Li*, H. F. Bao, Y. Qiao, Y. H. Toh: Mechanism of antimicrobial activity of CdTe quantum dots. ***Langmuir***, 24, 5445–5452, **2008**.

9. ***Z. S. Lu***, C. M. Li*, Q. Zhou, Q. L. Bao, X. Q. Cui: Covalently linked DNA/protein multilayered film for controlled DNA release. ***J. Colloid Interface sci.***, 314, 80–88, **2007.**

10. H. F. Bao[#], ***Z. S. Lu***[#], X. Q. Cui, Y. Qiao, J. Guo, J. M. Anderson, C. M. Li*: Extracellular microbial synthesis of biocompatible CdTe quantum dots. ***Acta Biomaterialia,*** 6, 3534–3541, **2010**. **(# Contribution equally to this work)**

11. W. Y. Yuan, ***Z. S. Lu***, C. M. Li*: Controllably layer-by-layer self-assembled polyelectrolytes/nanoparticle blend hollow capsules and their unique properties. ***J. Mater. Chem***, 21, 5148-5155, **2011**.

12. W. H. Hu, ***Z. S. Lu***, Y. S. Liu, C. M. Li*: In situ surface plasmon resonance investigation of assembly process of multiwall carbon nanotubes on alkanethiol self–assembled monolayer for efficient protein immobilization and detection. ***Langmuir***, 26, 8386–8391, **2010**.

13. C. X. Guo, ***Z. S. Lu***, Y. Lei, C. M. Li*. Ionic liquid–graphene composite for ultratrace explosive trinitrotoluene detection. ***Electrochem Comm,*** 12, 1237–1240, **2010**.

14. Q. L. Bao, ***Z. S. Lu***, J. Li, K. P. Loh, C. M. Li*: Theoretical and experimental studies of electronic transport of dithienothiophene. ***J. Phys Chem C***, 113, 12530–12537, **2009**.

15. G. C. Yuan, ***Z. S. Lu***, Z. Xu, C. Gong, Q. L. Song, N. Xu, C. M. Li*: Microstructure transformations induced by modified layers on pentacene polymorphic films and their effect on performance of organic thin film transistor. ***Organ. Electron***, 10, 1388–1395, **2009**.

16. L. Yu, ***Z. S. Lu***, Y. Gan, Y. S. Liu, C. M. Li*: AFM study of adsorption of protein A on a poly(dimethylsiloxane) surface. ***Nanotechnology***, 20, 285101, **2009**

17. W. Chen, ***Z. S. Lu***, C. M. Li*, Sensitive human interleukin 5 impedimetric sensor based on polypyrrole–pyrrole propylic acid–gold nanocomposite, ***Anal Chem***, 80, 8485–8492, **2008**.

18. G. H. Guai, Q. L. Song, ***Z. S. Lu***, C. M. Li: Effects of multiple heat treatment cycles on structure, optical and electrical properties of indium-tin-oxide thin films. ***Surf. Coat. Technol.*** 205, 2852-2856, **2011**.

19. C. X. Guo, X. T. Zheng, ***Z. S. Lu***, X. W. Lou, C. M. Li*: Biointerface by cell growth on layered graphene–artificial peroxidase–protein nanostructure for in situ quantitative molecular detection, ***Adv. Mater.***, 22 5164-5167, **2010**.

20. W. H. Hu, Y. S. Liu, ***Z. S. Lu***, C. M. Li*: Poly(oligo(ethylene glycol) methacrylate–co–glycidyl methacrylate) Brush Substrate for Sensitive Surface Plasmon Resonance Imaging Protein Arrays. ***Adv. Funct. Mater.***, 20, 3479–3503, **2010**.

21. H. B. Yang, Q. L. Song, ***Z. S. Lu***, C. X. Guo, C. Gong, W. H. Hu, C. M. Li*: Electrochemically polymerized nanostructured poly(3.4–ethylenedioxythiophene)–poly(styrenesulfonate) buffer layer for a high performance polymer solar cell. ***Energy Environ. Sci.,*** 3, 1580–1586, **2010**.

22. Y. S. Liu, W. H. Hu, ***Z. S. Lu***, C. M. Li*: Photografted poly(methyl methacrylate)–based high performance protein microarray for hepatitis B virus biomarker detection in human serum. ***Med. Chem. Comm.***, 1, 132–135, **2010**.

23. Y. Qiao, C. M. Li*, ***Z. S. Lu***, H. Ling, A. Kang, M. W. Chang: A time–course transcriptome analysis of Escherichia coli with direct electrochemistry behavior in microbial fuel cells. ***Chem. Comm.***, 6183 – 6185, **2009**.

24. Q. J. Cai, M. B. Chan–Park, ***Z. S. Lu***, C. M. Li*, B. S. Ong: Bottom–contact poly(3,3'"–didodecylquaterthiophene) thin–film transistors with gold source–drain electrodes modified by alkanethiol monolayers. ***Langmuir***, 24, 11889–11894, **2008**.

25. C. Gong, H. B. Yang, Q. L. Song, ***Z. S. Lu***, C. M. Li*: Solar cells made from polymers containing Dithieno[3,2-b:2′,3′-d]pyrrole with different side chain lengths. ***Sol. Energy Mater. Sol. Cells***, 95, 969–973, **2011**.

26. C. X. Guo, H. B. Yang, Z. M. Sheng, ***Z. S. Lu***, Q. L. Song, C. M. Li*: Layered Graphene/Quantum Dots for Photovoltaic devices. ***Angew. Chem. Int. Ed.,*** 49, 3014–3017, **2010**.

27. R. Li, X. Q. Cui, W. H. Hu, ***Z. S. Lu***, C. M. Li*: Fabrication of oriented poly–L–lysine/bacteriorhodopsin–embedded purple membrane multilayer structure for enhanced photoelectric response. ***J. Colloid Interface Sci.*** 344, 150–157, **2010**.

28. Y. S. Liu, C. M. Li*, W. H. Hu, ***Z. S. Lu***: High performance protein microarrays based on glycidyl methacrylate–modified polyethylene terephthalate plastic substrate. ***Talanta,*** 77, 1165–1171, **2009**.

29. Y. Qiao, C. M. Li*, S. J. Bao, ***Z. S. Lu***, Y. H. Hong: Direct electrochemistry and electrocatalytic mechanism of evolved Escherichia coli cells in microbial fuel cells. ***Chem. Comm.***, 11, 1290 –1292, **2008.**

30. W. Chen, C. M. Li*, L. Yu, ***Z. S. Lu***, Q. Zhou: In situ AFM study of electrochemical synthesis of polypyrrole/Au nanocomposite. ***Electrochem. Comm.,*** 10, 1340–1343, **2008.**

31. H. B. Yang, Q. L. Song, C. M. Li*, ***Z. S. Lu***: New architecture to accurately characterize the behaviors of individual sub–cells within a tandem organic solar cell, ***Energy Environ. Sci.*** 1, 389 – 394, **2008**.

32. Q. J. Cai, M. B. Chan–Park, Q. Zhou, ***Z. S. Lu***, C. M. Li*. B. S. Ong: Self–assembled monolayers mediated charge injection for high performance bottom–contact poly(3,3 '''–didodecylquaterthiophene) thin–film transistors. ***Organ. Electron.***, 9, 936–943, **2008.**

33. Q. J. Cai, Y. Gan, M. B. Chan–Park, H. B. Yang, ***Z. S. Lu***, C. M. Li*, J. Guo, Z. L. Dong: Solution–processable barium titanate and strontium titanate nanoparticle dielectrics for low–voltage organic thin–film transistors. ***Chem. Mater.***, 14, 3153–3161, **2009**.

34. Y. Gan, Q. J. Cai, C. M. Li*, H. B. Yang, ***Z. S. Lu***, G. Cheng; M. B. Chan–Park: Solution–prepared hybrid–nanoparticle dielectrics for high performance low voltage organic thin–Film transistors. ***ACS Appl. Mater. Interfaces***, 1, 2230–2236, **2009**.

35. G. C. Yuan, Z. Xu, C. Gong, Q. J. Cai, ***Z. S. Lu***, J. S. Shi , F. J. Zhang , S. L. Zhao, N. Xu, C. M. Li*: High performance organic thin–film transistor with phenyltrimethoxysilane–modified dielectrics. ***Appl. Phys. Lett.,*** 94, 153308, **2009**.

36. Y. Qiao, S. J. Bao, C. M. Li*, X. Q. Cui, ***Z. S. Lu***, J. Guo: Nanostructured polyaniline/titanium dioxide composite anode for microbial fuel cells. ***ACS Nano***, 2, 113–119, **2008.**

37. W. Zhang, J. Li, L. Zhou, B. Zhang, J. Qin, ***Z. S. Lu***, Y. F. Poon, M. B. Chan–Park, C. M. Li*: Semiconductive polymers containing Dithieno[3,2 – b:2, 3 – d]pyrrole for organic thin – film transistors. ***Macromolecules***, 41, 8953–8955, **2008.**

38. Q. L. Bao, J. Li, C. M. Li*, Z. L. Dong, ***Z. S. Lu***, F. Qin, C. Gong, J. Guo: Direct observation and analysis of annealing–induced microstructure at interface and its effect on performance improvement of organic thin film transistors. ***J. Phys. Chem. B***, 112, 12270–12278, **2008**.

39. Q. J. Cai, Y. Gan, M. B. Chan–Park, H. B. Yang, ***Z. S. Lu***, Q. L. Song, Z. L. Dong, C. M. Li*: Solution–processable organic–capped titanium oxide nanoparticles dielectrics for organic thin–film transistors. ***Appl. Phys. Lett.,*** 93, 113304, **2008**.

40. X. Q. Cui, C. M. Li*, H. F. Bao, X. T. Zheng, ***Z. S. Lu***: In–situ fabrication of silver nanoarrays in hyaluronan/PDDA layer–by–layer assembled structure. ***J. Colloid Interface Sci.***, 327, 459–465, **2008**.

41. Q. L. Bao, S. J. Bao, C. M. Li*, X. Qi, C. X. Pan, J. F. Zang, ***Z. S. Lu,*** Y. B. Li, D. Y. Tang, S. Zhang, K. Lian. Supercapacitance of solid carbon nanofibers made from ethanol flames***. J. Phys. Chem. B***, 112, 3612–3618, **2008.**

42. H. F. Bao, X. Q. Cui, C. M. Li*, Q. L. Song, ***Z. S. Lu***, J. Guo: Synthesis and Electrical Transport Properties of Single–crystal Antimony Sulfide (Sb2S3) Nanowires. ***J. Phys. Chem. C***, 111, 17131–17135, **2007**.

43. W. Y. Yuan, H. Dong, C. M. Li*, X. Q. Cui, L. Yu, ***Z. S. Lu***, Q. Zhou: pH–controlled construction of chitosan/alginate multilayer film: characterization and application for antibody immobilization. ***Langmuir***, 23, 13046–13052, **2007.**